Master Thesis in Geosciences

Caprock interaction with CO_2

Geomechanical and geochemical effects

Magnus Soldal

UNIVERSITY OF OSLO

FACULTY OF MATHEMATICS AND NATURAL SCIENCES

Blank page, for double side paper print.

Remove for digital publishing

Caprock interaction with CO_2

Geomechanical and geochemical effects

Magnus Soldal

Master Thesis in Geosciences

Discipline: Environmental Geology

Department of Geosciences

Faculty of Mathematics and Natural Sciences

UNIVERSITY OF OSLO

[April 2008]

Tutor(s): Per Aagaard (UiO) and Elin Skurtveit (NGI)

This work is published digitally through DUO – Digitale Utgivelser ved UiO

http://www.duo.uio.no

It is also catalogued in BIBSYS (http://www.bibsys.no/english)

Acknowledgements

First I would like to thank my supervisor, Professor Per Aagaard, for allowing me to be a part of the SSC Ramore project and for help and guidance whenever needed. Elin Skurtveit, my external supervisor at NGI, has been vital in ensuring project progression.

During my time at NGI I have gotten to know many clever and helpful people. I would especially like to thank Gudmund Havstad and Toralv Berre for sharing their impressive knowledge, and for demonstrating great patience throughout the project. Other NGI employees I have benefited from are Trude Ørbech, Reidar Otter, Lloyd Tunbridge, Eivind Aker and Erik Lied. Thanks to Matthieu Angeli for mercury porosimetry test and for a highly appreciated, thorough review of the report. Many thanks also to Morten Sjursen for employing me in the lab in those long months awaiting experimental startup.

Thanks to Mufak Naoroz at the Department of Geosciences for great help with the chemical analysis. Many thanks to Berit Løken Berg and Turid Winje for their very qualified and kind assistance during XRD and SEM analysis. I would also like to thank Julien Declercq for assistance with the batch reactor experiments at the University of Oslo, and Yacob Abreham for help with PHREEQC.

I also have to thank the Troll License for letting us use the excellent claystone material from the Draupne Formation in the experiment.

Thanks to fellow student Anders Bergsli and my sister Ellen Soldal for their reviews and comments to the manuscript. They were appreciated!

Finally I would like to thank my girlfriend, Ingrid, for motivating me during this very challenging and often frustrating process.

Magnus Soldal, April 2008

Abstract

Subsurface storage of carbon dioxide is often considered one of the most promising ways of reducing atmospheric levels of CO_2. The safety of the operation is closely related to the performance of caprocks overlying the formations in which CO_2 is injected. Interactions between CO_2 or CO_2/brine and caprocks can alter the sealing capacity which prevents upward migration of CO_2. This thesis is a part of the *SSC Ramore* project, concerned with risk assessment related to underground geological storage of CO_2. A new experimental design allowing a caprock core to be flooded with CO_2 was prepared and tested at the Norwegian Geotechnical Institute (NGI). The initial aim of injecting CO_2 saturated brine into a sample from the Draupne Formation had to be altered due to experimental difficulties encountered. Instead it was decided to perform a capillary breakthrough pressure test. By applying a gradually increasing pressure gradient across the sample, an apparent flow of supercritical CO_2 was obtained at a breakthrough pressure of ~3.5 MPa. However, the interpretation of this as a real breakthrough pressure was made difficult by the simultaneous onset of a significant radial expansion. Geochemical effects of Draupne claystone interacting with acidic CO_2-saturated brine were investigated in a batch reactor at the University of Oslo (UiO). Small amounts of powdered claystone material were reacted with solutions with pH ranging from 2 – 10. At the pH levels expected in underground geological formations after CO_2 injection, the experiment indicates that most of the carbonates present in the Draupne caprock are dissolution-prone.

Table of contents

1 Introduction 2

2 Objectives 4

3 Theory 6

3.1 Properties of CO_2 - brine 7

3.2 Geochemical effects 10

3.2.1 Hydrodynamic trapping 11

3.2.2 Mineral trapping 12

3.3 Geomechanical effects 16

3.3.1 Cap rock integrity 16

3.3.2 Creep mechanisms 18

3.3.3 Seismic velocities 19

4 Previous experimental and modelling work 20

4.1 Similar experimental setups 20

4.2 Geochemical experiments and models 21

4.3 Geomechanical experiments 24

5 Experimental setup 26

5.1 Flow through cell at NGI 26

5.1.1 Data logging and processing 31

5.2 Batch reactor at UiO 32

6 Characterization of material used in the experiments 34

7 Experimental procedure 40

7.1 Flow through cell at NGI 40

7.2 Batch reactor at UiO 46

8 Results 48

8.1 Flow through cell at NGI 48

8.1.1 Saturation of sample 48

8.1.2 Consolidation 48

8.1.3 Permeability test 52

8.1.4 Breakthrough pressure test 55

8.2 Batch reactor at UiO 62

9 Discussion 67

10 Conclusion 69
11 References 71

1 Introduction

When sunlight strikes the Earth's surface, some of it is reflected back towards space as infrared radiation. Greenhouse gases (like water vapor, carbon dioxide and methane) absorb this infrared radiation (heat) and trap it in the atmosphere. The amount of energy added to the atmosphere by the greenhouse effect is determined by the atmospheric concentrations of greenhouse gases (Doerr and Coling, 1993).

Since the large-scale industrialization began around 1850, levels of several important greenhouse gases have increased substantially. Over the same period of time the average global air temperature near the Earth's surface has increased by approximately 0.75ºC (IPCC, 2005). In terms of global warming, carbon dioxide (CO_2) is the greenhouse gas making the largest contribution from human activities. The main anthropogenic source of CO_2 is fossil fuel combustion in the power generation, industrial, residential and transport sectors. The atmospheric concentration of CO_2 is naturally regulated by the processes defined in the "carbon cycle" (Falkowski et al., 2000). The movement of carbon between the atmosphere and the land and oceans is dominated by photosynthesis, respiration and decomposition. Although these processes are able to absorb some of the anthropogenic CO_2 emissions, there is still a significant yearly increase in the atmospheric levels (Doerr and Coling, 1993).

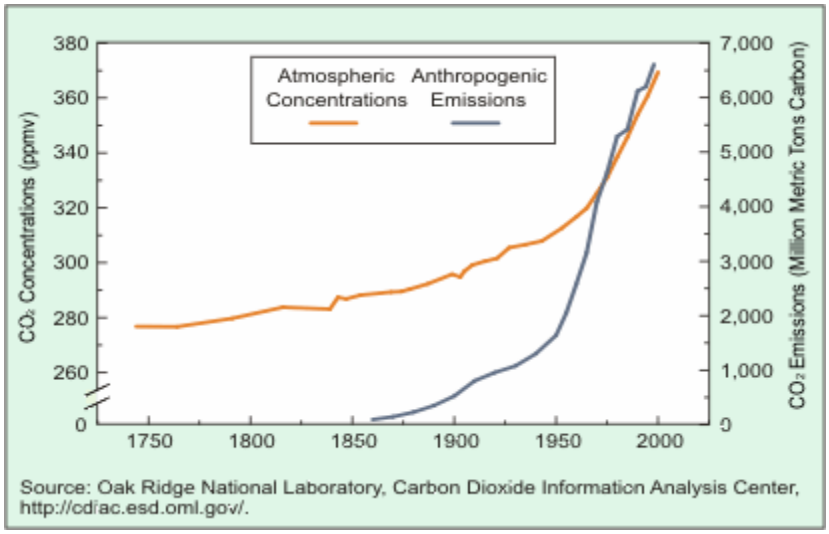

Figure 1: Atmospheric concentrations and anthropogenic emissions of CO_2 from 1750 to 2000 (www.eia.doe.gov, 2007).

The nature of changes in the climate caused by humans can be difficult to establish due to the natural variability of the Earth's climate (Bachu, 2003). Virtually all computer-based models indicate that rising CO_2 concentrations give an increase in the average temperature. Rising temperatures may again cause changes in weather, sea levels and land use patterns, commonly

referred to as “climate change”. Recently the Intergovernmental Panel on Climate Change (IPCC) published their fourth report concerning climate change. In it the probability that climate changes are caused by anthropogenic activities was estimated to over 90 percent (Black, 2007).

Current proposals to reduce atmospheric levels of carbon dioxide often include capture and subsequent storage in subsurface geological formations (e.g. (Bachu, 2003;Doughty et al., 2007;Gaus et al., 2005;Gunter et al., 2004;Holloway, 2001;IPCC, 2005;Klara et al., 2003;Lindeberg, 1997;Torp and Gale, 2004)). Three main options for subsurface storage have been identified; existing oil and gas fields, saline aquifers and unmineable coal beds. Main benefits are potential storage times, volumes available and low environmental impacts. Basins suitable for underground geological storage usually display some common features. The formations should be thick and permeable accumulations of sediments, sealed by a low porosity cap rock (IPCC, 2005).

At the pressure and temperature regimes usually encountered in deep subsurface formations, injected CO_2 will be in a supercritical phase. Being less dense than the formation water, the carbon dioxide will rise buoyantly and accumulate beneath the cap rock. The storage safety is therefore closely related to the ability of the cap rock to prevent further migration of the carbon dioxide. In this study attempts were made to experimentally examine the geochemical and geomechanical effects of CO_2/brine interactions with a cap rock sample from the Draupne Formation.

2 Objectives

The thesis is a part of the SSC RAMORE project led by the University of Oslo (UiO), in cooperation with the University of Bergen (UiB), the Norwegian Geotechnical Institute (NGI) and the Institute for Energy Technology (IFE). SSC RAMORE is concerned with risk assessment, monitoring and remediation connected to subsurface storage of CO_2 (UiO et al., 2008).

The main leakage risks associated with underground storage of carbon dioxide are related to wells and cap rocks. As cap rocks are the sealing agents overlying the porous formations in which CO_2 is injected, their performance is vital in determining the safety of the operation. Initially this thesis aimed at experimentally investigating the geomechanical and geochemical effects of cap rock flooding with CO_2/brine. After characterizing the cap rock using XRD and SEM, a permeability test was performed with artificial formation water. Using a flow through cell at the Norwegian Geotechnical Institute (NGI), CO_2-saturated brine was then to be injected into a claystone cap rock of the Draupne Formation collected at the Troll East Field. Axial and radial deformation sensors could provide information about the geomechanical development, while chemical analysis of fluids leaving the cell would provide insight into the geochemical development. Seismic velocities as a function of CO_2 saturation degree could be obtained from piezoelectric transducers mounted inside the top and bottom filters. The initial objectives had to be somewhat altered however, when it turned out the container in which the two phases were to be mixed did not tolerate the acidic environment arising. As capillary leakage may pose the most severe threat to cap rock safety, it was decided to perform a capillary breakthrough test instead. Capillary breakthrough pressure can be defined as the minimum pressure needed for the non-wetting fluid to displace the wetting fluid (Chiquet et al., 2007a), and is a key factor for caprocks as it determines the maximum CO_2 injection pressure which can be applied. By imposing a slowly increasing pressure gradient, the aim was to establish a minimum pressure needed for supercritical CO_2 to break through the water saturated sample.

Carbon dioxide injection into formation waters causes the pH to drop. To see what kind of geochemical alterations CO_2 injection could impose on the claystone, small samples were reacted with solutions of different pH in a batch reactor at the University of Oslo (UiO). After

48 hours at 200C, the solutions were examined for ion contents. Computer calculations using the final solution compositions as input indicated if saturation had been reached with respect to carbonate minerals.

Experimental work related to storage of CO_2 can be challenging and tedious. This was certainly experienced in this study, as can be seen by the deviation between the final experimental procedure and the one initially intended. As a consequence the methodical performance itself constitutes a vital part of the thesis objectives. Since the experimental design, and to some extent the procedures, are new at NGI, focus was on developing reasonable methods. The different approaches carried out and problems encountered are all included in this report. This is done partly because a significant portion of the time available was spent on them, and partly based on the belief that sharing of experimental experiences is important.

The report is roughly made up of five parts. Chapter 3 tries to describe important aspects of subsurface storage of CO_2, and potential geochemical and geomechanical effects. Even though the focus of the thesis is on caprock response, several processes are referred to from a reservoir rock perspective. This is done partly because the amount of literature available, and partly because many of the processes are similar. Chapter 4 gives a quick overview over similar previous experimental setups, and results from relevant geomechanical and geochemical experiments.

Chapter 5 and 7 describes the experimental setup and procedures used, and how they changed during the thesis. Chapter 6 is devoted to a rather thorough characterization of the material used. In chapter 8 the results as interpreted so far are presented. As emphasized in the discussion (chapter 9) and conclusion (chapter 10), the large amount of data available has not yet been fully processed.

3 Theory

Carbon dioxide Capture and Storage (CCS) involves capturing CO_2 generated by fuel combustion or released from industrial processes, and storing it away from the atmosphere for a very long time. The feasibility of the process as a CO_2 mitigation option has been demonstrated by several existing enhanced oil recovery projects like Weyburn (Li et al., 2006), in addition to the Sleipner (Bentham and Kirby, 2005) and Salah (IPCC, 2005) projects.

Detritus formations in the subsurface are composed of transported and deposited rock grains, minerals formed after deposition of the rock and organic material. The pore spaces between the grains and minerals are occupied by water and some oil and gas. The rocks making up the formation can be divided into cap rocks and reservoir rocks. The cap rocks are virtually impermeable rocks which form a barrier above the reservoir rocks. CO_2 injected into such formations will interact with both cap rock and reservoir rock, in addition to the in situ formation water (IPCC, 2005). Before looking more in detail at the potential geochemical and geomechanical effects of these interactions, it might be useful to examine some properties of the injected fluid.

3.1 Properties of CO_2 - brine

The distribution of CO_2 injected into water – rock systems is closely related to the differences in physical parameters between CO_2 and formation water. Under normal atmospheric temperature and pressure conditions, carbon dioxide is in the gas phase. According to the phase diagram of CO_2 (figure 2), solid CO_2 ("dry ice") is stable under low temperatures and somewhat elevated pressures. As liquid CO_2 forms only at pressures above 0.5 MPa, increasing the temperature at low pressures will change solid CO_2 directly into gaseous CO_2 through sublimation. The triple point of carbon dioxide, where the solid, liquid and gaseous phase coexists, is at 0.52 MPa and 56.6°C. The critical point is at 31.1°C and 7.38 MPa. Beyond this point CO_2 behaves in the dual way associated with supercritical fluids, namely filling all available volume like a gas, but with the density of a liquid. Subsurface storage of carbon dioxide is usually expected to take place below depths of 800 meters, where temperature and pressure conditions are such that CO_2 is in the supercritical phase (IPCC, 2005).

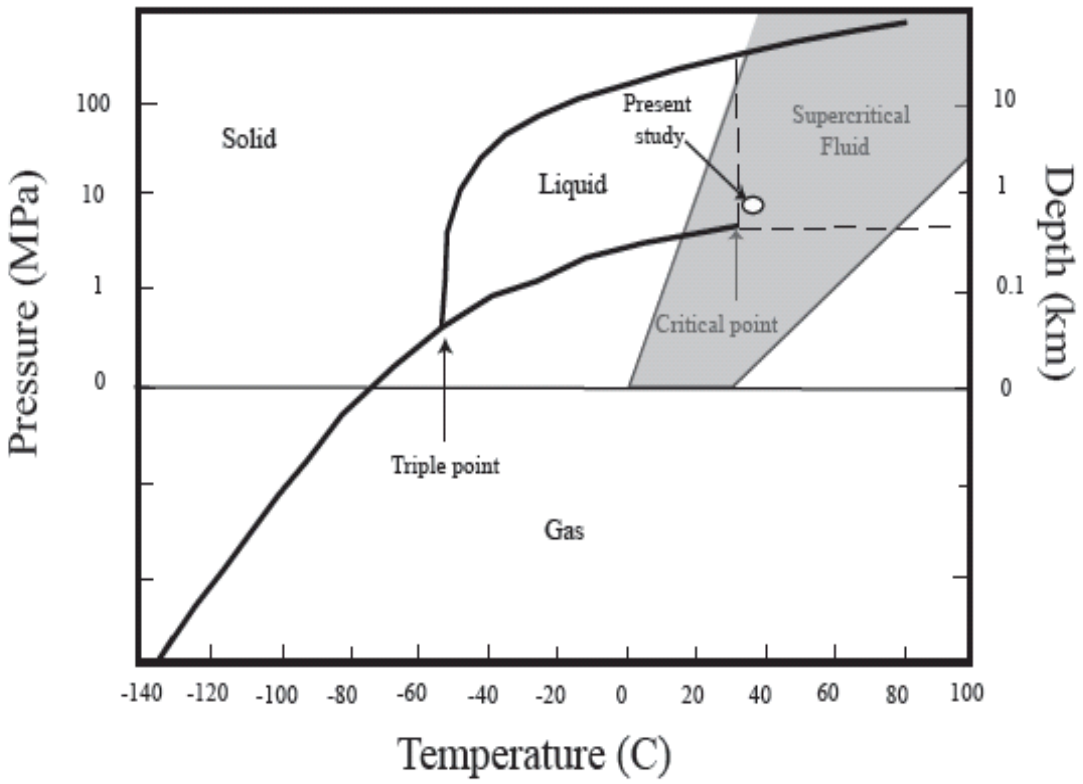

Figure 2: Phase diagram of CO_2 showing the pressure and temperature envelope for sedimentary basins worldwide (in grey). Pressure and temperature conditions used in this study marked with circle.

The density of CO_2 affects carbon dioxide storage in several ways (e.g. (Adams and Bachu, 2004;Bachu, 2003;Nordbotten et al., 2005;Suekane et al., 2005)). Higher density allows more CO_2 to be stored in the pore volumes available in formations. At the same time, the buoyancy forces which may threaten the safety by causing the CO_2 to migrate upward and updip are reduced with increasing density. The density of CO_2 generally increases with pressure and decreases with temperature (figure 3). At depths considered for underground storage of CO_2, the density of CO_2 typically varies between 0.6-0.8 g/cm^3 (Gunter et al., 2004). At the pressure and temperature used in this study (*P~8.0 MPa* and *T=36ºC*) the density of CO_2 is close to 0.6 g/cm^3 (figure 3). The density of formation waters depends on salinity, in addition to pressure and temperature. The density (ρ_b) of 1 M NaCl solution at 8.0 MPa and 36ºC can be estimated based on an empirically derived expression by Phillips et al. (1981);

$$\rho_b = -3.033405 + 10.1288163x - 8.750567x^2 + 2.663107x^3 \quad (3.1)$$

$$x = -9.9559e^{-0.004539 \cdot m} + 7.0845e^{-0.0001638 \cdot T} + 3.9093e^{0.00002551 \cdot P} \quad (3.2)$$

where *P* is pressure in bars, *T* is temperature in Celsius and *m* is NaCl molality (Phillips et al., 1981). The calculated density is 1.04 g/cm^3, which is close to 75 % higher than the CO_2 density.

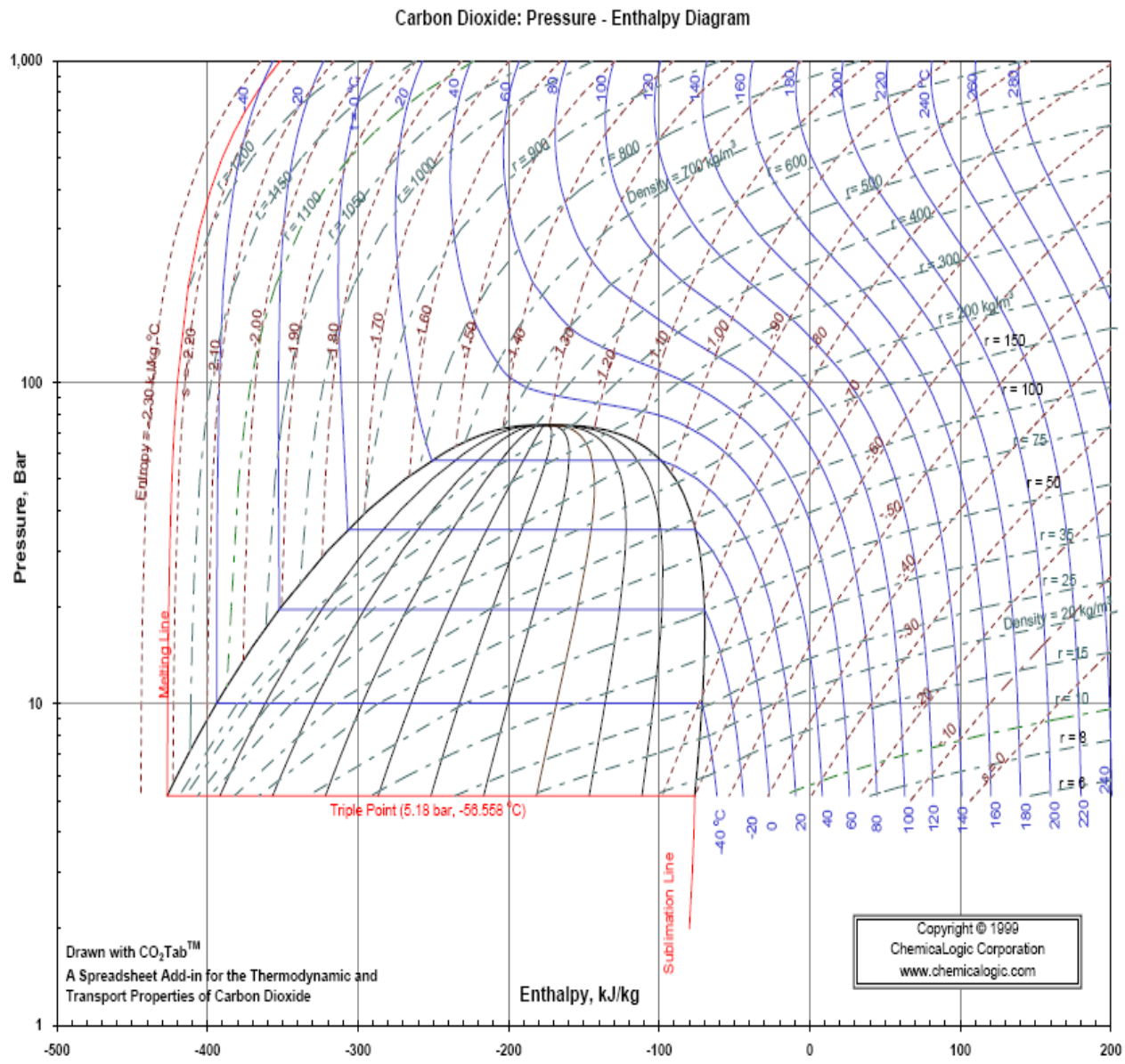

Figure 3: The Mollier diagram for carbon dioxide displays the pressure on a logarithmically scaled Y-axis and the enthalpy on the X-axis. Furthermore the diagram includes temperature, density and entropy contour lines (www.chemicalogic.com, 2008).

Viscosity describes fluids' resistance to flow and for CO_2 it increases with pressure and temperature. Under the relevant conditions, CO_2 has a viscosity around 3.0×10^{-5} Pa s (Fenghour et al., 1998). The viscosity of water decreases with temperature, and increases with salinity and pressure. Temperature is the main controlling factor (Adams and Bachu, 2004), and under the pressure and temperature conditions in this study, the viscosity of water is more than ten times that of supercritical CO_2 (Suekane et al., 2005).

The volume change of fluids in response to applied pressure is expressed as their compressibility. Compared to water, supercritical CO_2 has a very high compressibility (Yuh, 2003), meaning that relatively small pressure and temperature changes can significantly alter its density. Actually, the compressibility of CO_2 close to the critical point $((\delta\rho/\delta P)_{T=Tc}$ at $P \rightarrow P_c)$ approaches infinite values (Abdulagatov et al., 2007). The changes in isothermal compressibility ($\Delta T=0$) with pressure is significantly larger and more distinct at 35ºC than at 50ºC (figure 4) (Sirard et al., 2002). For comparison, the very small compressibility of water at 8.0 MPa and 36ºC is approximately 43.4×10^{-6} bar^{-1} (Fine and Millero, 1973).

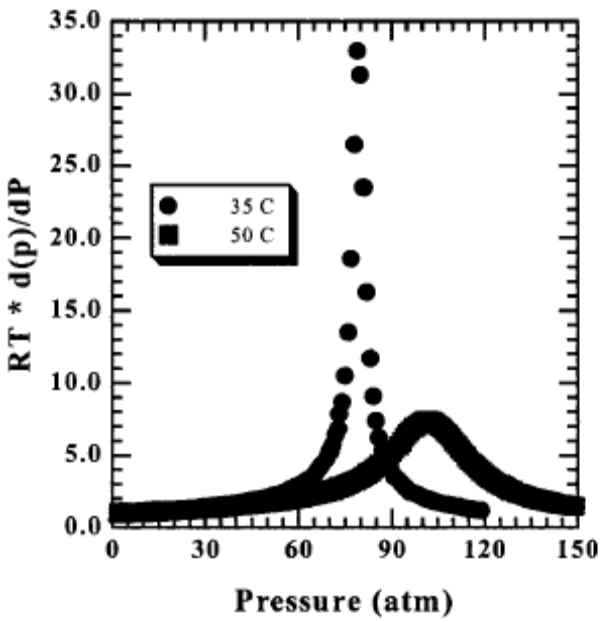

Figure 4: The isothermal compressibility of CO2 at 35ºC and 50ºC (Sirard et al., 2002).

In terms of displacement processes between CO_2 and water, the lower viscosity of CO_2 leads to viscous fingering, while the lower density may cause a gravitational segregation (Nordbotten et al., 2005). Viscous fingering refers to the finger-shaped structures resulting from the injection of low viscosity fluids into fluids with higher viscosity. Due to viscous fingering and gravitational segregation, injected CO_2 will spread and accumulate above the water phase (Suekane et al., 2005).

3.2 Geochemical effects

As already mentioned, CO_2 will be in a supercritical phase at depths of geological formations considered for storage of carbon dioxide. Being less dense than water, the supercritical CO_2 will rise until it reaches the overlying cap rock. This kind of *physical trapping* beneath stratigraphic or structural barriers is the principle means to store CO_2 in geological formations. With time CO_2 will dissolve into the formation water, removing buoyancy as a reason for migration. The dissolved CO_2 will instead migrate according to relatively slow

regional-scale groundwater flows. The storing of CO_2 dissolved in slow moving waters is referred to as *hydrodynamic trapping* (Czernichowski-Lauriol et al., 2006). Finally, CO_2 can be locked up in carbonate minerals in *mineral trapping* (Rochelle et al., 2008). Some of the most probable carbonate minerals forming are calcite ($CaCO_3$), magnesite ($MgCO_3$), siderite ($FeCO_3$) and dawsonite ($NaAlCO_3(OH)_2$) (Hellevang et al., 2006). The advantages of mineral trapping are apparent, as the CO_2 would be stored in fairly stable minerals over very long timescales (Rochelle et al., 2008). The relevant geochemical alterations caused by CO_2 injection into a claystone cap rock, will be presented based on the two latter trapping mechanisms.

3.2.1 Hydrodynamic trapping

The amount of CO_2 dissolving in the water is expressed as solubility, and varies with temperature, pressure and salinity. The solubility increases in a more pronounced manner for pressures up to 10 MPa than for pressures above this (Koschel et al., 2006). For pressures below 10 MPa, the solubility decreases with increasing temperature. But above this pressure the trend is slowly changing, and at 25 MPa the solubility increases with temperature (Portier and Rochelle, 2005). The reduction in solubility caused by the presence of salts is known as salting-out effect (Jodecke et al., 2004). Although the decreasing solubility trend is similar for the presence of both monovalent and divalent salts, Portier and Rochelle pointed out that the solubility in divalent solutions is higher than in monovalent solutions with the same ionic strength. This might be attributed to the fact that divalent cations (*e.g.* Mg^{2+} and Ca^{2+}) very easily form ion pairs with the anions present in the solution, leading to a lower salting-out effect than monovalent ions (*e.g.* Na^{+}) (Portier and Rochelle, 2005). For a 1 M NaCl-solution at 8.8 MPa and 36°C, the theoretical CO_2 solubility is approximately 1.0 mol/kg water (Duan and Sun, 2003).

The dissolution of CO_2 in water can be represented by the following reaction sequence (Rochelle et al., 2008);

$$CO_{2,aq} + H_2O \leftrightarrow H_2CO_3 \leftrightarrow HCO_3^- + H^+ \leftrightarrow CO_3^{2-} + H^+ \tag{3.3}$$

Since pressure and temperature levels control the solubility, they also govern this series of reversible reactions. In addition, the speciation of CO_2 is closely related to pH (figure 5).

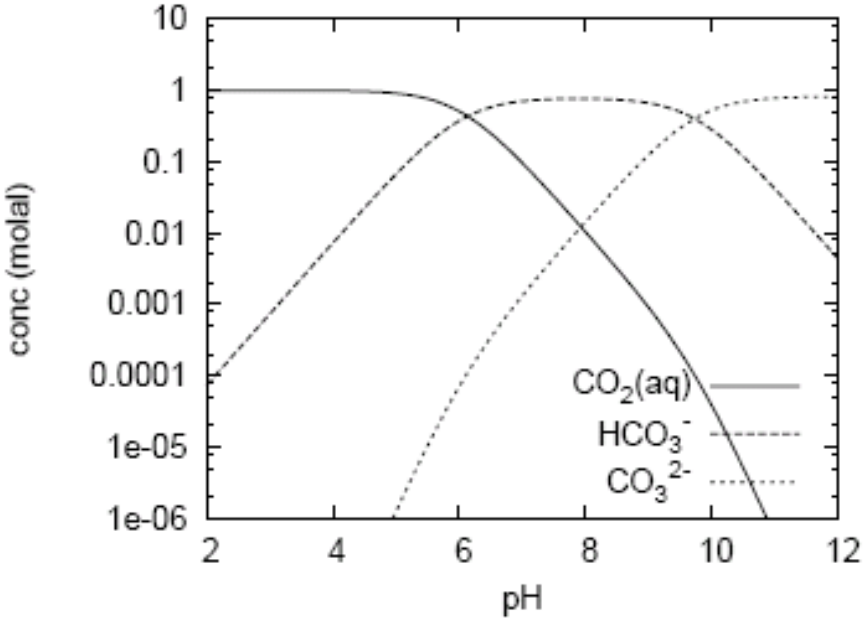

Figure 5: The speciation of dissolved CO_2 as a function of pH in a closed system with 1 m NaCl solution at 60ºC (Lagneau et al., 2005).

Dissolved CO_2 ($CO_{2,aq}$) dominates at low pH, while bicarbonate (HCO_3^-) and carbonate (CO_3^{2-}) dominate at intermediate and high pH, respectively (Lagneau et al., 2005). The release of H^+-ions in the dissolution sequence acidifies the solution to a degree determined by the amount of CO_2 dissolving and the pH-buffering capacity of the host formation (Rochelle et al., 2008). For example, as carbonates are dissolving, the resulting bicarbonate is reduced by further reactions within the carbonate system. The divalent cations however, are non-reactive in the solution, leading to a net increase in the positive charges in the solution. The dissolution of carbonates will therefore lead to a higher pH according to the criteria of electroneutrality (Hellevang et al., 2006).

3.2.2 Mineral trapping

Dissolved CO_2 moving though reservoir- and cap rocks acts as a weak acid capable of destabilizing primary minerals. Neutralization by formation of bicarbonate or carbonate ions is realized through reactions with silicate minerals (*e.g.* feldspars, clay minerals) or calcium-, magnesium- and iron carbonates (Gunter et al., 2004). Due to their high porosity and permeability, sandstone- and coarse carbonate formations are most often considered as host rocks for carbon dioxide injection. The overlying cap rocks are usually shales or salts. The

chemical reactions and rates in these differing lithologies vary as their mineralogical compositions are very different (Rochelle et al., 2008). Here the main focus will be on reactions relevant for the minerals found in shales. Generally the most important primary minerals in terms of dissolution are the ones containing components which may participate in the formation of new carbonate minerals. These components are mainly divalent cations M^{2+} (*e.g.* Ca^{2+}, Mg^{2+} and Fe^{2+}), which combine with bicarbonate according to (Hellevang et al., 2006);

$$M^{2+} + 2HC0_3^- \rightarrow MCO_3 + H_20 + CO_{2,aq} \quad (3.4)$$

A large number of reactions might take place between fluid and rock, and only a few, relevant will be exemplified in the following. Reactions involving feldspars provide one possible way of immobilizing CO_2 through the fixation of carbon dioxide in carbonate minerals. For example, if the calcium end-member of the plagioclase series (anorthite) reacts with available H^+ in the aquifer fluid, Ca^{2+} can precipitate together with CO_2 as calcite (Rosenbauer et al., 2005);

$$CaAl_2Si_2O_8 + H_2CO_3 + H_2O \rightarrow CaCO_3 + Al_2Si_2O_5(OH)_4 \quad (3.5)$$

The precipitation of the carbonate mineral dawsonite ($NaAlCO_3(OH)_2$) from K-rich feldspars in saline solutions have been postulated by several authors (Gunter et al., 2004;Hellevang et al., 2006;Rochelle et al., 2008);

$$KAlSi_3O_8 + Na^+ + CO_{2,aq} + H_2O \rightarrow NaAlCO_3(OH)_2 + 3SiO_2 + K^+ \quad (3.6)$$

As divalent cations are usually few in solutions, dawsonite could be the major carbonate forming during CO_2 sequestration. But dawsonite is rarely observed in areas which have been exposed to CO_2 seepage. The explanation can be obtained from thermodynamic calculations, which indicate dawsonite instability as CO_2 pressure is reduced by leakage or dissipation. Therefore, CO_2 trapped in dawsonite is only favored in systems capable of maintaining a stable, high CO_2 pressure (Hellevang et al., 2005).

Some silicate minerals (e.g. *albite*) may also trap CO_2 as a dissolved species like bicarbonate;

$$7NaAlSi_3O_8 + 6CO_{2,aq} + 6H_2O \rightarrow Na - smectite + 6HCO_3^- + 10SiO_2 + 6Na^+ \quad (3.7)$$

The same trapping species results from the dissolution of carbonate minerals (Rochelle et al., 2008);

$$CaCO_3 + CO_{2,aq} + H_2O \rightarrow Ca^{2+} + 2HCO_3^- \quad (3.8)$$

Generally, the importance of silicates in terms of geological storage of carbon dioxide is a factor of their kinetics, amounts present and cation content. The dissolution kinetics determine the rate at which cations can be supplied to the solution at undersaturation (Hellevang et al., 2006). As the process of carbonate precipitation is fast, the extent of solid carbonate formation is mostly dependant on the rate of cation supply from silicate dissolution (Matter et al., 2007). Mg^{2+} and Fe^{2+}-ions available for carbonate precipitation are usually from phyllosilicate dissolution, while Ca^{2+}-ions can be provided by plagioclase dissolution (Hellevang et al., 2006).

The kinetic rate law for dissolution and precipitation of mineral *m* can be expressed by;

$$rate_m = A_m \cdot k(T)_m \cdot (a_{H+})^n \cdot \left[1 - \left(\frac{Q_m}{K_m}\right)\right] \quad (3.9)$$

where *A* is the reactive surface of mineral *m* per kg water, *k(T)* is the temperature dependent rate constant, a_{H+} is the proton activity, *Q* is the ion activity product and *K* is the equilibrium constant. The temperature dependant rate constant is given by;

$$k(T) = k_{25} \exp\left[\frac{-E_a}{R}\left(\frac{1}{T} - \frac{1}{298.15}\right)\right] \quad (3.10)$$

where k_{25} is the rate constant at 25°C, E_a is the activation energy, *R* is the gas constant and *T* is the temperature in Kelvin. In this rate expression, the pH dependency of the dissolution rate is expressed as the activity of the H^+ in solution raised to the experimentally derived power *n*.

Most silicate minerals show a similar trend in that their dissolution rates decrease with pH in the acid region, and increase with pH in the basic region. This behavior has proven challenging to explain theoretically, but attempts have been made based on reactions on the mineral surfaces (Blum and Lasaga, 1988).

The interaction between dissolved species and mineral surfaces involves exchange and adsorption on the mineral surfaces. The H^+ and OH^- concentrations at the surfaces resulting from these reactions affect the dissolution kinetics of most slightly soluble oxides and silicates (Xie and Walther, 1992). Whether the mineral surfaces will have a negative or positive charge, can be predicted based on their point of zero charge (pzc). The pzc of a mineral corresponds to the pH at which the mineral surfaces have a net neutral charge. In solutions with pH lower than the pzc of a given mineral, the mineral surfaces will be positively charged. Conversely, if the pH is above the pzc, the surface will have a negative charge (Lasaga, 1984). To complicate the picture, all charges arising from different cation sites of minerals should be considered. For aluminosilicates the minimum dissolution rate occurs at the pH where the sum of the absolute values of Al- and Si surface charges are at a minimum. The positive and negative charges correspond to adsorption of anions and cations, respectively. The weakening of cation-oxygen bonds at the mineral surfaces arising from bond polarization (Aagaard and Helgeson, 1982), increases the probability of surface detachment (i.e. dissolution) (Walther, 1996).

3.3 Geomechanical effects

3.3.1 Cap rock integrity

CO_2 injection may lead to pressure build up and temperature decrease, which may cause CO_2 leakage through the cap rock by capillary leakage or rock fracturing (Li et al., 2006). CO_2 diffusion through the cap rock is an extremely slow process, and is only considered important over geological time (Chiquet et al., 2007b). Capillary leakage occurs if the minimum pressure needed to displace the brine in the cap rock (*capillary breakthrough pressure,* P_c) is exceeded (figure 6) (Chiquet et al., 2007a).

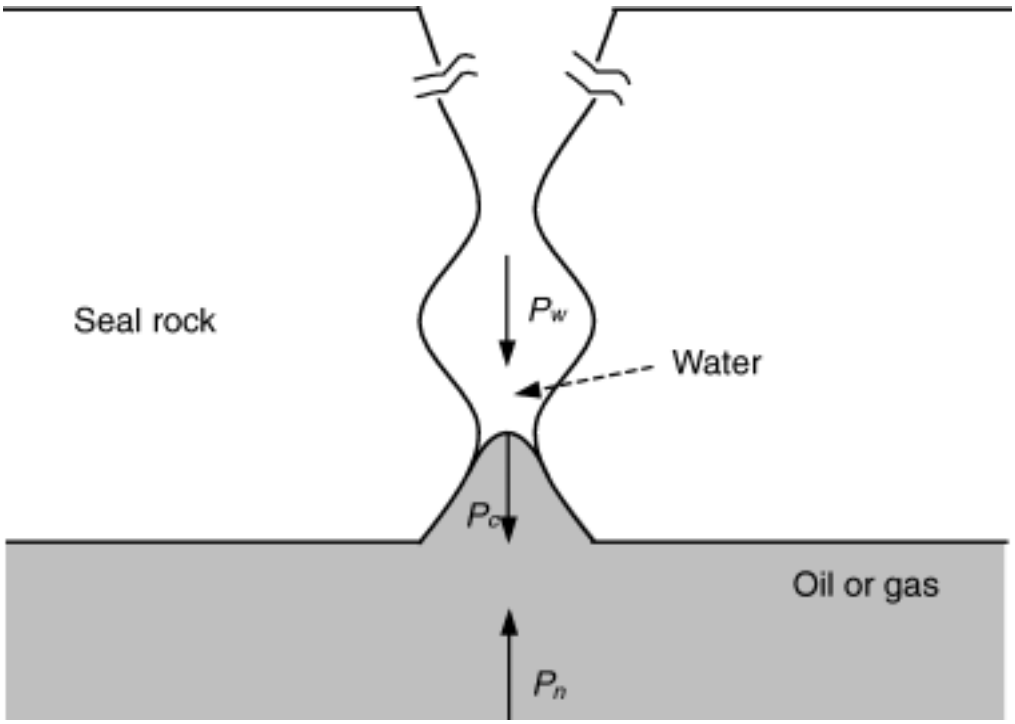

Figure 6: Capillary sealing mechanism of cap rock in pore throat where the capillary breakthrough pressure (P_c) is the difference between the hydrostatic pressure (P_w) of the brine and the CO_2 storage pressure (P_n). In this experiment, the lower oil fluid (oil and gas) consists of CO_2 (Li et al., 2005).

Since cap rocks overlying gas and oil reservoirs have proven the ability to prevent upward migration of hydrocarbons through geological time, it has been argued that they will be sufficient seals also after CO_2 injection. Recently however, Li et al. (2006) (*among others*) pointed out that since the interfacial tension (IFT) is much lower in the CO_2/water system than in the hydrocarbon/water system, the sealing capacity of the cap rock is significantly reduced after CO_2 injection. IFT (σ) is a result of the attractive forces of molecules acting at the

interface between fluids, and is closely related to capillary breakthrough pressure. The two are connected through the Laplace law (Chiquet et al., 2007b);

$$P_c = \frac{2\sigma \cos\theta}{r_p} \tag{3.11}$$

where σ is the IFT between CO_2 and water, r_p is the largest connected pore throat radius and θ is the contact angle between the mineral – brine – CO_2 - system. The general assumption has been that brine is a good wetting fluid (small contact angle) (Chiquet et al., 2007b). Recently however, it has been pointed out that the dense, supercritical CO_2 reduces the wettability of water on shale minerals (e.g. quartz, mica) (Chalbaud et al., 2007). Chiquet et al. experimentally examined the contact angle on quartz and mica under varying CO_2 pressures. They observed a 40-50º increase in the contact angle of mica and 15-25º increase for quartz over the pressure interval 0-11 MPa. This corresponds to lowering the sealing capacity by a factor of ~1.5. This wettability alteration was primarily attributed to a decrease in brine pH caused by CO_2 dissolution, as the electrostatic repulsion between the negative surface charges on the mineral/brine and brine/CO_2 interfaces are reduced at low pH (Chiquet et al., 2007a).

Quantitatively, the differences in IFT between brine/CO_2 and brine/hydrocarbons have been addressed by several authors (*e.g.* Chiquet et al., 2007b; Hildenbrand et al., 2004; Ren et al., 2000). Although Ren et al. only investigated IFT in *(CO_2 + CH_4) + water* systems, they clearly observed that the relative amounts of CO_2 and hydrocarbons affected the IFT (Ren et al., 2000). Hildenbrand et al. complemented their gas breakthrough experiments with a review of existing experimental data. At pressures from 6 – 20 MPa and temperatures below 71ºC, the IFT levels in brine/CO_2 are approximately half the values of water/hydrocarbon (Hildenbrand et al., 2004). Among pressure, temperature and salinity of the brine, pressure exerts the main control on the IFT (Chiquet et al., 2007b). Combining the effects of reduced IFT and increased contact angle, the replacement of hydrocarbons by CO_2 can reduce the capillary breakthrough pressure by a factor of ~3.

Translating the breakthrough pressure into storage capacity for aquifers is relatively straightforward. If the reservoir in which CO_2 is stored has a thickness h, the buoyancy forces driving CO_2 upwards are the product of the gravitational constant, the thickness of the aquifer and the difference between the density of brine and CO_2 ($(\rho_{water} - \rho_{CO2}) \times g \times h$). If the

buoyancy forces are greater than the cap rocks capillary pressure, CO_2 will enter the cap rock. The maximum height of CO_2 that can be stored can therefore be obtained from the simple inequality expression (Chiquet et al., 2007b;Chiquet et al., 2007a):

$$(\rho_{water} - \rho_{CO2}) \times g \times h \leq \frac{2\sigma \times \cos\theta}{r_p} \quad (3.12) \quad \text{and} \quad h \leq \frac{2\sigma \times \cos\theta}{r_p \times (\rho_{water} - \rho_{CO2}) \times g} \quad (3.13)$$

It should be mentioned that the density variations of CO_2 and water in the reservoir is not accounted for in these equations.

The low viscosity and high diffusion coefficient of supercritical CO_2 has made it a preferred agent in supercritical fluid extraction (SFE) (Spiteller, 1985). The ability to extract organic matter from rocks could potentially influence the sealing performance of the organic-rich claystone from the Troll East Field. Okamoto et al. (2005) treated siltstone from the Nagaoka injection test site (total organic matter content 0.4 – 1.3 wt %) with supercritical CO_2 to identify potential cap rock alterations caused by SFE. Even though the carbon and nitrogen levels, porosity and pore size distribution remained virtually unchanged after 150 days of treatment, significant permeability changes could not be excluded. If the minor amounts of organic matter dissolving hold grains together, the resulting pore structure alteration could drastically increase the permeability (Okamoto et al., 2005).

3.3.2 Creep mechanisms

The dissolution of minerals in the presence of acidified fluids, may lead to increased porosity. At the same time, weakening of the rock skeleton promotes mechanical compaction which can decrease the porosity. Among the different mechanical creep methods which could be involved in this process, pressure solution creep (PSC) is believed to play a major role (Le Guen et al., 2007).

Deformation of grains by pressure solution is driven by differences in chemical potential between high stress regions at grain contacts and low stress regions in the pores (Renard et al., 2005). Dissolved material from stress enhanced dissolution at grain contacts is transported through intergranular fluid film by diffusion. The precipitation of these solutes on the surface of grains in contact with the pore fluid, decreases the porosity (Gundersen et al., 2002). High

P_{CO2} fluids increase the rate of dissolution, which may increase the PSC induced strain and compaction in rocks.

3.3.3 Seismic velocities

Seismic surveys have already proven successful in terms of monitoring fluid changes in hydrocarbon reservoirs during oil production. Even though sequestration of CO_2 is a relatively new application, laboratory data and field experiments suggest that CO_2 influences the seismic properties to a degree which is seismically detectable (Yuh, 2003). Measurements on core samples indicate that the velocity of both compressional and shear waves can decrease by ~10 % (Wang et al., 1998;Wang and Nur, 1989). In addition, the seismic monitoring of the Sleipner field have shown a large increase in reflectivity and travel time-delay caused by CO_2 injection (Eiken et al., 2000).

Seismic velocities and amplitudes depend on the bulk and shear moduli of the rock the waves are propagating through, in addition to properties of the pore fluids. Bulk modulus is defined as the rate of hydrostatic pressure to volumetric strain, while shear modulus is the relationship between shear stress and shear strain (Goodman, 1989). Quantitatively the P- and S-wave velocities change with fluid properties in a manner described by the Gassmann equation. It states that the shear modulus of an isotropic, homogeneous and monominerallic rock under isostress conditions will stay constant during changes in the fluid properties. The bulk modulus of the rock however, depends on the bulk modulus, saturation and density of any fluids present. According to the Gassmann equation , the P- and S-wave velocities are given as (Gassmann, 1951):

$$V_p = \sqrt{\frac{K_{sat} + \frac{4}{3}\mu}{\rho_{bulk}}} \qquad (3.14) \qquad \text{and} \quad V_s = \sqrt{\frac{\mu}{\rho_{bulk}}} \qquad (3.15)$$

where K_{sat} is the bulk modulus of the saturated rock, μ is the shear modulus of the rock and ρ_{bulk} is the bulk density. From these expressions it is clear that the P-wave velocity is determined by both the bulk modulus and density of the fluid, while the S-wave velocity is only affected by the density of the fluid.

4 Previous experimental and modeling work

4.1 Similar experimental setups

Le Guen et al. (2007) examined the deformation of limestone and sandstone caused by injection of high and low P_{CO2} aqueous fluids. The experiments were preformed in a triaxial cell where a vertical stress of 16 MPa was imposed by a piston directly in contact with the sample. The horizontal confining pressure was 10.2 MPa, the temperature 40ºC and the salinity of the brine 0.01 M NaCl. The fluids were injected in the bottom of the sample at constant flux (0.005 ml/min) using a high pressure liquid chromatography pump. The high pressure CO_2/brine mixture (8 MPa) was prepared in an autoclave. After filling the autoclave with CO_2 ice, they injected saline solution ([NaCl]=5.8 g/l) until the desired pressure was obtained. The mixing of CO_2 and water was considered satisfactory after one week as the heavier water was injected at the top and the autoclave was equipped with a impeller (Le Guen et al., 2007). Furthermore, the exchange kinetics over the interface have previously been demonstrated to rapidly equilibrate supercritical CO_2 and water (Carroll and Knauss, 2005).

The experimental setup used by Bateman et al. (2005) display some features similar to the setup used in this study. Their reacting material was placed in a 100 cm high column inside a large heated pressure vessel, with the confining pressure controlled by a syringe pump. CO_2 and brine were equilibrated at 70°C and 10 MPa using a second syringe pump which was also connected to the top of the column. Fluid flow was controlled by a third syringe pump connected to the bottom of the column. A 30 cm^3 titanium floating piston pressure sampler inserted between the outlet of the pressure vessel and the syringe pump applying the back-pressure, allowed fluid samples to be taken. Analytically the solids were examined using SEM and gas sorption on clean surfaces to determine the surface areas. In addition to pH measurements, the fluid samples were analysed for both major and trace cations using inductively coupled plasma-optical emission spectroscopy (ICP-OES) and for anions using ion chromatography (Bateman et al., 2005).

4.2 Geochemical experiments and models

Fluids leaving the triaxial cell of Le Guen et al. were constantly collected, and analyzed by ICP-AES every second day. As the pressure was reduced in the samples upon analysis, nitric acid was added to prevent precipitation. A Triassic arkosic sandstone was exposed to 70 days of high P_{CO2} (8.3 MPa) injection, followed by 50 days of no-flow. During fluid injection, the aqueous concentrations of Ca, Si and Sr decreased, while Mg increased. After the 50 days without flow, a second injection period was started with an injection rate 10 times the original one. This rate was later lowered to 2 times the original rate, thereby completing an increase-decrease sequence simulating uplift followed by burial. All the steady state concentrations decreased after the injection rate was increased, whereas decreasing the injection rate again led to increasing concentrations in a step-like manner. The overall higher concentrations of Mg and Ca compared to Si were attributed to a well-known decrease in reactivity from dolomite and calcite to quartz (Le Guen et al., 2007).

The synthetic mineral composition in the column of Bateman et al. (table 1) was flushed with CO_2/brine at a constant flow rate of 0.021 cm^3/min for 7.5 months. After the 7.5 months, the mineralogical investigation indicated significant dissolution of calcite and dolomite in the zone close to the inlet of the column. Between 10 and 20 cm from the column inlet, the proportions of calcite and dolomite returned to those originally present. The surface area analysis showed a slight increase at the inlet of the column, whereas the small decrease in surface area for the rest of the column was attributed to instrumental inaccuracy (Bateman et al., 2005).

Table 1: Starting material in the experiment of Bateman et al. (2005).

Synthetic mineral composition	
Phase	*Weight (%)*
Quartz	80
Labradorite	10
K-feldspar	1
Albite	2
Calcite	3
Dolomite	1
Muscovite	2
Chlorite	1

Kaszuba et al. (2003) injected CO_2 at 200ºC and 20 MPa into an aquifer-aquitard system composed of arkosic sandstone and shale, respectively. The injection period lasted for 80 days, and the purpose was to examine fluid-rock interactions with focus on carbonate mineral precipitation. This was done by investigating reaction textures on aquifer and aquitard minerals, carbonate minerals precipitated and changes in brine chemistry. In addition to precipitated magnesite, amalcine mica and clay minerals, their results showed textures on

silicate minerals which indicated significant reactions. The arkosic sandstone serving as the aquifer was composed of equal amounts of quartz, oligoclase and microcline. On the edges of pits and open fractures of the quartz grains, abundant clay minerals were observed using SEM. Smectites not present on the initial oligoclase were present in abundance on the surfaces and cleavages of the CO_2 exposed oligoclase grains. While Kaszuba et al. observed differential etching on the microcline surfaces, the same phenomenon was not observed for the oligoclase. For the shale (mostly composed of quartz and clay minerals), they saw clay coatings draping across surfaces and small cavities. Subhedral halite crystals had accumulated on the shale surfaces, something which may have resulted from brine trapping during quenching. The levels of major ions in the brine stabilized within the first 670 hours after start of injection. Whereas the Na-and B-concentrations stayed close to the initial concentrations, K-, Mg- and Cl-levels decreased by 15-20 %. Ca increased by approximately 30 %, while Si increased from zero to a level just below what was calculated based on quartz solubility. The concentrations of SO_4 and Fe did not stabilize and continued to change throughout the duration of the experiment (Kaszuba et al., 2003).

Gaus et al. (2005) examined the cap rock effects of CO_2 injection at Sleipner by reactive transport modeling of dissolved CO_2 in the cap rock. As it is considered unlikely that capillary leakage will occur through the Nordland Group shales overlying the Utsira sand at Sleipner, only reaction kinetics and diffusive transport was included in the model. The initial composition of the cap rock entered into the model is presented in table 2.

Table 2: Initial cap rock mineralogy used by Gaus et al. (2005).

Nordland shale composition	**Mass percent**	**Minerals entered in the model**
Plagioclase	12.3	*Albite* *Anorthite* *Oligoclase*
Calcite	1.0	*Calcite*
Quartz	21.5	*Chalcedony*
Chlorite	4.1	*Clinochlore-7A*
Mica/Illite	24.7	*Illite*
Kaolinite	18.0	*Kaolinite*
K-feldspar	2.1	*K-feldspar*
Pyrite	2.8	*Pyrite*
Siderite	1.6	*Siderite*
Smectite	8.8	*Smectite-high-Fe-Mg*
Mixed layer clay	1.4	*Not used*
Total	98.3	

The Oseberg formation water was equilibrated with the cap rock mineralogy by geochemical modeling as a starting point. Under 37°C and approximately 10 MPa, two types of batch models were done; one assuming instantaneous thermodynamic equilibrium and one incorporating the kinetics over 15 000 years. The latter

showed a fairly fast dissolution of calcite after the initial pH drop from 7.7 to 3.0. Relatively small amounts of calcite were needed to stabilize the pH at 4.5. In the long run, kaolinite and calcite formed from the dissolution of albite combined with Ca^{2+} ions from the initial dissolution of carbonates according to;

$$2NaAlSi_3O_8 + CO_2 + 2H_2O + Ca^{2+} \rightarrow 4SiO_2 + CaCO_3 + Al_2Si_2O_5(OH)_4 + 2Na^+ \qquad (4.1)$$

As the Ca^{2+} concentration decreased with time, the model predicted a shift from calcite to dawsonite formation. However, the total amounts of carbonate minerals formed over the 15 000 years were minor, and the porosity of the cap rock remained virtually unaffected by the dissolution/precipitation reactions. In the thermodynamic batch model an unrealistically high reactivity was revealed by a significant reduction in pure H_2O levels. Overall smectites and illite dissolved, while chalcedony, kaolinite and large amounts of carbonates (magnesite, dolomite, dawsonite and siderite) precipitated.

The main lesson learned from the diffusive transport model was that the process is very slow, even when the effective diffusion coefficients were in the high end of their calculated range. Replacing albite with the more reactive anorthite retarded the CO_2 migration as the CO_2 rapidly reacted with the anorthite in the lower part of the cap rock (Gaus et al., 2005).

Suekane et al. (2005) examined the behavior of supercritical CO_2 in contact with water in a porous media. Using magnetic resonance imaging (MRI) they were able to directly observe the distribution of supercritical CO_2 injected into a packed bed of glass beads (70 μm in diameter). After completely filling the pores of the packed bed with water, supercritical CO_2 was injected at 11 MPa injection pressure and 10 MPa back-pressure. 5 minutes later they stopped the injection and observed that the water saturation in most regions of the bed had been reduced to 0.3-0.5. The higher concentration of water observed near the centre of the bed, was classified as trapped water. About four CO_2-rich channels penetrated this trapped water, and inhomogeneous distribution of water saturation remained for about 15 minutes. As water is heavier than supercritical CO_2, the downward movement of water after injection stop was observed as increasing water saturation with time from the upper part of the bed.

4.3 Geomechanical experiments

The axial displacement sensors in the experiment of Le Guen et al. indicated that the compaction response of the sandstone after injection start, was very rapid. After 1 day the deformation rate was already at the limit of what could be measured. The rapid compaction was believed to be caused by a sudden increase in pore fluid pressure. This pressure increase initiated grain-grain rearrangement and grain-grain sliding, which led to the compaction. A porosity increase in the sandstone of 1.7 % was estimated based on the amount of dolomite and calcite cement dissolved (Le Guen et al., 2007).

Capillary breakthrough pressure tests for supercritical CO_2 have been performed with somewhat different approaches by Li et al. (2005) and Springer and Lindgren (2006), among others. Li et al. experimentally investigated the breakthrough pressure of supercritical CO_2 for Midale evaporites (Weyburn cap rock). These rocks have very low porosity and permeability. Using a constant backpressure of 7.3 MPa and the in-situ temperature of 59ºC, they increased the injection pressure in steps of 0.5 – 1.0 MPa. For samples with porosities ranging from 0.3-0.7 %, they got breakthrough at differential pressures from 11.2-5.0 MPa (Li et al., 2005).

Springer and Lindgren determined capillary entry and breakthrough pressure of the Nordland shale cap rock under reservoir conditions. With a confining pressure of 15.3 MPa, they started with equal pore pressure in the top and bottom of their samples (10.3 MPa). Next, the downstream pressure was decreased in steps of approximately 0.3 MPa until upstream CO_2 moved into the sample. This occurred after the downstream pressure had been reduced to 8.6 MPa, resulting in a breakthrough pressure of 1.7 MPa (Springer and Lindgren, 2006).

The laboratory tests on V_p and V_s preformed by Wang et al. (1998) were motivated by the discrepancies between theoretically derived and observed seismic velocities after CO_2 injection at the McElroy field, Texas. The higher velocities observed compared to the ones predicted using the theory of Gassmann, were attributed to a more significant pore pressure increase following the CO_2 injection than what was initially assumed. Therefore, they flooded eight dolostone cores with CO_2 under McElroy pressure and temperature conditions and examined the velocities as functions of CO_2 saturation and pore pressure. Their experimental data suggested 3.0 – 10.9 % decrease in V_p and 3.3 – 9.5 % decrease in V_s. The results obtained from Wang et al. indicated that while V_p is sensitive to changes in both CO_2

saturation and pore pressure, V_s is only sensitive to pore pressure changes. Based on this, they suggested that S-wave velocities can be used to separate the effect of pore pressure increase from the combined effect of pore pressure build up and increasing CO_2 saturation. This can possibly be used to separate between reservoir zones with CO_2 and high pressure zones without CO_2 (Wang et al., 1998).

5 Experimental setup

5.1 Flow through cell at NGI

As allready mentioned, the experimental setup at NGI was somewhat altered during the thesis. Initially the aim was to inject CO_2/brine into a claystone cap rock, and examine the geochemical and geomechanical effects. Fluids were to enter and exit the shale via two filters connected to the top and bottom of the sample, respectively. Perforated plates between the sample and filters would ensure an even spatial distribution at the interfaces. The filters were both connected to two different *TELEDYNE ISCO 260 D* syringe pumps (labeled *pump A* and *pump B*). These pumps are designed specifically for refilling under high pressures to handle supercritical fluids, and have pump volumes of 266 cm^3. The pumps are equipped with pressure control to approximately 50 MPa and flow rates from sub-micro liter to 100 ml/min. As the accuracy of the internal pressure sensors in the pumps were considered to be too low, two external pressure sensors mounted near the pump outlets controlled the pumps pressures (figure 7).

Figure 7: The two syringe pumps used for fluid transport through the claystone.

The two ISCO pumps and a CO_2 bottle with a dip tube were both connected to a scuba bottle (hereafter called *mixing chamber*), where the mixing of CO_2 and water took place. The mixing chamber could tolerate working pressures up to about 23 MPa, and had a volume of 1 500 cm^3. As the mixing chamber would contain vertically separated phases, it was equipped with two wires; one reaching the heavier phase near the bottom and one reaching the lighter phase close to the top of the bottle, respectively. The connection between the pumps, the two wires from the mixing chamber and the top and bottom of the cell was realized through two 5-way valves (figure 8). The valves were labeled A and B as they were always open to pump A and B, respectively.

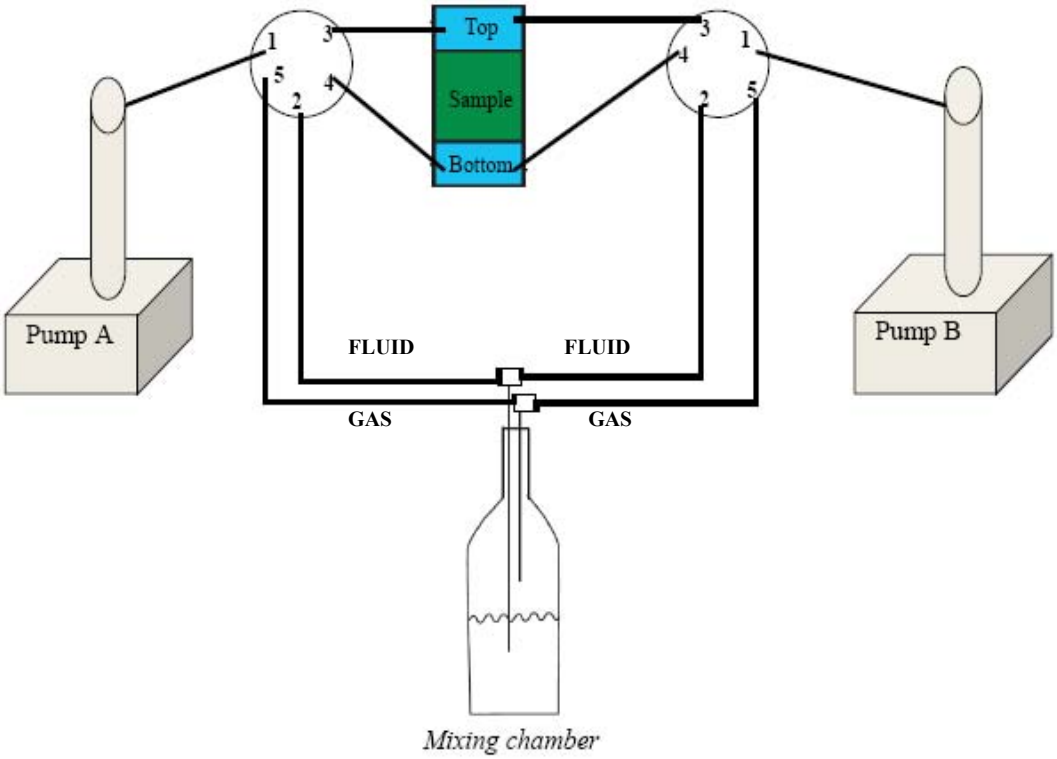

Figure 8: Two 5-way valves connected the pumps, mixing chamber and the top and bottom of the sample.

Two pressure sensors placed near the bottom and top filters allowed the pore pressure in the sample to be constantly logged. The confining pressure in the cell was controlled by a hand pump connected to an accumulator. A pressure sensor located close to the cell inlet enabled an accurate logging of the cell pressure.

The axial and radial deformation of the sample was measured using three Linear Variable Differential Transformers (LVDTs); two in the axial (*Schaevitz MHR 50*) and one in the radial direction (*Schaevitz MHR 25*). The axial measurements were 180º apart, while the radial deformation sensor was located midway between top and bottom of the sample. LVDTs are electromagnetical transducers capable of registering very small displacements of objects they are mechanically connected to. The rectilinear motion of those objects induces changes in the electrical signal created. The LVDT contains one primary (P1) and two secondary (S1 and S2) windings, and the transfer of current between the primary and secondary windings are controlled by the position of a magnetic core. The windings are located inside a hollow high permeability magnetic shield, and a tabular core is free to move axially in the center of the

magnetic shield (figure 9). If the core is located midway between S1 and S2, the flux coupled to each of the secondary windings are equal. Hence, the voltages induced (E1 and E2) are equal and the differential voltage output (E1 – E2) is zero. As the core moves away from the center, the result is an increase in the induced voltage of the nearest secondary winding and a decrease in the other. The differential voltage output reveals the position of the core relative to a reference point (Trietley, 1986). All three LVDTs were attached to a metallic ring surrounding the sample (figure 10). The ring was held midway between the top and bottom of the sample by two connections to the membrane covering the shale. To give recordable readings, the LVDTs were connected to *Schaevitz ATA 2001* analog transducer amplifiers.

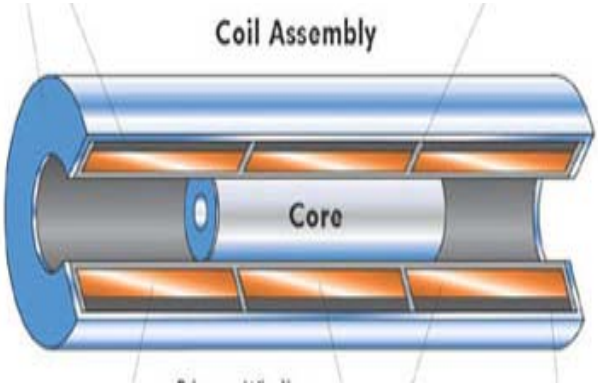

Figure 9: The tabular core is free to move inside the hollow magnetic shield of LVDTs (MacroSensors, 2008)

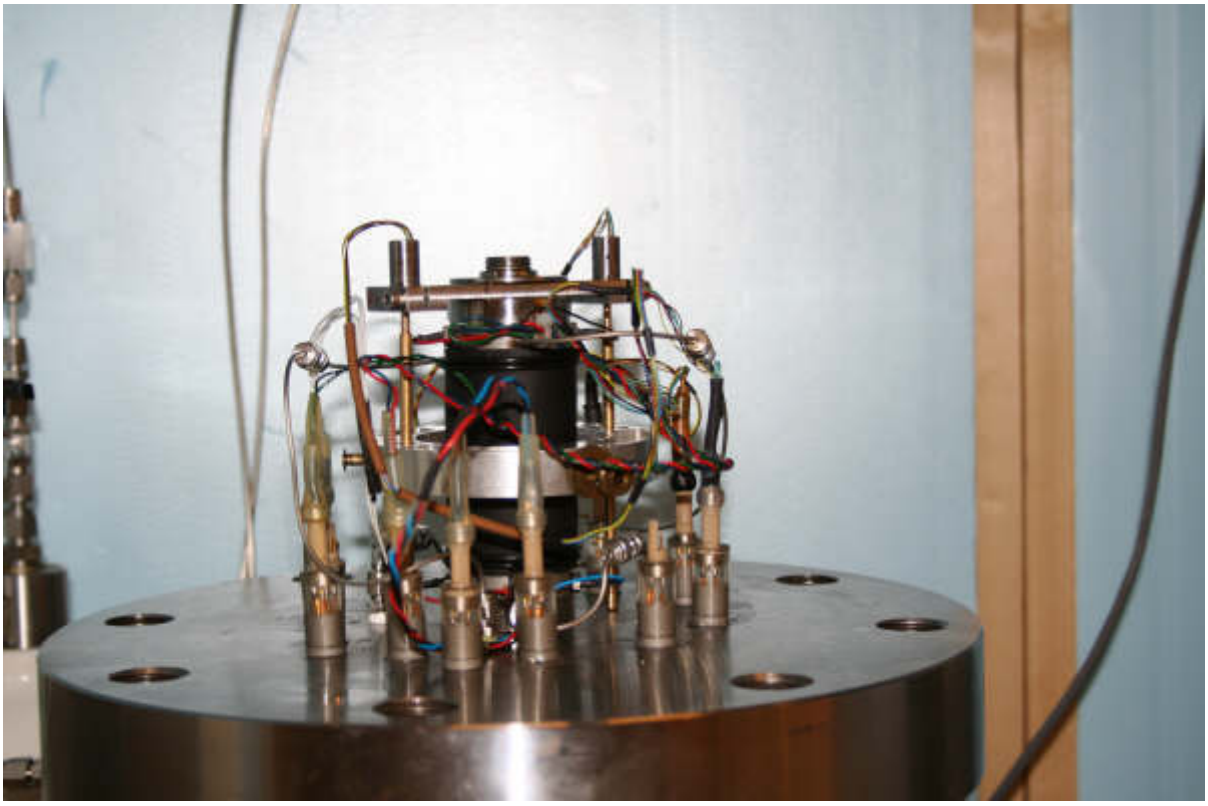

Figure 10: The cell bottom with the sample in a black nitrile membrane. Two axial and one radial deformation sensor were connected to a metallic ring surrounding the sample.

The transit time of acoustic compressional (V_P) and shear (V_S) waves were measured using piezoelectric transducers, placed inside the top and bottom filters. The transducers can convert electrical pulses into mechanical vibrations and the returned mechanical vibrations back into electrical energy. Both P-and S-waves were shot from the top to the bottom. During the planned injection of CO_2/brine into the claystone, it was decided that a minimum of 50 velocity measurements should be taken over the time period it would take for the new fluid to replace the water already in the sample (*~4 pore volumes*).

A 30 cm^3 pressure-tolerant chamber inserted between pump B and the sample allowed water samples to be taken (figure 11). Two open/closed valves were inserted on both the side of fluid entrance and fluid exit. By closing off all four valves, the chamber could be removed from the cabinet while keeping the pressure constant in both the chamber and the rest of the system. Before CO_2/brine entered the sample, the chamber was supposed to be filled with oil. The oil was chosen because of its resistance to mix with the water phase, enabling undisturbed water samples to be collected. The CO_2 content in the water could be measured by releasing the pressure in the chamber against a water cylinder with an opening in one end. The volume of water forced out of the cylinder would then correspond to the amount of CO_2 in the water. Next, the water could be analyzed for pH and ion content.

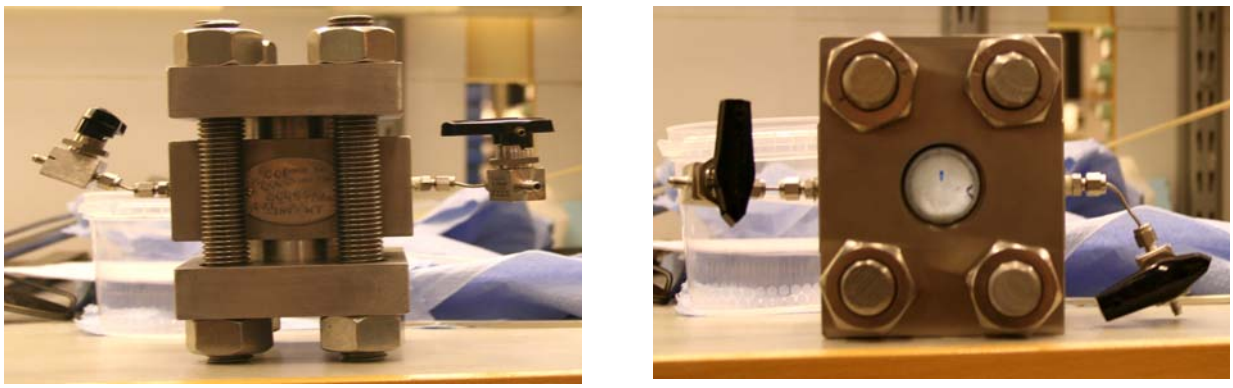

Figure 11: The pressure-tolerant chamber from which water could be sampled and analyzed.

As both permeability and solubility are closely related to temperature, efforts were made to keep the temperature constant. The cell, syringe pumps and mixing chamber were therefore placed inside a *2*x*1*x*1* meter cabinet. The cabinet walls were made of polystyrene boards (*STYROFOAM 300 A-N*), which can withstand working temperatures up to 80ºC. The desired temperature was entered into a digital temperature controller connected to a 400 watts heat source. A thermometer placed inside the cabinet and connected to the temperature controller

registered the temperature, and regulated the energy emitted by the heat source accordingly. Distribution of heat throughout the cabinet was secured by a fan placed inside it. Even so, as the possibility of temperature gradients arising inside the cabinet and cell could not be excluded, two thermistors were placed inside the cell; one near the top of the sample and one near the end. One additional thermistor was placed near the bottom of the cabinet to locate potential gradients in the vertical direction. For safety reasons a temperature regulator was also placed inside the cabinet, making sure energy supply to the heat source was stopped if the temperature increased too much.

As the need for constant temperature called for a closed cabinet throughout the experiment, a "valve-panel" was placed near one of the cabinet walls (figure 11). From this all connections involving the pumps, the top and bottom of the cell, the mixing chamber and the CO_2 bottle could be handled. An opening in the wall allowed for the different valves to be operated while keeping the cabinet closed.

As already mentioned, the experimental aim shifted during this thesis. The experimental design did not however change; the only difference was that the chamber in which CO_2 and brine were to be mixed was no longer included in the procedure.

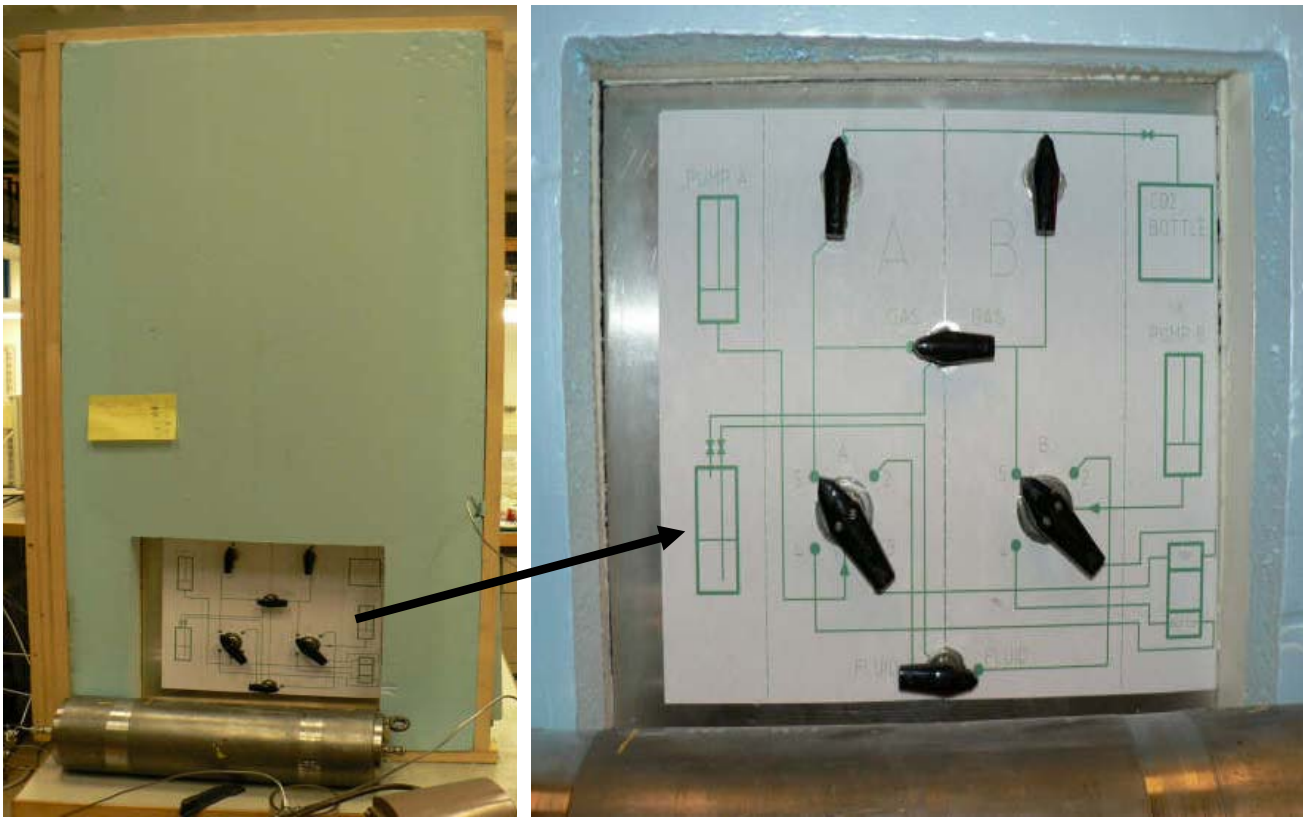

Figure 12: The valve-panel placed on one of the short walls of the polystyrene cabinet.

5.1.1 Data logging and processing

The voltage outputs from the different sensors were constantly logged in Solartron data logging system. The conversion from voltage to millimeter or Pascal was realized through numerous equations, which also contained the various calibration factors. In addition to the direct readings from the sensors, certain parameters derived from the deformation measurements were constantly calculated (table 3). This included differential pressure, mean axial deformation and horizontal (ε_h), vertical (ε_v) and octahedral (ε_{oct}) strain. The differential

Table 3: Direct and derived parameters constantly logged in Solartron data logging system.

Parameters logged in Solartron	
Direct readings	**Derived parameters**
Axial Deformation 1	*Mean Axial Deformation Horizontal, Vertical and Octahedral Strain*
Axial Deformation 2	
Radial Deformation	
Temperature $Cell_{BOTTOM}$	
Temperature $Cell_{TOP}$	
Temperature cabinet	
Pore $Pressure_{BOTTOM}$	*Differential Pressure*
Pore $Pressure_{TOP}$	
Pressure Cell	
Pressure ISCO pumps	
Volume and Flowrate ISCO pumps	

pressure was found subtracting the average pore pressure from the cell pressure. The strains were found in milistrain (mS) using the formulas:

$$\varepsilon_v = \frac{Ax_{mean}}{h_i} \tag{5.1}$$

$$\varepsilon_h = \frac{R_{def}}{d_i} \tag{5.2}$$

$$\varepsilon_{oct} = \varepsilon_v + 2\varepsilon_h \tag{5.3}$$

Where Ax_{mean} is the average axial deformation (in mm), R_{def} is the radial deformation (in mm), h_i is the initial height of the sample (in mm) and d_i is the initial diameter (in mm). The outputs from Solartron were entered into files at specified time intervals. Unless special conditions called for a shorter logging interval, measurements were usually taken every 20 minutes.

5.2 Batch reactor at UiO

Small amounts of claystone material sampled close to the plug used in the experiment at NGI were taken to the University of Oslo (UiO) for batch experiments in a flow through reactor connected to a controller (*PARR TM*). The different pH solutions and powdered material was entered into a 100 cm^3 steel vessel, which was then properly closed with six cap screws in a split-ring cover clamp. The vessel was surrounded by a hollow cylindrical heater with the same diameter. The heater gave off energy according to the values entered on the controller unit. A stirrer capable of 1 700 rpm mounted on top of the vessel ensured a proper mixing of the solids and the fluid. Water was constantly flushed through the part overlying the vessel, to prevent overheating of the system.

Figure 13: The reactor used in batch experiments at the University of Oslo.

6 Characterization of material used in the experiments

The shale material used in the experiment comes from the Troll East field. The Troll field is located approximately 65 km off the coast from Kollsnes, in the northern part of the North Sea. The seal peel, from which the sample used in this study is taken, belongs to the Upper Jurassic Draupne Formation and was found 1360 meters beneath sea level. Being a part of the Viking Graben which contains several major source rocks in the North Sea, the Draupne Formation has been thoroughly described in several studies (Isaksen et al., 2002;Isaksen and Ledje, 2001a;Justwan et al., 2005). The development of the Viking Graben began with rifting and thermal subsidence during late Perm – early Triassic. The main rifting event of this northward trending graben system however took place during late Jurassic – early Cretaceous (figure 14). During this time sub-basins and large rotational fault blocks cut by several faults was formed. The establishment of the rift system together with eustatic sea level rise led to widespread transgression and deep-water sedimentation (Isaksen and Ledje, 2001b). Finely laminated shales identified within the Draupne Formation indicate the absence of grazing or burrowing organisms under anoxic bottom water conditions. As the waters had little or no correspondence with adjacent ocean waters, there was restricted oxygenation and mixing (Justwan and Dahl, 2005). Average levels of total organic carbon (TOC) in the Draupne Formation is between 5 – 10 wt % (Dahl, 2004;Knudsen et al., 1988). The marine shales are in places interbedded with sandstones and siltstones, providing an efficient hydrocarbon plumbing system.

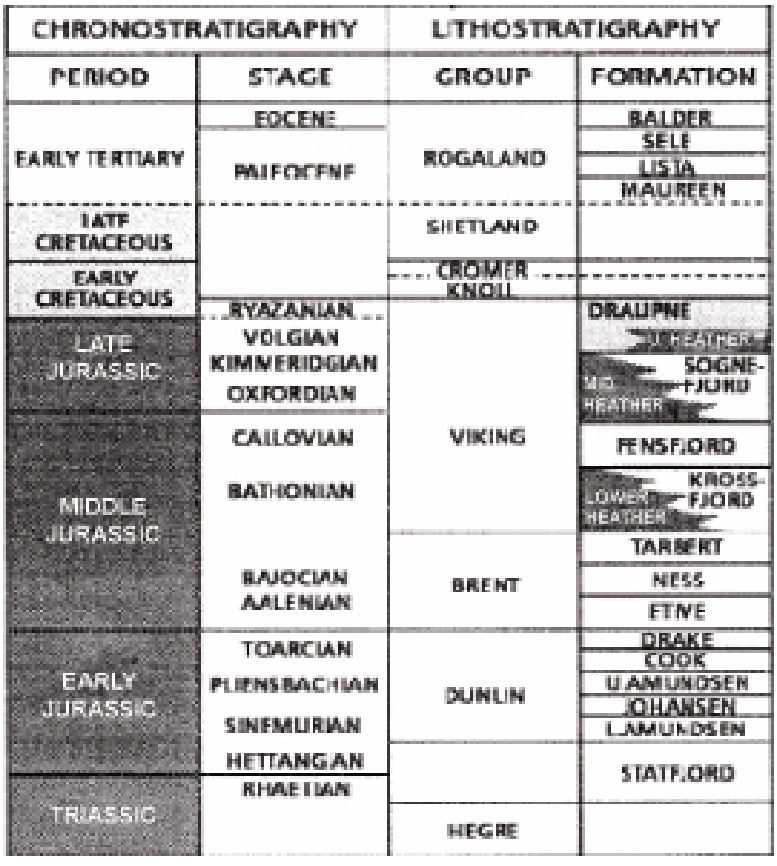

Figure 14: Chrono- and lithostratigraphy of the Troll Field (Gibbons et al., 1993).

The sandstone formations in the Troll field (Krossfjord, Fensfjord and Sognefjord Formations) situated on the Horda platform on the eastern margin of the Viking Graben (Clausen et al., 1999), are all considered suitable for underground geological storage of CO_2. These sandstones are overlain by claystones of the Draupne Formation, which in certain areas are several hundred meters thick. As the aquifer – cap rock system at Troll has already been identified as a potential storage location for carbon dioxide (Bøe et al., 2002), the use of Draupne claystone in this study appears reasonable. Even though the much deeper Johansen Formation is currently the most probable injection formation at the Troll Field, the Draupne Formation will still constitute one of the sealing agents for potential CO_2 injected.

Forty-five claystone seal peels from the Troll Field arrived at NGI in the beginning of 1998. Of the ones still remaining in 2007, plug B of seal peel number 40 from 1361.50 – 1362.00 meters below sea level was chosen in this study. In a general visual description of the seal peel made ten years ago, it was said to contain several visible horizontal fractures. As the fractures did not show any indication of shear displacement along them, they were believed to result from unloading during sampling or drying after sampling. Lithologically it was classified as a homogeneous, black claystone. The salt content in the pore water was determined by placing some crushed material in a known amount of distilled water. After the salt in the crushed specimen had dissolved in the water, the electrical resistance was measured. Not considering all the different salts present in the water, the resistance corresponds to a certain amount of NaCl. Next, the amount of equivalent NaCl in a water volume corresponding to the natural water content was calculated ([NaCl] = 57g/l). The swelling properties were examined by placing a piece of the sample in fresh water for 24 hours. No swelling was observed (Berre, 1998).

Since 1998, the material has been kept in a cooling room under moderate axial load. Together with a moist soft paper, the sample was placed inside two plastic bags to prevent it from drying out. Even so, numerous salt crystals were seen on the surface of the plug when the sample was unwrapped ten years later, indicating water loss. To quantify the water loss during storage, a small piece of the rest material was weighted before and after 24 hours of drying at 100ºC. The water content was found to have decreased from ~ 15 % in 1998 to 11.5 %. After removing the salt crystals on the surface of the sample with a file, the approximately 10 cm high plug was cut in two. For the experiment in the flow cell, a specimen height of 40 mm

was considered the best compromise between flow distance and height needed for P & S measurements. As the plug was cut in two, the upper part fractured along several horizontal/subhorizontal fracture planes. This fractured half was used for XRD, SEM, autoclave experiment and index testing.

Upon Scanning Electron Microscope (SEM) analysis, the parts of the core sample to be investigated went through freeze drying (lyophilization) to preserve the original structure. First they froze immediately when exposed to liquid nitrogen and next the frozen water sublimed directly in a vacuum container (CHRIST ALPHA 1-4) under the right temperature. One vertical and three horizontal surfaces were investigated. During SEM inspection, a beam of electrons is focused on a spot volume of the specimen. The bombarding primary electrons dislodge secondary electrons from the specimen itself, which are collected and translated into a signal. To produce the SEM image, the electron beam is swept across the examined area, giving several such signals. Some of the primary electrons are reflected from the specimen and can be used in backscatter electron imaging. The yield of the collected backscattered electrons increases with the specimen's atomic number, making the technique useful in distinguishing between the different minerals.

The Scanning Electron Microscope clearly revealed salt crystals on the horizontal surfaces (see *Appendix E*). The presence of barium sulfate was attributed to contamination during drilling. The clay minerals displayed planar surfaces and relatively high Al-, Si-, O- and Mg-content. On the vertical cross-section, one layer was distinctively different from the rest of the surface. Upon closer examination, this layer demonstrated high content of calcium and sulfur. The rest of the vertical spectrums showed the high Al-, Si-, O- and Mg-content described for the clay minerals in the horizontal cross-section. Relatively large fractures could be seen on both the horizontal and vertical surfaces (see *Appendix E*).

A few grams of the claystone material were crushed to powder and examined using X-ray powder diffraction (XRD). XRD is an instrumental technique capable of identifying crystalline materials. It benefits from the three-dimensional structure of minerals, which is defined by regular repeating planes of atoms that form a crystal lattice. When a focused X-ray beam interacts with these planes of atoms, part of the beam is diffracted. The distance between the planes of the atoms (d) that constitute the examined sample, can then be found using Bragg's law;

$$n\lambda = 2d \sin\theta \tag{6.1}$$

where the integer n is the order of the diffracted beam, λ is the wavelength of the incident X-ray beam and θ is the angle of incident of the beam. Since λ is known and θ is constantly measured, the d-spacings can be readily calculated. The characteristic set of d-spacings generated in a typical X-ray scan provides a unique fingerprint of the minerals present in the sample (Moore and Reynolds, 1989).

XRD (see *Appendix D*) was performed on both the bulk sample and on the clay fraction (>2 μm), which was separated from the rest of the sample by gravity settling of particles in suspension. In addition to the "full-scale" XRD from 2 – 50 °2θ, a slow scan was also done from 26 – 28.5 °2θ. The latter made it easier to distinguish between quartz, K-feldspar and plagioclase. Three separate XRD's were preformed on the clay fraction after they had been air-dried, treated with ethylene glycol and heated to 500 ºC, respectively. Ethylene glycol effectively caused the smectites present to swell, whereas the water content in these minerals were removed when they were heated. As a result, the smectite peak from the ethylene glycol treated sample collapsed under heat. To separate the kaolinite and chlorite in the clay fraction, a slow scan was performed between 24 – 26 °2θ.

The XRD results were used to give a semi-quantitative composition of the sample. The weight percent of a mineral present can be obtained from the area underneath its distinct peak divided by the total area underneath all distinct peaks in the sample. Furthermore, this ratio can be multiplied by a weight factor related to the intensity of the quartz peak. As choosing to neglect or include these weight factors appears trivial and determined by the researcher, it was decided to calculate weight percents both with and without weight factors (see *Appendix D*). First, the weight percent of "quartz", "clay minerals", dolomite/ankerite and pyrite were calculated from the bulk XRD. K-feldspar, plagioclase and quartz were then separated using the slow scan. The sum of the weight percent of these minerals should equal the percent of "quartz" from the bulk XRD. Smectite, illite/muscovite and kaolinite/chlorite contents were calculated from the ethylene-glycol treated clay sample. Finally kaolinite and chlorite were separated from the last slow scan. It should be kept in mind that neglecting the weight factors in weight percent calculations may lead to an overestimation of the carbonate content.

During the experimental work, the sample and some additional adjacent material was water saturated in an exicator (see *chapter 7*). The additional material was completely submerged in water on a scale after the exicator, allowing the volume of the material to be calculated. Furthermore, the mass of the material was found after drying at 110ºC for 24 hours. Together with the mass of the water saturated sample and the density of the saline water solution, the porosity and bulk density could be derived. Calculations indicated a relatively high porosity of 35 % and a sample density of 1.79 g/cm^3.

In addition, approximately 3.8 grams of the material was kindly taken to the Cergy-Pontoise University, France, for Mercury Intrusion Porosimetry (MIP) by Matthieu Angeli. In MIP dry samples are put under vacuum and surrounded by mercury. As mercury does not wet the sample spontaneously, pressure is needed to force mercury into the empty pores. The pressure was increased in steps from 0.003 – 200 MPa, and the volume of mercury intruded at each step registered. The pressure and corresponding pore radius are connected through the Washburn equation (Angeli, 2007);

$$Pc = -\frac{2\sigma \times \cos\theta}{r} \tag{6.2}$$

The method is based on the cylindrical pore model, meaning that the radius of the pore is considered equal across the full length of it. A large pore with a small entry diameter will therefore be associated with the higher pressure needed to intrude the entry of the pore.

The test preformed on the Draupne claystone showed a porosity of 21.0 %. The resolution of the MIP prohibits the detection of pore diameters smaller than 6.0×10^{-13} m. The 21 % porosity is therefore only calculated based on pores with diameter greater than this. The median pore diameter was found to be 27.5×10^{-9} m ($r = 13.75 \times 10^{-9}$ *m*).

An estimation of the capillary breakthrough pressure range for CO_2 in the Draupne claystone can now be obtained from the median pore radius. Assuming that the median pore radius is a measure of the largest connected pore radius in the sample, a breakthrough pressure range for somewhat different IFT and contact angles can be calculated. Cos θ can be expected between 0.9 – 0.75 (Chiquet et al., 2007a). An IFT range between 20 – 40 mN m^{-1} is based on previous work (Kemp et al., 2002;Kvamme et al., 2007);

$$Maximum\ P_c = \frac{2 \cdot (\cos\theta)_{\max} \cdot \sigma_{\max}}{r_p} = \left(\frac{2 \cdot 0.9 \cdot 40 \times 10^{-3}}{13.75 \times 10^{-9}} \right) Pa = 5.24 \times 10^6\ Pa = \underline{5.24 MPa} \quad (6.3)$$

$$Minimum\ P_c = \frac{2 \cdot (\cos\theta)_{\min} \cdot \sigma_{\min}}{r_p} = \left(\frac{2 \cdot 0.75 \cdot 20 \times 10^{-3}}{13.75 \times 10^{-9}} \right) Pa = 2.18 \times 10^6\ Pa = \underline{2.18 MPa} \quad (6.4)$$

$$Mean\ P_c = \frac{2 \cdot (\cos\theta)_{mean} \cdot \sigma_{mean}}{rp} = \left(\frac{2 \cdot 0.825 \cdot 30 \times 10^{-3}}{13.75 \times 10^{-9}} \right) Pa = 3.60 \times 10^6\ Pa = \underline{3.6 MPa} \quad (6.5)$$

7 Experimental procedure

7.1 Flow through cell at NGI

Initially the LVDTs were calibrated according to normal calibration procedures at NGI. This means that the sensors are locked in one position and a magnetically permeable stick is displaced a known distance inside the hollow bore of the coil. The voltage outputs at the different distances are used to calculate calibration factors which are added into the conversion equations in the software. Although the voltage output for the total ± 1.0 mm was measured for the radial deformation sensor (MHR 25), only the linear area (± 0.625 mm) was used to calculate the calibration factor. The linear area of the sensor is where the output signal varies linearly with the core's position from the null point. Similarly the total range of the axial deformation sensors (MHR 50) is ± 2.0 mm, but the linear area is only between ± 1.25 mm.

To test the performance of the experimental system before inserting the claystone, a dummy-test was preformed on a metal cylinder. After placing the cylinder into the cell, the cell pressure was increased to 0.1 MPa. The deformation sensors were zeroed at this pressure. At 35°C the false deformation in the membrane was separated from the real deformation according to normal procedures at NGI (see Appendix). At 19 different cell pressures from 0.1 – 16.0 MPa, the mean axial and radial deformations were registered. The cell pressure (σ_{CP}) deforms the steel dummy according to;

$$\varepsilon_{steel} = \frac{\sigma_{CP}}{E_{steel}} \times (1 - 2\mu_{steel}) \tag{7.1}$$

The Young's modulus (E_{steel}) for the dummy is 215 000 MPa, while the Poisson's ratio (μ_{steel}) is 0.29. By multiplying the strain with the initial height (40 mm) and diameter (38 mm) of the dummy, the changes in height and diameter can be found, respectively ($\varepsilon_{ver}=\Delta h/h$ and $\varepsilon_{hor}=\Delta d/d$). The false deformation is then the observed deformations minus the deformation of the steel dummy (see *Appendix B*). Finally, the relationship between false deformation and cell pressure can be found by linear regression (equations *7.2* and *7.3*).

False radial deformation = 0.00032 x σ_{cp} - 0.00019 (7.2)

False axial deformation = 0.00243 x σ_{cp} + 0.00395 (7.3)

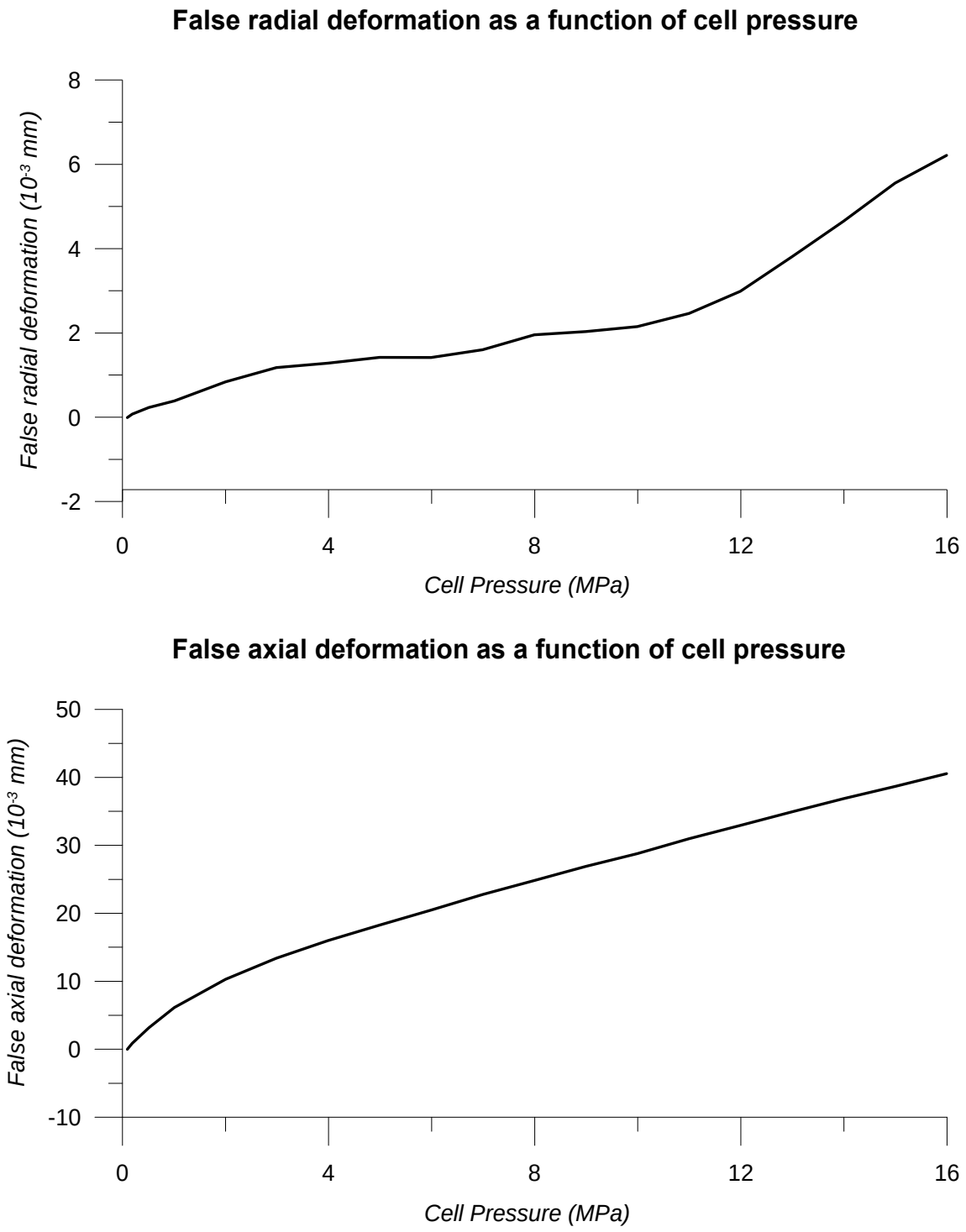

Figure 15: Plots of false radial and axial deformation versus cell pressure.

Before removing the steel cylinder, the system was tested for leakages by creating a pressure gradient of up to 10 MPa between the top and bottom of the dummy. No leakages were observed.

To saturate the shale sample with water, it was decided to use an exicator. The performance of the exicator was initially tested on approximately 50 grams of rest material. After registering the mass of the material before and after it had been in the exicator, the saturated material was lowered into a container with water placed on a scale. The density of the material could then be calculated from the mass of the displaced water. Furthermore, a calculated saturation degree of 91.7 % after saturation in the exicator demonstrated the suitability of the procedure (see *Appendix A*).

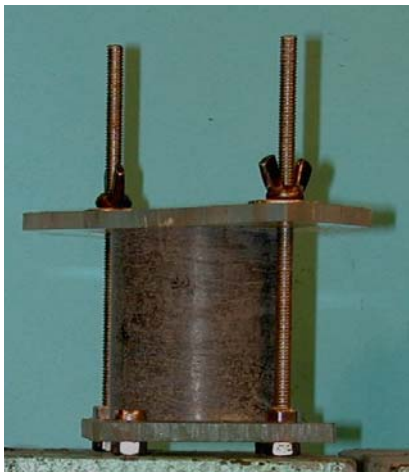

Figure 16: The claystone sample used in the experiment after saturation in exicator under small axial load.

The salt content in the water entering the plug was chosen to resemble the in situ pore water at Troll East (*[NaCl] = 57 g/l*) calculated in 1998. The accuracy of the salinity prepared was confirmed by both conductivity measurements and using a pychnometer. After vacuum had been created in the exicator, water was slowly allowed to enter until the water level in the exsiccator rose above the top of the sample. In this way the porevolume in the sample was filled with the Troll East-water. As there were concerns as to how well the claystone would stay together during vacuum treatment, it was placed under a small axial load (figure 16). After leaving the sample in the exicator for 24 hours, it was removed and the new height, weight and diameter measured. A nitrile membrane (inner diameter 38.5 mm) and four "o-rings" held the top, bottom and sample together after it had been placed inside the cell. Vacuum secured that the membrane was tightly fastened to the sample. As the claystone plug was expected to experience both axial radial shortening, the starting point of the deformation sensors were close to the end-position which would maximize the range of shortening. The cell walls were fastened to the top and bottom of the cell, and oil injected into it. The cell pressure was then immediately increased to 0.4 MPa, to prevent significant swelling. Waterfilled wires connected to a raised bottle of brine enabled water to enter the top and bottom filters when the closed off circuit under vacuum was opened.

The cell pressure was increased in steps of 0.4 MPa from 0.4 – 1.6 MPa. At each step the system was given a minimum of 20 hours to stabilize. To make sure this was enough time for stabilization, plots of the mean axial deformation against the square root of time were made (figure 17). The graphs clearly indicate that the deformation increase was significantly reduced as time passed from the pressure increase.

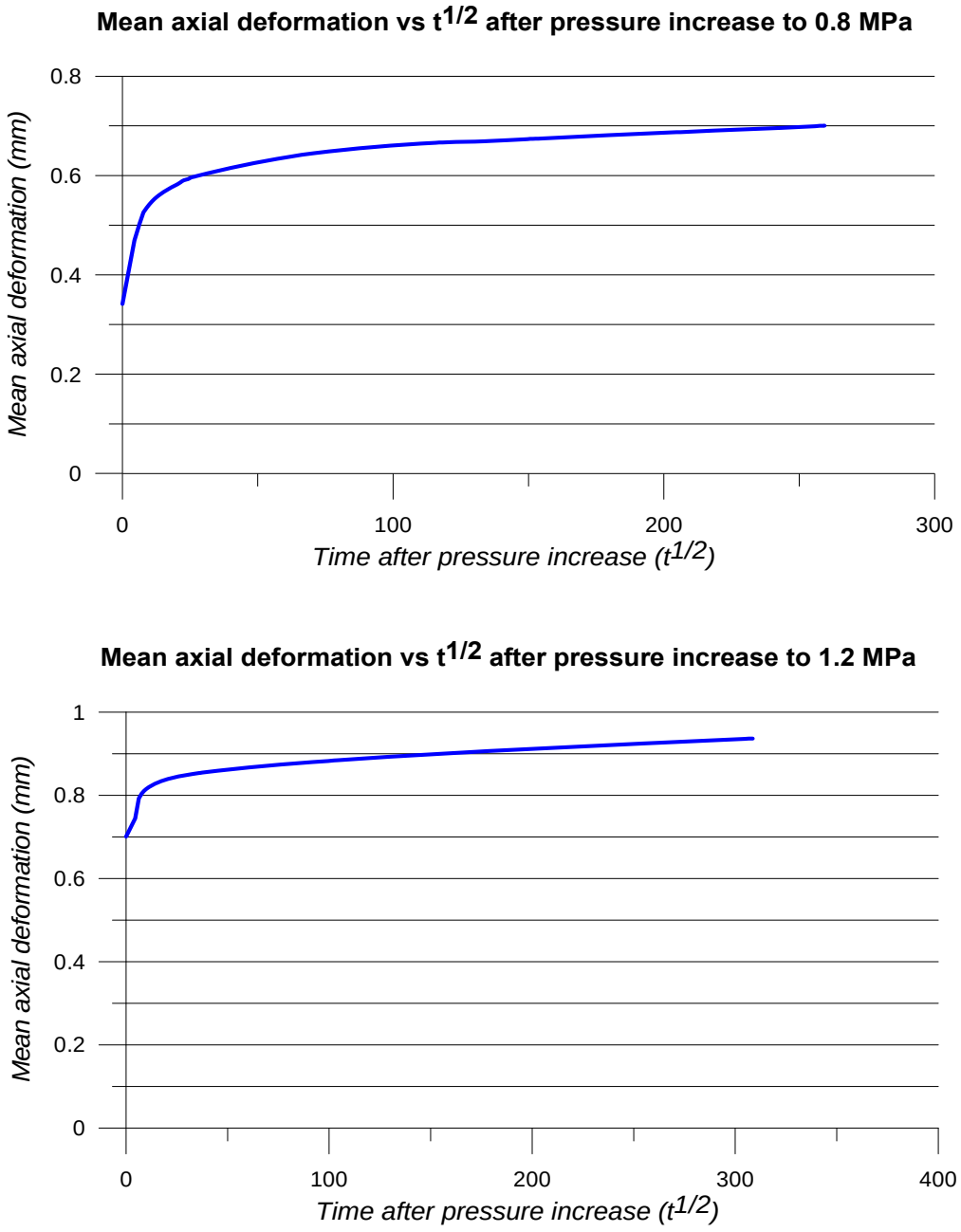

Figure 17: Mean axial deformation versus $t^{1/2}$ (s) following cell pressure increases to 0.8 and 1.2 MPa.

The process of further increasing the pressures was accomplished over two days. A relatively slow pressure ramp (9 kPa/min) applied to both the pore pressure and the cell pressure, allowed the differential pressure (*cell pressure – pore pressure*) to remain constant at 1.6 MPa. The ramp gave the pore pressure enough time to evenly distribute itself over the total length of the sample. P- and S-wave velocity measurements were taken for approximately every 0.5 MPa increase in pressure. After a pore pressure of 8.0 MPa and cell pressure 9.6 MPa had been reached, the cabinet was closed and the temperature raised to 36ºC.

When the thermistors at the top and bottom of the cell indicated that the temperature was successfully distributed throughout the cell, the cell and pore pressures were increased to 13 MPa and 8.8 MPa, respectively. Next, the pore pressure in the bottom was increased to 9.6 MPa, and the pore pressure in the top decreased to 8.0 MPa. The resulting flow from the bottom to the top of the sample was then given several days to stabilize.

After a stable flow was established through the sample, permeability tests were conducted by registering the flow in and out of the sample over 10 days. The average of these values were used together with the current height of the sample (h_i), the density of the water (γ_w), the cross-sectional area of the sample (A), the pressure gradient in the sample (Δu) and the duration of the flow (Δt) to find the conductivity coefficient k:

$$k = \frac{\Delta Q \times h_i \times \gamma_w}{A \times \Delta t \times \Delta u \times 100} (cm/s) \tag{7.4}$$

After completion of the permeability test, the pore pressure in the top and bottom were equalized at 8.8 MPa. The inner circuit extending from the sample to the two 5-way cranes could then be closed of while the pore pressure remained constant.

The mixing of CO_2 and brine was supposed to take place in the mixing chamber connected to both ISCO pumps and the CO_2 cylinder. Initially a water volume of approximately 260 cm^3 was injected into the chamber. Next the system was put under vacuum, to remove the air from the water, mixing chamber and wires. The vacuum was released after approximately 30 minutes against the CO_2 bottle, allowing CO_2 (at ~5.5 MPa) to occupy the available space in the mixing chamber and both pumps. With the two pumps and mixing chamber filled with CO_2, the CO_2 bottle was closed off. CO_2 from the pumps were pumped into the mixing

chamber, leading to an increase in pressure. Then the mixing chamber was closed again, and the pumps filled with CO_2 from the CO_2 cylinder. Another two pump volumes where then directed into the mixing chamber. This procedure was repeated until supercritical CO_2 under the desired pressure (8.8 MPa – the average pore pressure in the sample) occupied both the mixing chamber and pump A.

Next, the 5-way valve connected to pump A was pointed towards the bottom (*labeled* FLUID *phase in figure 8*) of the mixing chamber, while pump B was directed to the top (*labeled* GAS *phase in figure 8*). The CO_2 in pump A was then injected into the water using the constant pressure option. At the same time pump B was filled with CO_2 from the mixing chamber using a slow refill rate. In this way the CO_2 was bubbled through the water, ensuring that the CO_2 and water mixed. It was observed that a rather significant overpressure (~ 1.0 MPa) was needed to pump the CO_2 into the water phase, something which at the time was attributed to differences in compressibility and density between the fluids. The process was reversed and run for a total of five times.

Pump B filled with supercritical CO_2 was then held at constant pressure against the gas phase of the mixing chamber. At the same time the CO_2/brine from the fluid phase of the chamber was supposed to enter pump A under a slow volume ramp. Numerous efforts to get CO_2/brine into the pump failed, and it was decided to remove the mixing chamber from the cabinet and closely examine the problem. After releasing the pressure in the chamber, a thick discolored fluid phase was observed at the bottom of the chamber. In addition, the chamber walls were covered with solids of differing colors. These observations are believed to come from dissolution of the inner walls of the mixing chamber. In addition, indications of dissolution could also be seen on the stainless steel wire reaching down to the water phase in the mixing chamber.

As the reactivity of the CO_2/brine mixture was considered too high for the aluminum-covered scuba bottle, a cylindrical titanium container was inserted instead. A hollow polypropylene cylinder placed inside the titanium container prohibited direct contact between the titanium walls and the brine/CO_2 mixture. The bottom of the cylinder was sealed off by a lid with two o-rings. The 316 steel wire originally extending into the container was replaced with a PEEK tube.

Even though the initial mixing of water and CO_2 in the titanium cylinder worked satisfactory, it was decided that the risk of filling the expensive ISCO pumps with the very reactive CO_2/brine mixture was too high. Instead supercritical CO_2 was injected directly into the sample and the breakthrough pressure was measured. As the experiment will continue after the registration of breakthrough pressure, mixing of CO2 and brine is expected to take place within the sample. The effects of CO2/brine interaction with the sample can therefore be evaluated after some time (unfortunately, *after* the completion of this thesis).

Over the period the sample had been closed off, its pore pressure had decreased to approximately 7.5 MPa. It was therefore decided to start the breakthrough test by imposing an equal supercritical CO_2 pressure of 7.5 MPa in the top and bottom of the sample. After the system had reached a stabile condition, the pressure was increased in the bottom (0.2 MPa steps). Before moving on to the next pressure increase, plots of the flow rate versus time indicated stabile, non-breakthrough conditions. This was repeated until flow in and out of the sample was observed.

7.2 Batch reactor at UiO

At the University of Oslo approximately 1 gram of powdered shale was reacted with solutions of different pH for 48 hours at 200°C. The solutions were constantly stirred at moderate velocity. The various pH-solutions were prepared from HCl, NH_4Cl and NH_4OH. Upon completion of each test, the solutions were rapidly cooled by lowering the container into a bucket of cold water. This was done to prevent precipitation of dissolved minerals. After the temperature had been lowered to around 50°C, the grains and solutions were separated by filtering. The solutions were placed in a refrigerator, while the solid particles were dried at a moderate temperature.

The solutions were analyzed for different ions using ion chromatography (Cl and SO4), spectrophotometry (Si) and atomic absorption spectroscopy (Na, K, Mg, Ca, Al). Ion chromatography is based on the retention of analytes by columbic interaction with a stationary charged phase. After absorption in a chromatography column, an ion extraction liquid passes through the column. The absorbed ions then separate from the column and the retention times determine the ionic concentrations. In atomic absorption spectroscopy the analyte atoms should be in the gas phase. This is realized through vaporization and desolvation using a high

temperature flame. Next, light from an element-specific cathode lamp passes through the flame. The amount of light absorbed by the analyte is directly related to the amount present of that element. In spectrophotometry a spectrophotometer can measure the concentration of ions as a function of the color (wavelength of light) in the solution after certain chemicals have been added.

The alkalinities of the different solutions, or buffering capacities, were evaluated using Gran titration. In this method known amounts of 0.001 M HCl were added to the solution while registering the pH. The principle behind Gran titration is that the H+ levels will increase linearly with the amount of H^+ added at the point where all HCO_3^- has been converted to H_2CO_3. The Gran titration essentially linearizes the titration curve by applying the following expression;

$$F_1 = (V + V_0) \times 10^{-pH} \tag{7.5}$$

where V_0 is the initial sample volume, V is the volume acid added and pH is the negative logarithm of the H^+-concentration at that time. When F_1 is plotted against V, the equivalence point V_e was selected where the Gran function is 0.001. The volume acid needed to reach the equivalence point is used together with the initial volume of the sample (V_s) and the concentration of acid (C_{acid}) to find the alkalinity;

$$Alk(^{meq}/_{l}) = \frac{V_e \times C_{acid} \times 1000}{V_s} \tag{7.6}$$

Based on the solution analysis, four samples were chosen for SEM inspection. In addition, unreacted crushed material was examined for comparison.

8 Results

8.1 Flow through cell at NGI

8.1.1 Saturation of sample

The weight, height and diameter of the claystone plug used in the flow through experiment was measured prior to and after water saturation in the exicator (table 4). Swelling smectites caused the volume to increase by almost 4.7 %.

Table 4: Weight, height and diameter of the Draupne claystone before and after saturation in the exicator,

	Before exicator	**After exicator**
Weight of sample (g)	98.26	102.59
Diameter (mm)	38.1	38.6
Heigth (mm)	40.1	40.9

8.1.2 Consolidation

The path of cell and pore pressure increase followed prior to the permeability test can be divided in three main events in terms of deformation monitoring;

- First the cell pressure was increased while the pore pressure was kept constant (*i.e. differential pressure increased.*)
- Next the pore and cell pressures were increased simultaneously (*i.e. differential pressure kept constant.*)
- Finally the cell pressure was increased to prevent leakage between sample and membrane, while pore pressure was kept constant (*i.e. differential pressure increased.*)

Deformation of the sample during the different pressure events is shown in figure 18 – 20 (note that strain axes are not to scale).

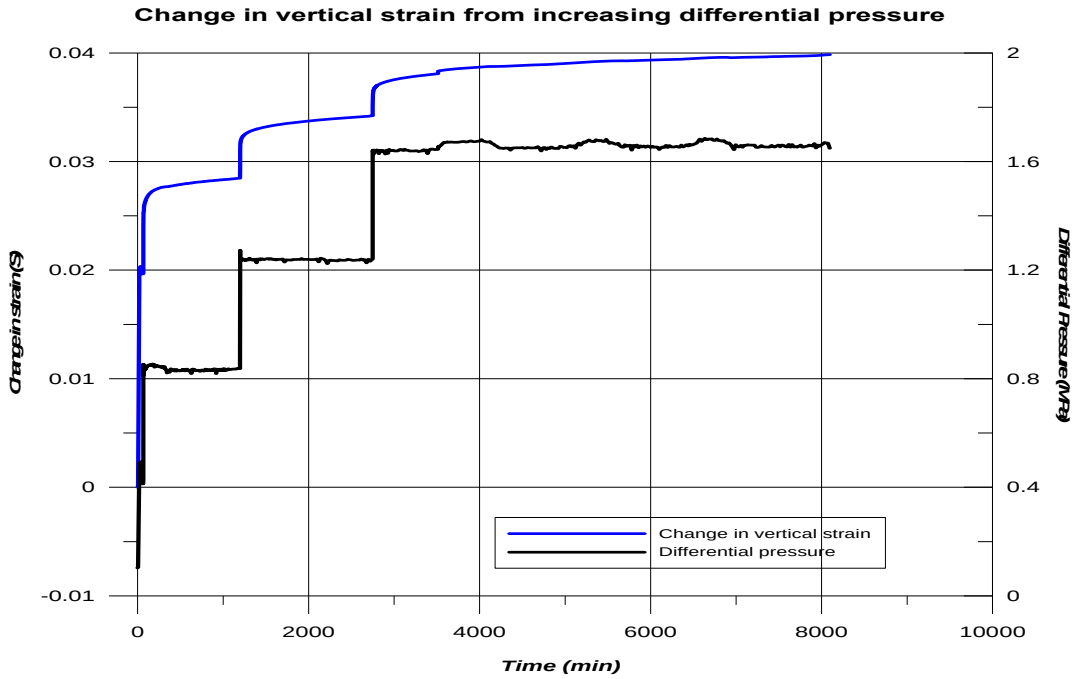

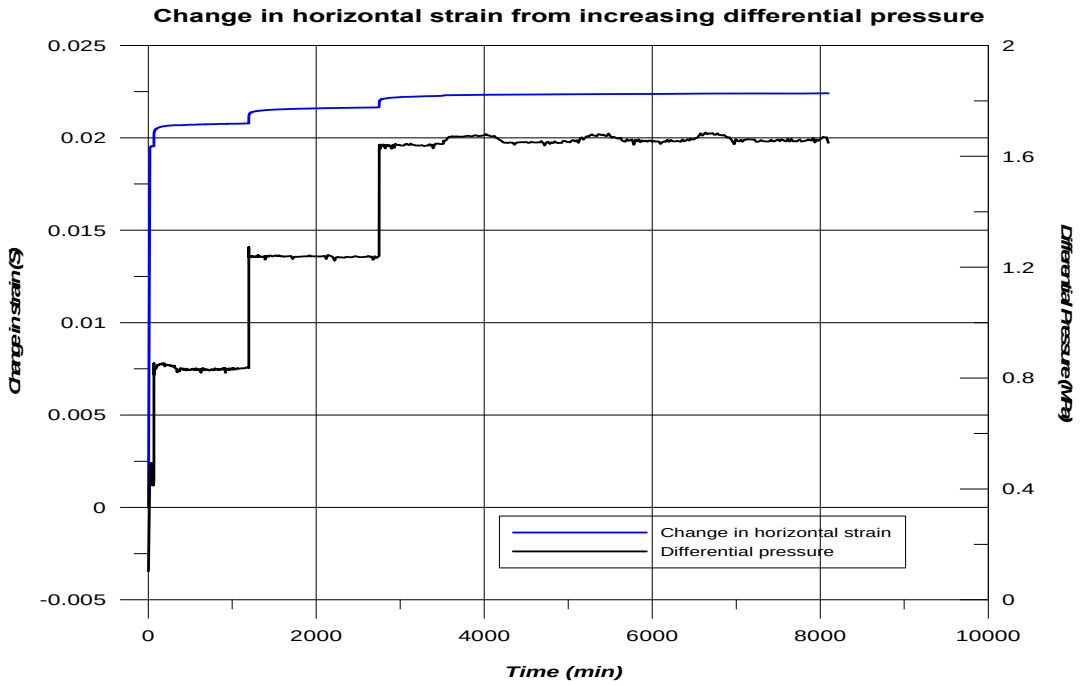

Figure 18: (Above) Change in vertical strain under increasing differential pressure fro 0 – 1.6 MPa. Positive strain indicates decrease in sample size. (Below) Change in horizontal strain for the same period.

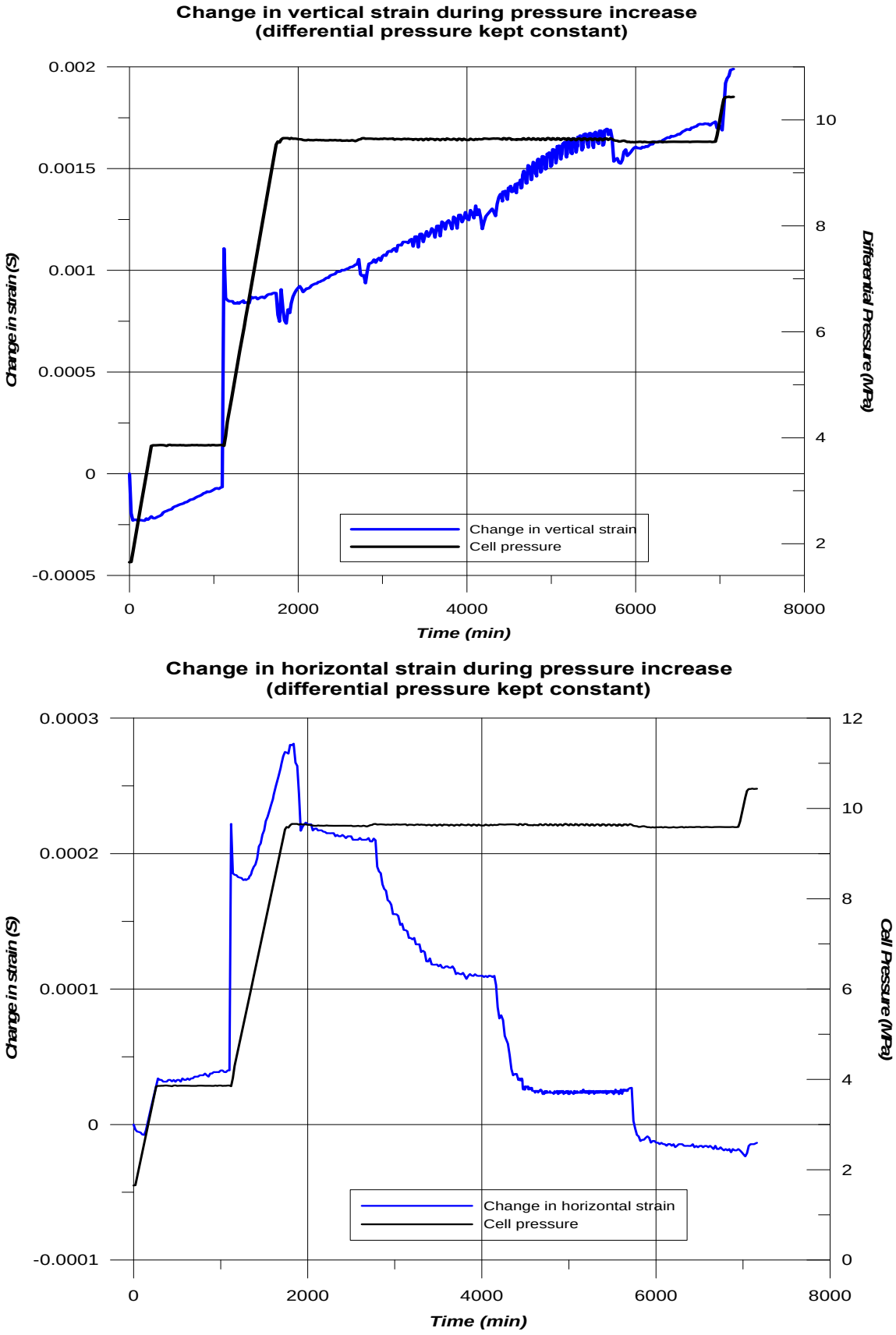

Figure 19: (Above) Change in vertical strain under pore and cell pressure increase (constant differential pressure). Positive strain indicates decrease in sample size. (Below) Change in horizontal strain for the same period.

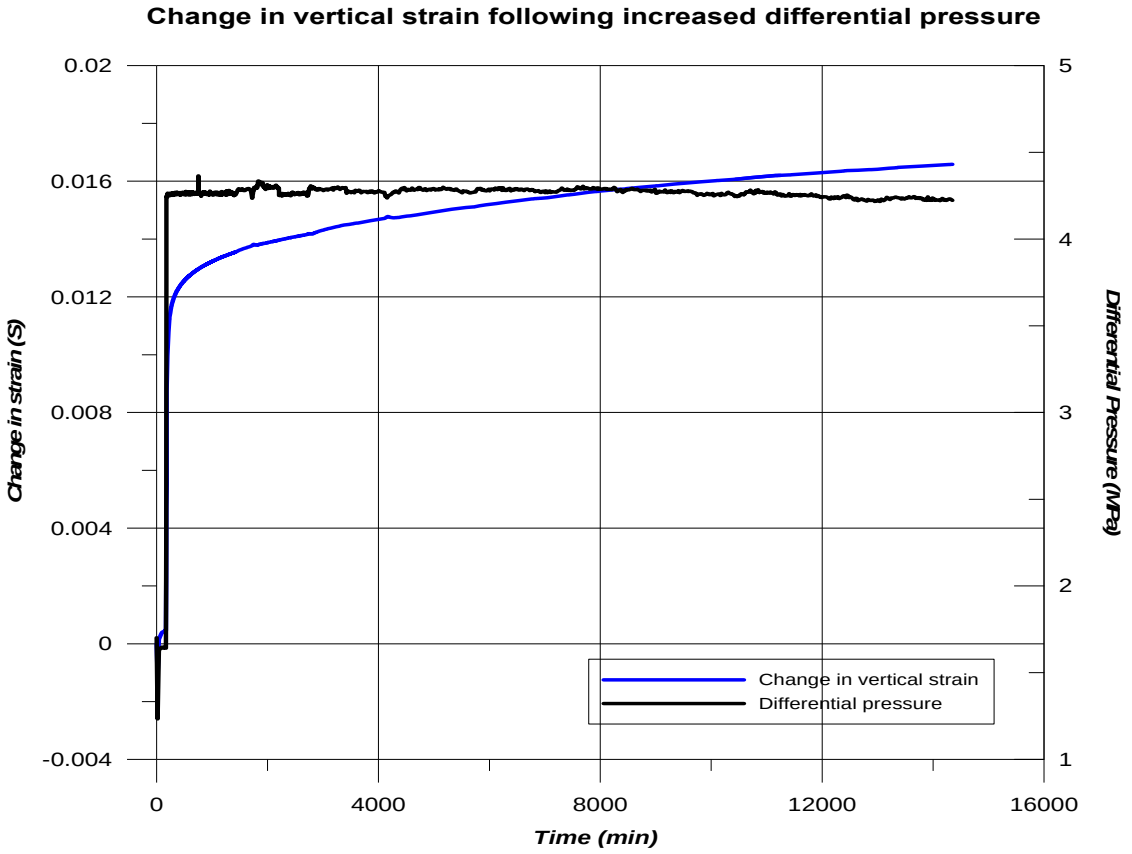

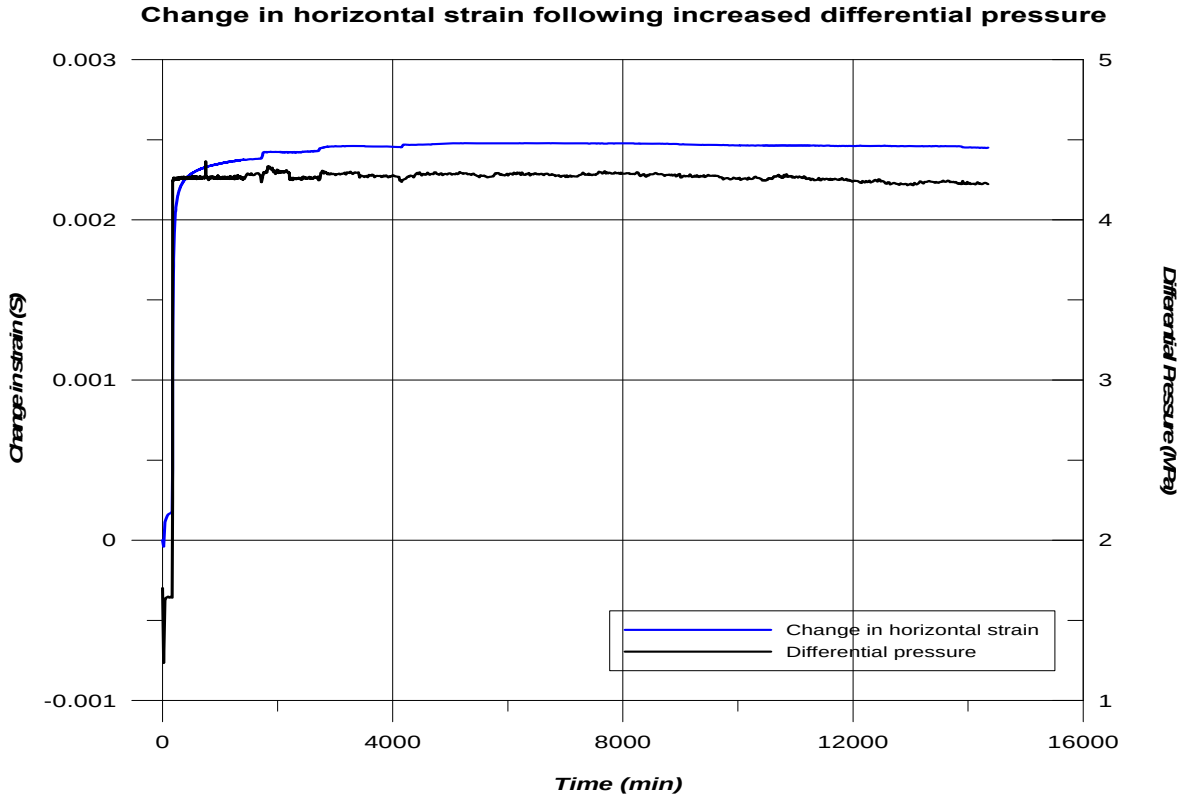

Figure 20: (Above) Change in vertical strain following increase in differential pressure from 1.6 MPa to 4.2 MPa. Positive strain indicates decrease in sample size. (Below) Change in horizontal strain for the same period.

Deformation of the sample following initial differential pressure increase to 1.6 MPa is plotted in figure 18. As already mentioned in chapter 7, the cell pressure was increased in steps of 0.4 MPa. Approximately 50 percent of the total vertical change in strain caused by increasing differential pressure was induced in the first pressure step. Over the next steps, the resulting strain changes became progressively smaller. In the horizontal direction almost 90 % of the total change in strain came from the first pressure increase. The overall change in vertical strain for this period was almost twice that in the horizontal direction.

Figure 19 shows how the vertical and horizontal strains developed during cell pressure increase from 1.6 – 10.6 MPa. During this step the pore pressure was increased at the same rate as the cell pressure, maintaining a constant differential pressure. As deformation in the sample is mostly related to changes in differential pressure, the simultaneous increase of pore and cell pressure gave little deformation. At the end of this pressure event, the pore pressure was 8.8 MPa and the cell pressure 10.6 MPa.

To make sure there were no potential leakage routes between the membrane and the sample, the differential pressure was increased by raising the cell pressure to 13 MPa, while keeping the pore pressure constant at 8.8 MPa. The increase in differential pressure from 1.6 MPa to 4.2 MPa resulted in $\Delta\varepsilon_v \approx 12.5$ mS and $\Delta\varepsilon_h \approx 2.25$ mS (figure 20). With time the changes in both axial and radial deformation approached zero.

8.1.3 Permeability test

At the beginning of the permeability test the initial height and diameter of the sample had decreased by approximately 2.3 and 0.26 mm, respectively. To measure the permeability, flow in and out of the sample was registered for ten days. A total of 12 permeability coefficients (k) were calculated for time intervals ranging from 160 – 1420 minutes (see *Appendix C*). The relatively large variation in permeability coefficients (8.15 – 5.78 x 10-11 cm s-1) can to some extent be explained by temperature variations within the cabinet. Figure 21 shows the flow rate (cm^3 min-1) in and out of the sample plotted against time. Virtually all large peaks and troughs in flow rate can be assigned to an increase or decrease in cabinet/cell temperature. Furthermore, the permeability coefficients seem to approach a more steady state with time. Based on figure 21 and the measured temperatures, the most stable conditions were considered to be in the time interval between 4 200 and 14 100 minutes after start of permeability measurements. The corresponding permeability coefficient is 6.26×10^{-11} cm s^{-1}.

This permeability coefficient is approximately 45 percent higher than the one obtained on a adjacent plug in 1998 (4.32 $\times 10^{-11}$ cm s^{-1}). The test ten years ago was performed with a significantly lower differential pressure (1.6 MPa), something which may explain the deviation. Some of the difference may also be attributed to spatial variations in the seal peel examined and micro fractures from drying of the sample.

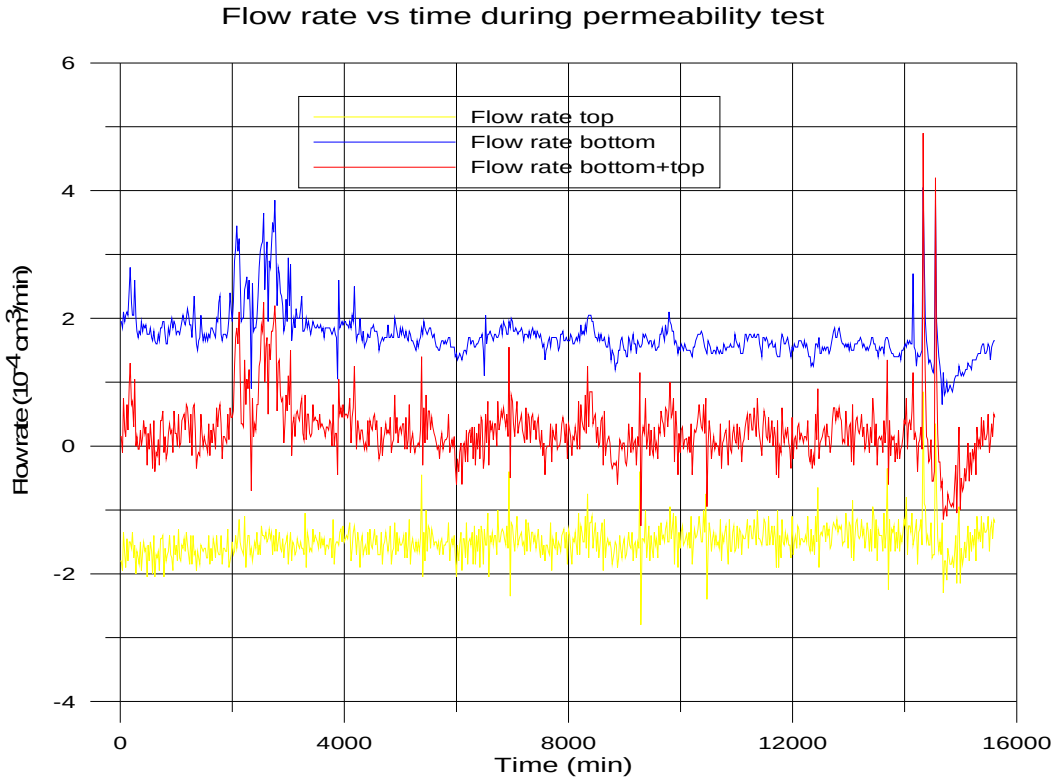

Figure 21: Flow in and out of the sample during permeability test. Positive flow rate means that brine is leaving the pump and negative means that brine enters.

The changes in vertical and horizontal strain during the permeability test are shown in figure 22. In the axial direction the sample experienced minor shortening (5 x 10^{-2} mm), while the diameter remained virtually unchanged.

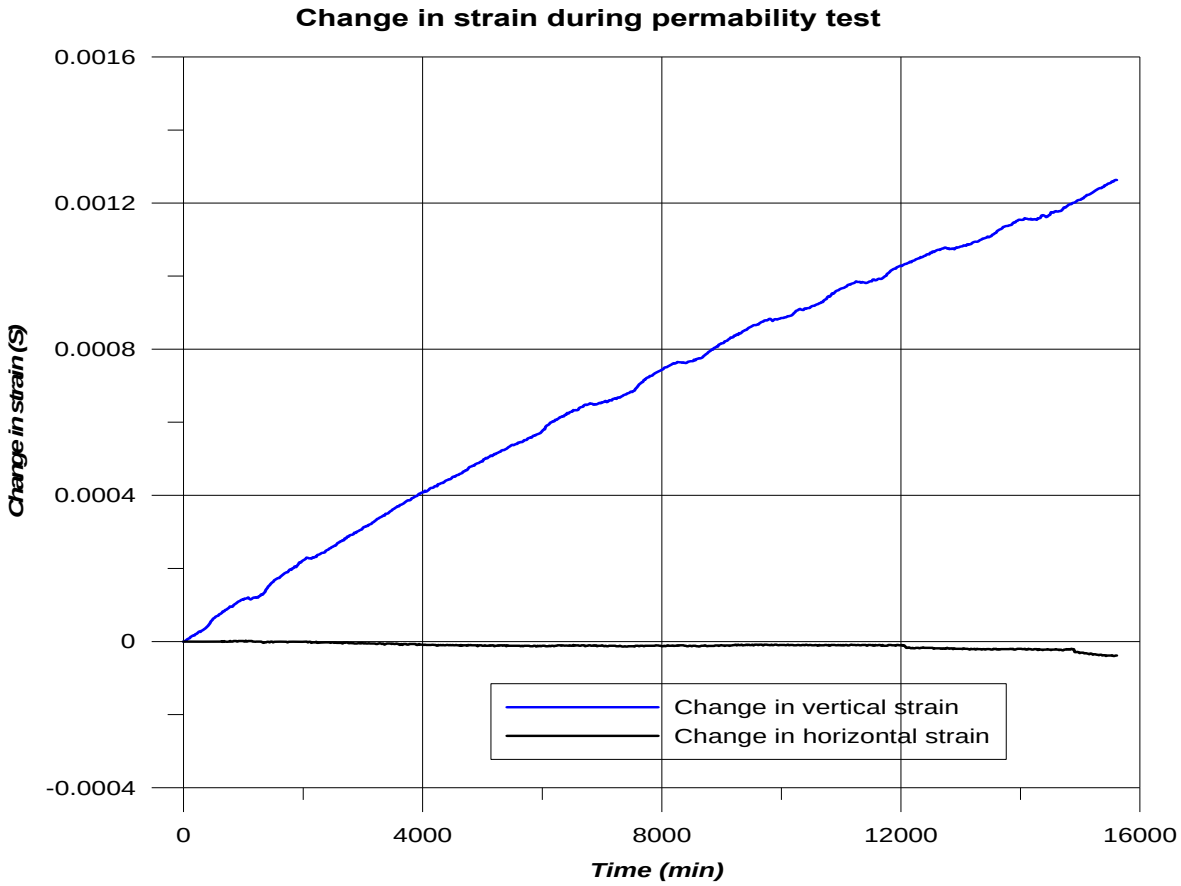

Figure 22: Change in vertical and horizontal strain (in mS) during permeability test. Positive strain indicates decrease in sample size.

As the two syringe pumps controlling the pore pressure were needed to mix CO_2 and water, the sample had to stay isolated for some time. Unfortunately, problems arising prolonged this time period substantially, leaving the pumps disconnected for approximately 50 days. During this time, the pore pressure in the sample dropped by 2.5 MPa. The deformation in the sample during this period is given in figure 23. Whereas the sample only experienced negligible deformation in the radial direction, the length of the sample decreased by approximately 0.2 mm.

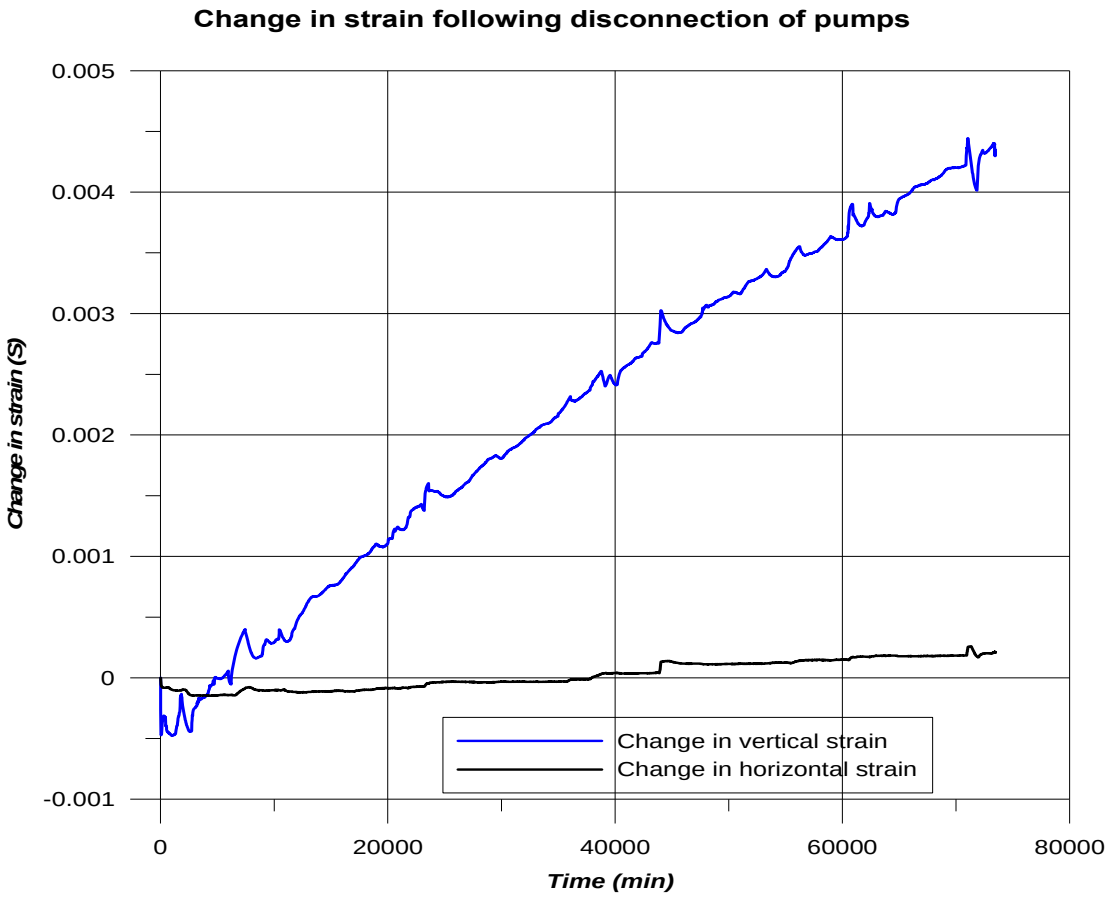

Figure 23: Change in vertical and horizontal strain (in mS) following disconnection of pumps. Positive strain indicates decrease in sample size.

8.1.4 Breakthrough pressure test

In the breakthrough experiment, the pressure in pump A (filled with CO_2), connected to the bottom of the sample, was increased in steps from 0.1-0.5 MPa, starting at 7.5 MPa. At the same time the pressure connected to the top (pump B, with CO_2) was kept at 7.5 MPa. The CO_2 breakthrough pressure was to be identified as the smallest differential pressure between pump A and B capable of transporting fluid from one pump to the other. The flow rates at various pressure gradient steps are plotted in figure 24.

The flow out of pump A generally approached zero within a few hours after each pressure increase. At the same time, a relatively irregular flow was observed in the pump connected to the top of the sample. As the conditions in pump B were very close to the critical point of CO_2, the compressibility was extremely high. Consequently, small pressure changes caused

by temperature variations in the cabinet and cell significantly altered the volume of CO_2 leaving or entering pump B. The compressibility increase close to the critical point can also be seen from the flow rates to the bottom of the sample. As the pressure increased in the bottom of the sample, the test conditions moved away from the critical point and progressively less and less CO_2 was needed to reach the desired pressures in pump A.

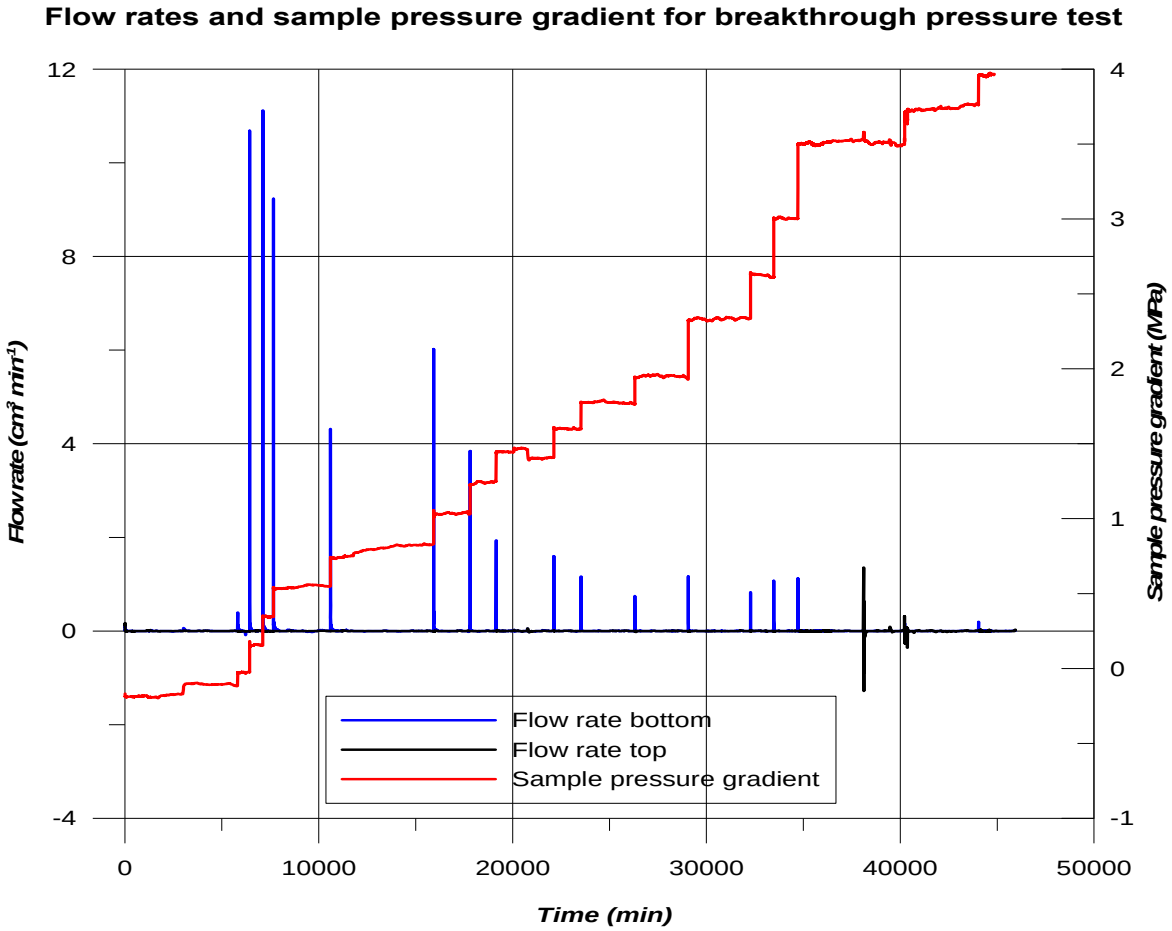

Figure 24: Flow rates in pump A and B associated with the different sample pressure gradient steps. Positive flow rate means that CO_2 leaves the pump.

Because of the compressibility, identification of breakthrough pressure meant that potential flow through the sample somehow had to be separated from the volume changes caused by temperature variations. Naturally the temperature variations in the cabinet were larger and more abrupt than in the cell. As the volume changes in pump B were a factor of the temperature in both cabinet and cell, neither of them showed a good correlation with the flow rate. It was decided to isolate time periods where the temperature stayed fairly constant (± 0.05 ºC) for more than 100 minutes for each pressure increment step. The pump volumes and

flow rates within such time intervals are shown in figure 25, 26 and 27 for sample pressure gradients ΔP 3.0, 3.5 and 3.9 MPa, respectively.

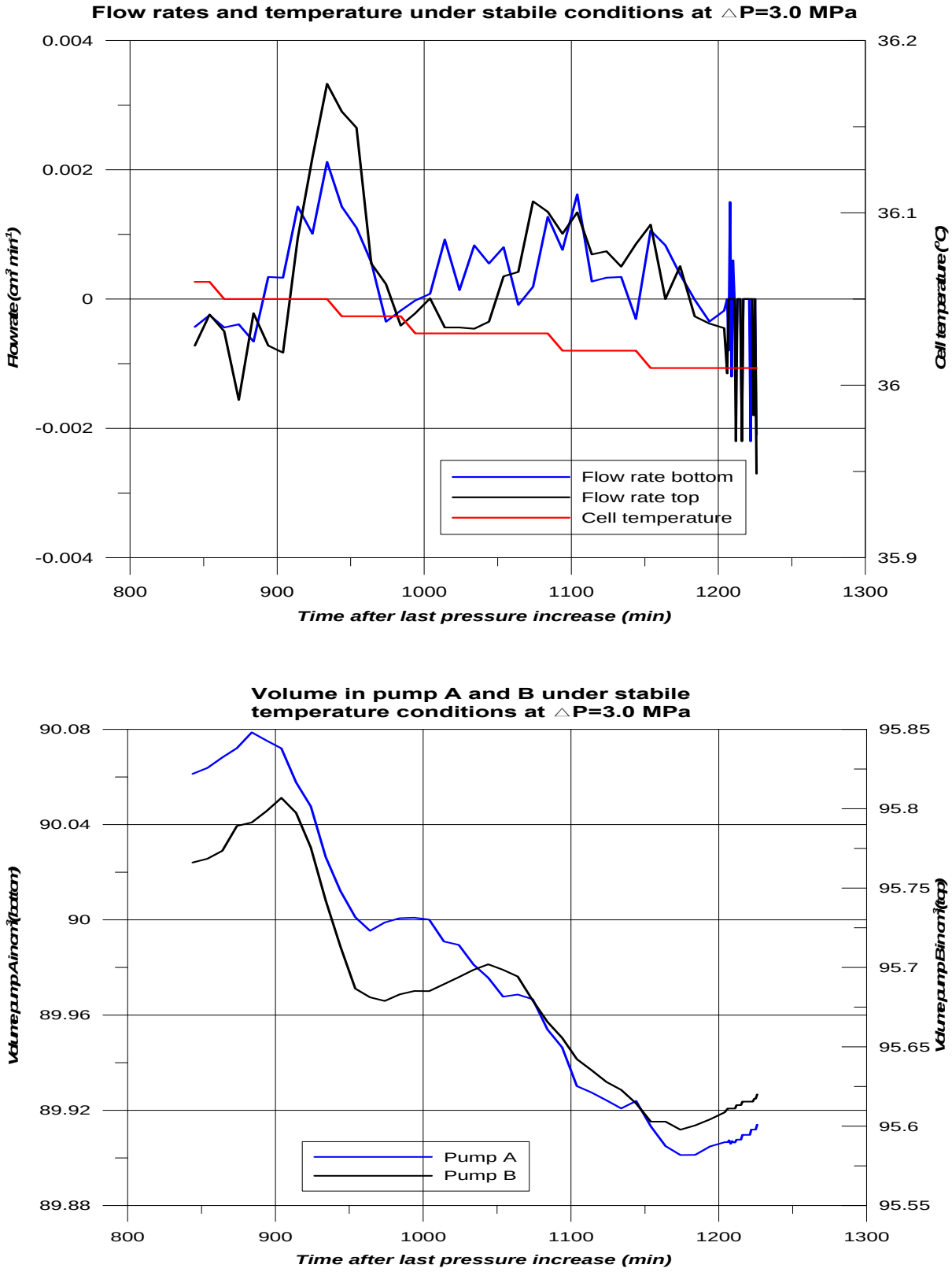

Figure 25: (Above) Flow rates for both pump and cell temperature at ΔP = 3.0 MPa. Positive flow rate means that CO_2 leaves the pump, (Below) CO_2 volume in pumps for the same time period.

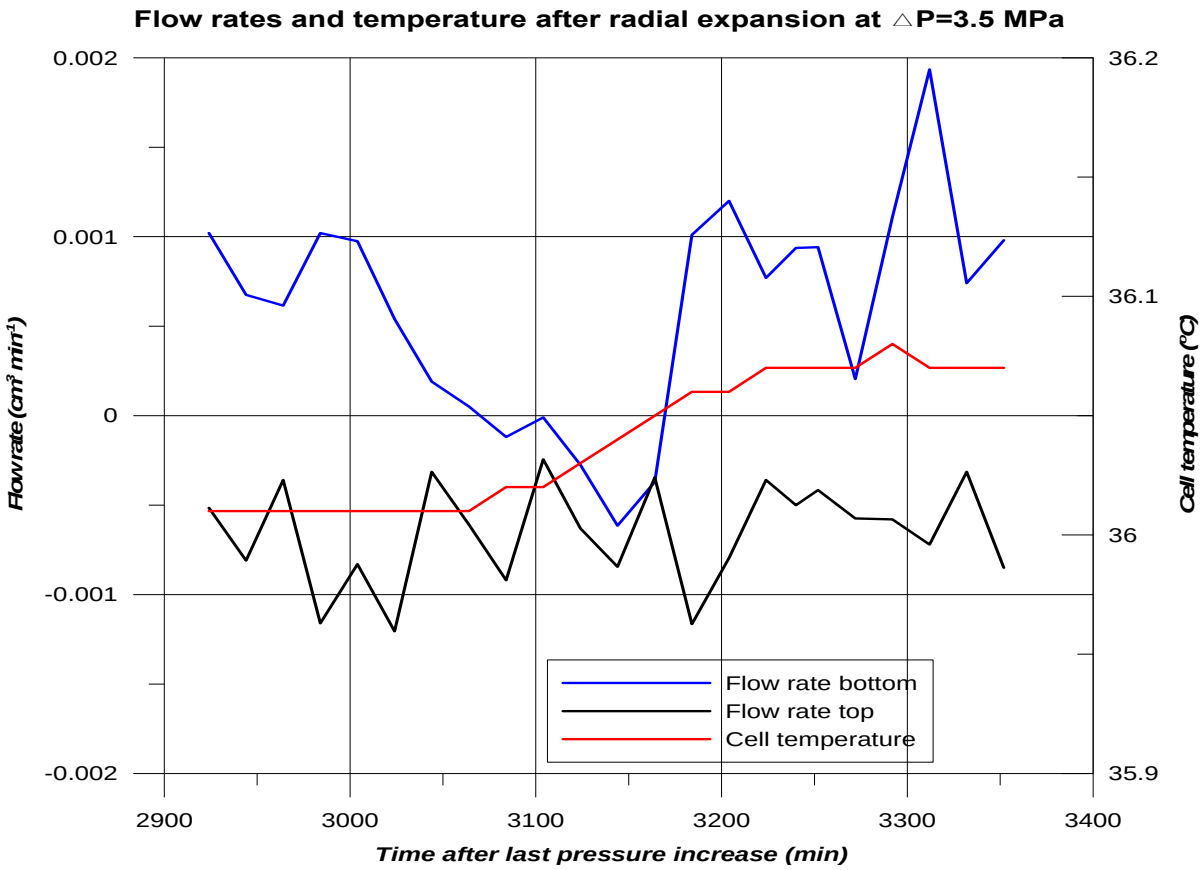

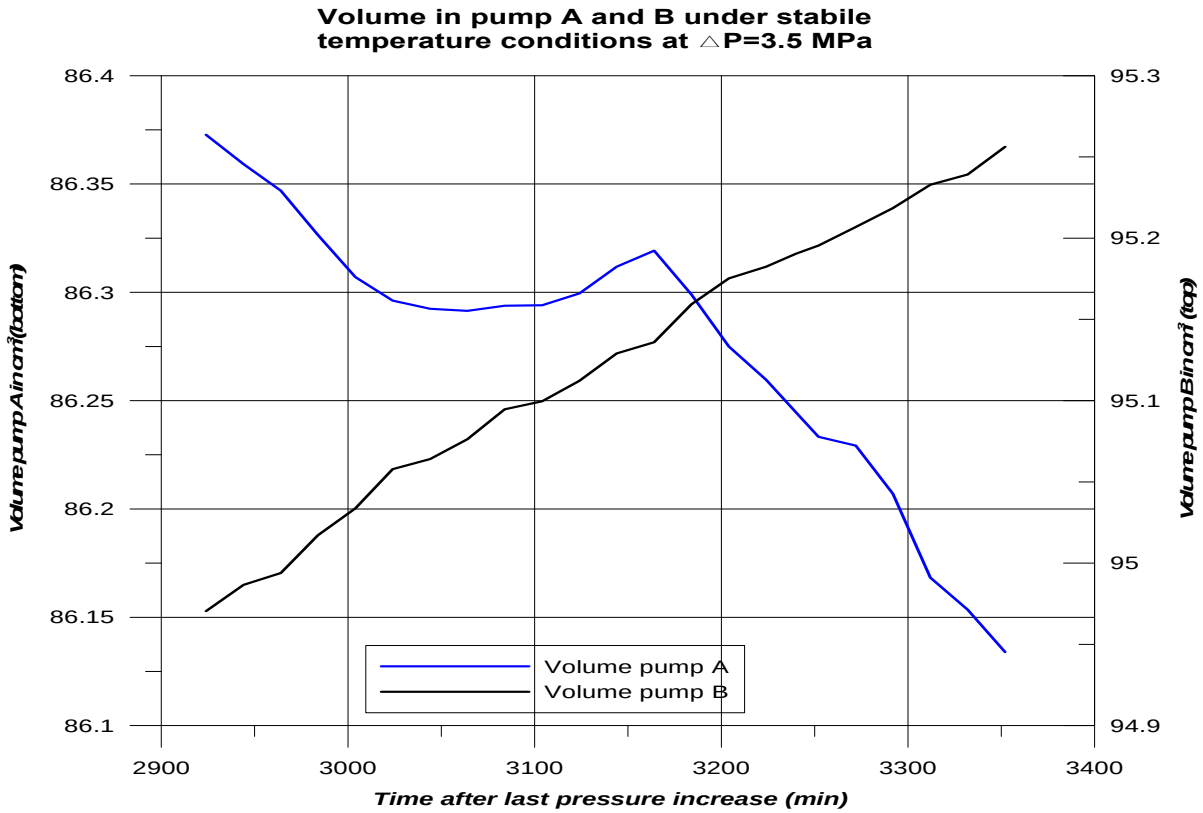

Figure 26: (Above) Flow rates for both pump and cell temperature at ΔP = 3.5 MPa. Positive flow rate means that CO_2 leaves the pump, (Below) CO_2 volume in pumps for the same time period.

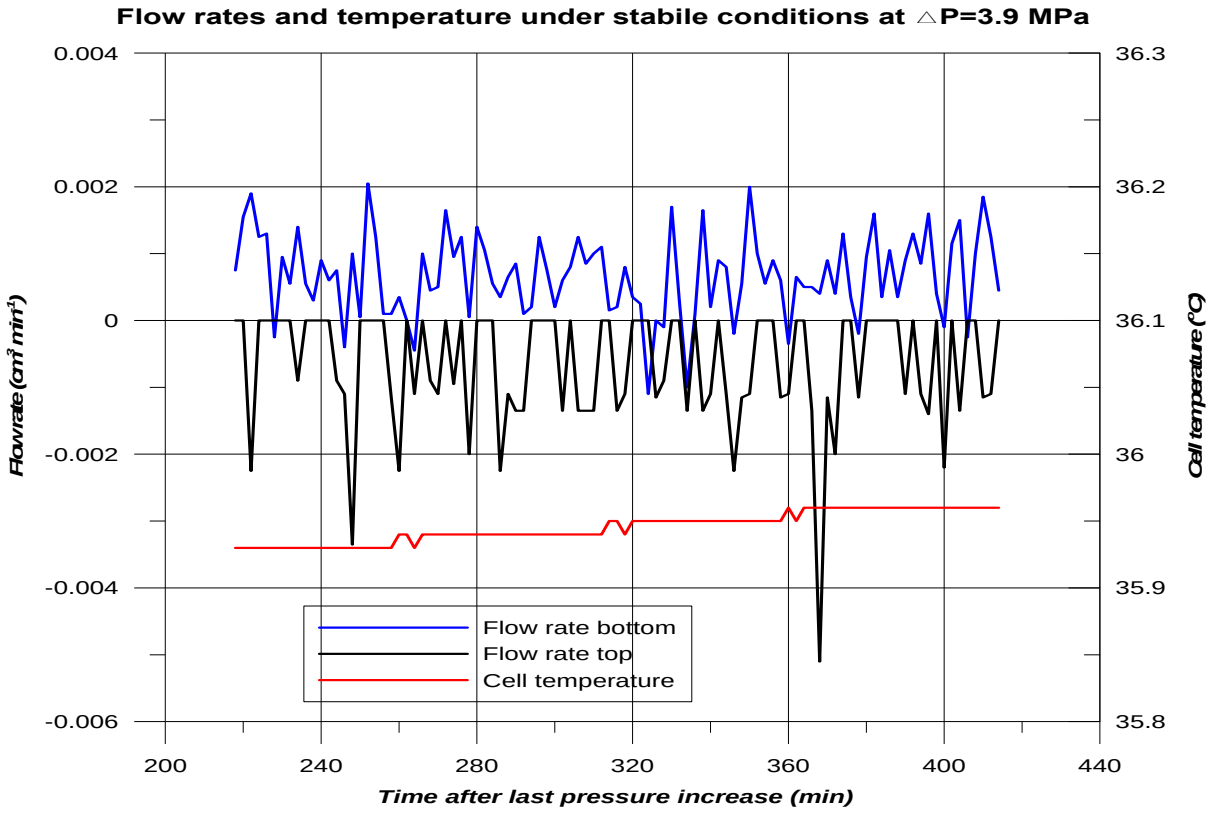

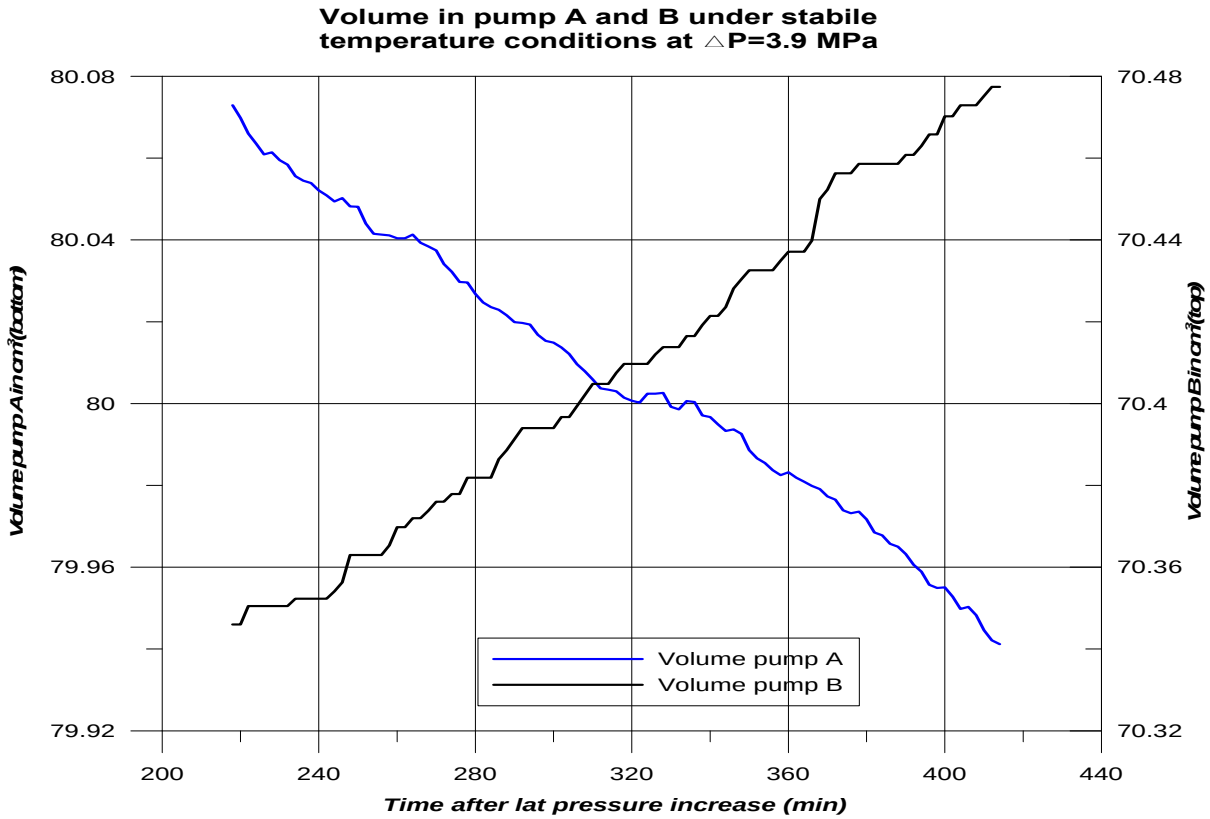

Figure 27: (Above) Flow rates for both pump and cell temperature at ΔP = 3.9 MPa. Positive flow rate means that CO_2 leaves the pump, (Below) CO_2 volume in pumps for the same time period.

At ΔP = 3.0 MPa the volumes in both pumps are decreasing with time (figure 25). The volume decrease in pump B connected to the top of the cell is actually larger than for the pump connected to the bottom. These volume changes are probably solely caused by temperature variations. The flow rates in pump A and B show a similar trend in that they are increasing/decreasing at approximately the same time.

Increasing ΔP to 3.5 MPa, leads to a somewhat different volume and flow rate pattern (figure 26). Whereas CO_2 leaves pump A, the volume in pump B increases. The flow rates in pump A are generally above zero, while B shows negative flow rates.

The trend vaguely seen moving from ΔP = 3.0 to ΔP = 3.5 MPa, becomes clearer when considering ΔP = 3.9 MPa (figure 27). At this sample pressure gradient almost identical amounts of CO_2 are leaving pump B and entering pump A. The flow rates appear evenly distributed above and below zero. There is a general impression of flow from pump A to pump B, *i.e.* flow from the bottom to the top of the sample.

Plots of deformation following pressure increase display a very peculiar behavior (figure 28). Generally the pressure increments were followed by a minor axial shortening, while the diameter remained unaltered. At ΔP=3.5 MPa, the sample experienced an abrupt change in radial deformation starting approximately 45 hours after the pressure increase. While the sample expanded slightly in the axial direction in a manner similar to that of previous pressure increments, the radial expansion was very different from the earlier behavior. Approximately 15 hours after the onset of the radial expansion, the fluid sampler device, which had been removed from the system for some time, was inserted between pump B and the top of the sample. During this operation the cabinet was opened, and pump B disconnected from the sample. With temperature decreasing, the pressure in the top of the sample decreased and ΔP increased somewhat. However, the trends in radial expansion before and after insertion of the fluid sample tube were identical, indicating that the pressure drop in the top of the sample did not affect the sample (figure 29). No specific change in neither temperature nor pressure was seen prior to the onset of the radial expansion.

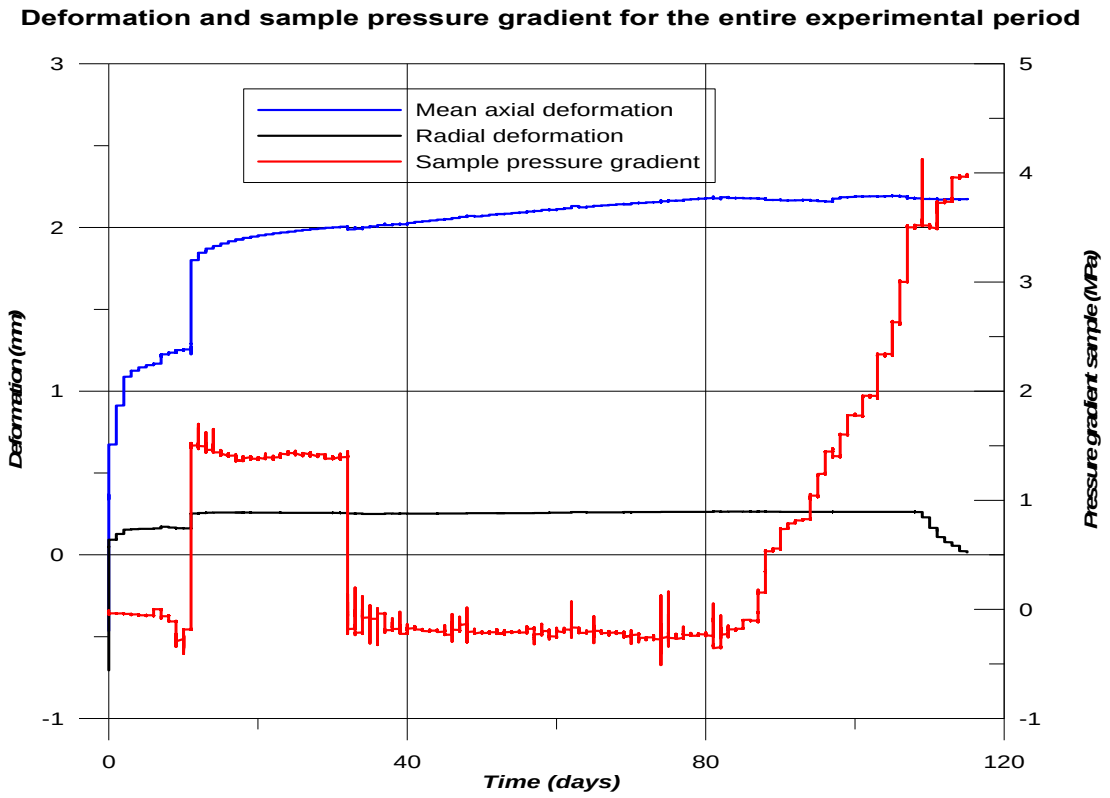

Figure 28: Plot of vertical and horizontal deformation (in mm) and sample pressure gradient (MPa) for the entire experimental period.

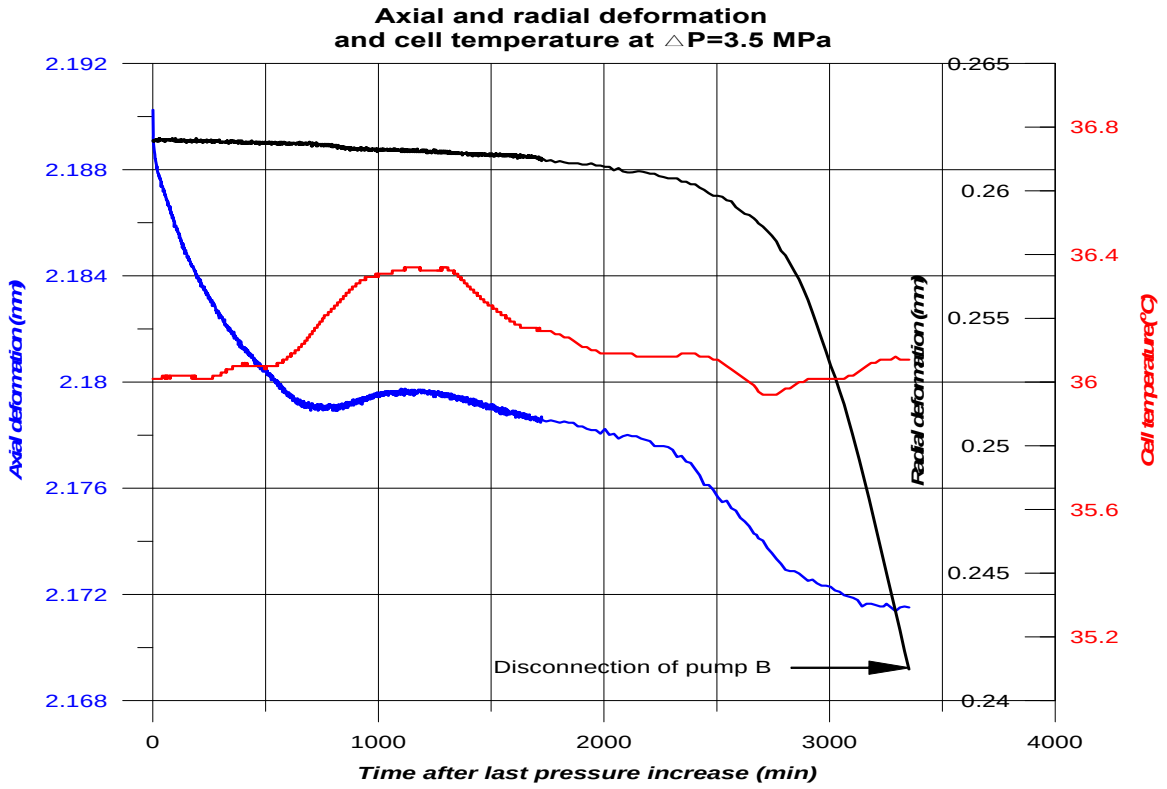

Figure 29: Axial and radial deformation (mm) and cell temperature at the onset of radial expansion. The trend deformation trend started in figure 29 continued throughout the rest of the experiment.

It was also searched for evidence of CO_2 inside the claystone from the P-wave velocity measurements (see *Appendix G*). However, the only changes in V_p discovered during the experiment were associated with increasing differential pressure. Increasing the cell pressure from 10.4 to 13.0 MPa while keeping the pore pressure at 8.8 MPa, increased the P-wave velocity by approximately 6 %. As there were differences in defining the first arrival of S-waves, they are not included in the thesis.

8.2 Batch reactor at UiO

The initial and final pH, alkalinity and ion concentrations for the 10 solutions are listed in *Appenix F*. The levels of all cations except aluminum were usually decreasing with increasing initial pH. Generally the solutions had relatively similar calcium and potassium levels, while the magnesium levels were somewhat smaller. Silicon showed a slight decrease with pH, but overall the levels stayed fairly constant. It should be mentioned that there were some problems with the spectrophotometer used for silicon concentrations. The apparatus was not able to reproduce accurately the values of certified standards. The concentrations listed in *Appendix F*, are adjusted according to the deviations experienced on these standard solutions. Aluminum concentrations were minor, but increasing with pH.

The concentrations of Mg, Ca and K were plotted against the corresponding silicon content for the different solutions (see figure 30). The solution with the lowest pH appears to the right, while progressively less acidic solutions follow to the left. Linear trend lines are included in the plot, even though the deviation from linear trend was significant. The amounts of calcium and magnesium in the solution showed a stronger correlation with initial pH than silicon did. This indicates carbonate dissolution at low pH. Potassium roughly displayed a 1:1 relationship with silicon.

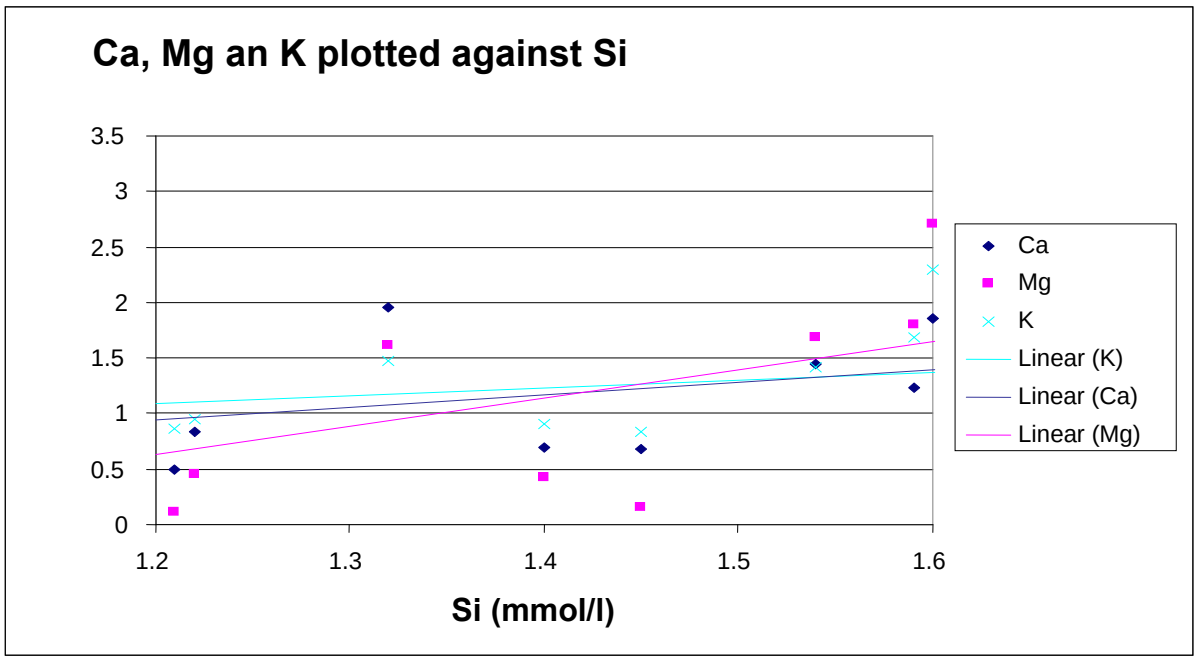

Figure 30: Ca, Mg and K levels (mmol/l) in the different solutions on the vertical axis plotted against Si. The lowest pHs has the highest cation concentrations and are found to the right in the plot.

The saturation indexes (SI) for calcite and dolomite in the different solutions were calculated using PHREEQC. PHREEQC is a tool for simulating geochemical reactions and transport processes in natural and polluted waters. Figure 31 shows the saturation indexes plotted against final pH. Negative SI indicates undersaturation with respect to the mineral, favoring dissolution. At saturation index of zero the solution is saturated, while a positive SI suggests supersaturation and precipitation. Generally, the low pH solutions are undersaturated with respect to both dolomite and calcite. In the case of calcite, solutions with pH > 6.5 become saturated. Even though the high pH solutions show supersaturation, the SI is relatively close to zero, making precipitation questionable. For dolomite, the solutions never reach saturation.

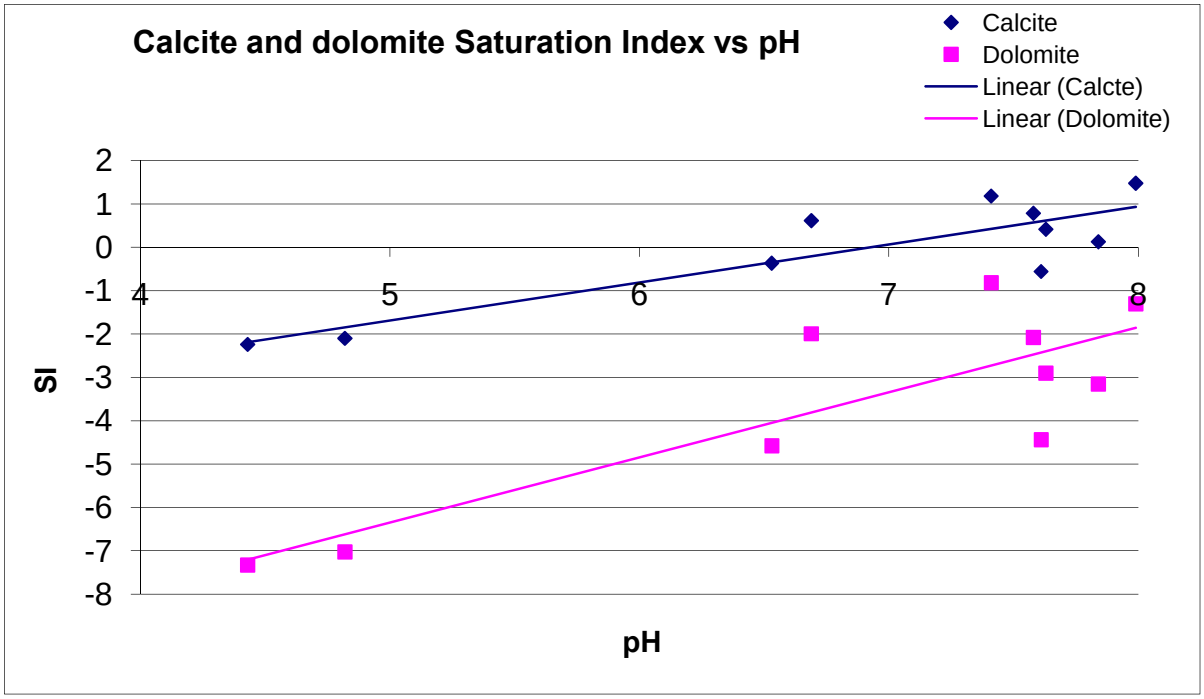

Figure 31: Plot of calcite and dolomite saturation index vs pH of solution.

Considering dissolution of all the dolomite ($CaMg(CO_3)_2$) initially present (see Appendix D), it would correspond to 1.61 x 10^{-4} mol. The number of moles of magnesium in the most acidic solution (~100 cm^3) was approximately 2.7 x 10^{-4} moles. This would indicate that even with dissolution of all dolomite, some of the magnesium originates from other sources. For calcium, maximum dissolution of dolomite explains the levels encountered. It should be mentioned that the weight percents as determined from XRD contain a significant uncertainty, meaning that dolomite dissolution could be responsible for a larger part of the magnesium in solution. Even so, potential sources for the extra magnesium could be dissolution of the magnesium rich chlorite mineral clinochlore ($(Mg_5Al)(AlSi_3)O_{10}(OH)_8$), or maybe even illite ($(K,H_3O)(Al,Mg,Fe)_2(Si,Al)_4O_{10}[(OH)_2,H_2O]$).

Sediments exposed to initial pH of 2, 4, 8 and 10 were compared to unreacted sediments in the Scanning Electron Microscope. Identification of significant differences between the samples proved very challenging. In the least acidic solution it was possible to see fibrous illite appearing between larger clay mineral grains (see figure 32). From the shape it was difficult to state if the fibers originated from dissolution or precipitation, but considering the basic environment they could very well be secondary precipitates.

The only carbonate mineral identified was calcite from sample 8 (with final pH 6.53). According to the saturation index for calcite, solution 8 was undersaturated. Together with the shape of the mineral, this indicates that the calcite observed was a primary clastic phase (figure 33).

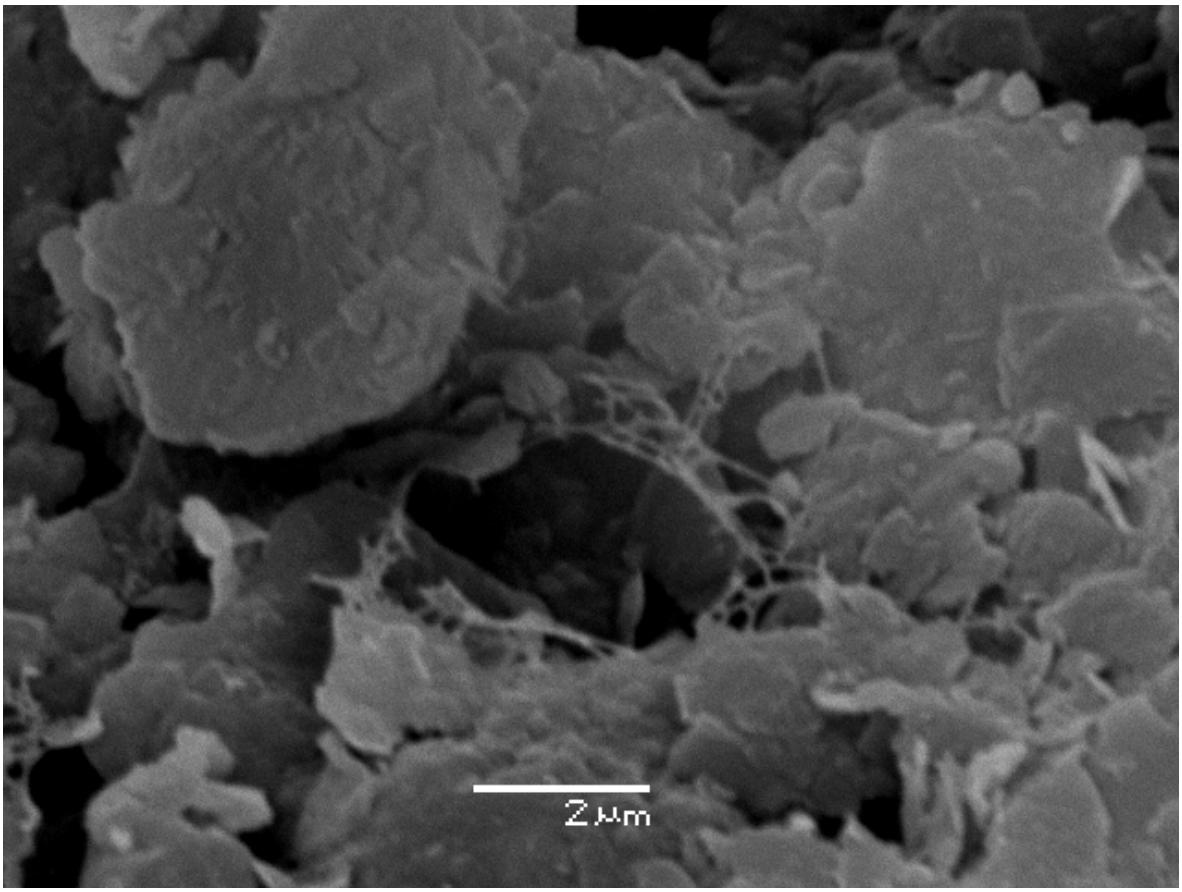

Figure 32: Peculiar fibrous illite appearing between adjacent clay minerals found in sediments expose to pH 10.

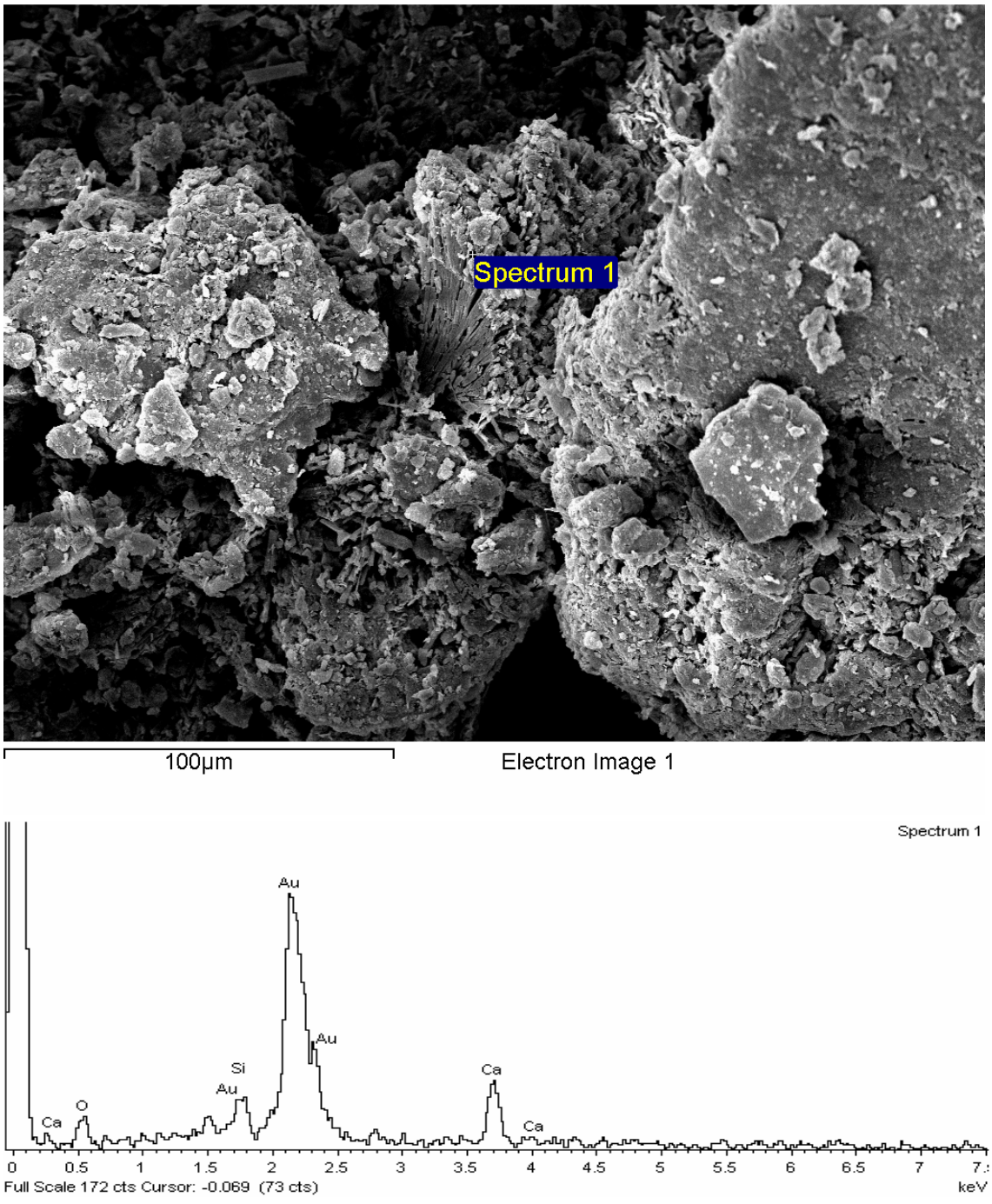

Figure 33: Carbonate mineral (probably calcite) observed in sediments exposed to solution number 8.

9 Discussion

There are numerous aspects related to experimental procedure followed and results obtained in this thesis that deserve discussion. However, as most of the problems encountered have already been discussed in the previous chapters, this section mainly focuses on the results, in addition to a few important aspects of the procedure.

The change from a flow through experiment using brine/CO_2 to a breakthrough pressure test was done without any alterations on the experimental setup. Although there was a possibility that tubes or even pumps were contaminated with the slurry occupying the bottom of the initial mixing chamber, it was decided to proceed without removing the CO_2 from the pumps. The chance of contamination somewhere in the system can therefore not be excluded. However, nothing has so far indicated contamination outside the mixing chamber.

In the beginning of the breakthrough test the cell pressure was 13 MPa. To prevent leakage between the membrane and sample, the differential pressure should be minimum 0.5 MPa. As the theoretically derived maximum breakthrough pressure was 5.4 MPa (*see* chapter 6), it was decided to pressurize the top of the sample to 7.5 MPa. This allowed for a maximum sample pressure gradient of 5.0 MPa. Difficulties related to excessively high compressibility could partly have been avoided by increasing the cell pressure and choosing a pressure in the top farther from the critical point of CO_2. In addition, moving away from the critical point would decrease potential problems related to phase transitions. When operating as close to the critical point as in this study, accurate volume measurements require a temperature stability unfortunately not obtained in the present setup.

Even with an experimental setup not designed for capillary breakthrough experiment, it was possible to identify a sample pressure gradient at which the flow behavior in the pumps connected to the top and bottom of the sample changed from that experienced at lower pressure gradient. At approximately the same time as the onset of these changes, a significant horizontal expansion of the sample began. If CO2 did indeed displace the heavier brine occupying the claystone pores, a radial shortening might intuitively seem more reasonable. A possible explanation of the expansion could be that the boundary between high and low pressure was close to the bottom of the sample, making breakthrough a way of distributing a

generally higher pressure across the sample height. Another explanation could be pore pressure build-up along a relatively thin horizontal section of the sample (maybe along the original horizontal layering), corresponding to the height at which the deformation sensor was located. As only one radial deformation sensor was used, the possibility of instrumental malfunction should not be ruled out. In the axial direction, comparison of the two sensors strongly indicated that they worked properly.

As the radial expansion has now continued for more than a week, the most plausible explanation besides breakthrough is perhaps tensile failure. The shear strength of adjacent material was tested at NGI in 1998, and found to be around 4.0 MPa at similar differential pressures. The tensile strength of the material is usually lower. As these rock strengths are close to the differential pressure applied in the experiment, the possibility of rock failure can not be disregarded. If the claystone did actually fracture, the pressure gradient in the sample should not be mistaken for breakthrough pressure.

To some extent the batch experiments at the University of Oslo demonstrated the pH dependency of dissolution of especially carbonate minerals. As most of the carbonate initially present was in the form of dolomite, the solutions became saturated with calcite at relatively low pHs. Complete dolomite saturation was not reached for the pHs used in this experiment. Considering the low pH of 3 in the CO_2/brine mixture after CO_2 injection from Gaus et al. (2005), significant portions of the Draupne claystone would probably dissolve after CO_2 injection. The high magnesium content in the acidic solutions could perhaps be explained by considering illite and clinochlore (chlorite group) dissolution. Both of these minerals show decreasing dissolution rates with pH over the pH interval utilized in this thesis (Abdulagatov et al., 2007).

Given the time available for the thesis, it was decided to use a broad range of pH solutions rather than to vary the duration or temperature of the different experimental runs. By including different exposure durations, it could have been possible to approach dissolution rates in a more quantitative manner. Also, for organic rich material like the Draupne claystone it would have been interesting to see how much of the organic material that left the samples by total organic carbon analysis.

The flow through experiment at NGI will continue for some time upon the completion of this report. As a large portion of the thesis has been dedicated to experimental work, less time has been available for data processing. Data has been collected at an average logging interval of 10 minutes for 125 days. Together with over 1 500 seismic measurements, the possibilities for further interpretation are numerous.

10 Conclusion

The combination of geochemical and geomechanical experiments on caprock material can be used to gain insight into how the sealing capacity will be affected by CO_2 injection. The chemical experiments performed on the claystone caprock from the Draupne Formation indicate substantial carbonate dissolution at pH levels expected in formation waters after CO_2 injection. Dissolution of even small amounts of material could severely affect the permeability of the caprock.

The geomechanical test on the claystone aimed at identifying the pressure excess needed to displace brine in the sample by CO_2. Even though an apparent flow through the sample was realized at pressure difference of 3.5 – 3.9 MPa between top and bottom, the peculiar strain behavior makes caution necessary in terms of interpreting the results. As the possibility of rock failure can not be excluded, the sample should be taken out of the cell and examined closely before conclusions are drawn. However, if the pressure gradient indeed corresponds to the capillary breakthrough pressure, the theoretical estimation of it correlates very well with the experimentally determined.

In terms of underground geological storage of CO_2 underneath the caprock examined in this report, the injection pressure should not exceed the pore pressure in the caprock by more than ~3.5 MPa. Usual pressure at depths of this claystone is approximately 10 MPa, suggesting a maximum injection pressure of 13.5 MPa. Assuming a density of formation water of 1 000 kg/m^3 and density of injected CO_2 of 600 kg/m^3, equation 3.13 gives a maximum height of CO_2 that can be stored beneath the caprock close to 900 meters.

Considering the thesis objectives, significant improvements on the experimental setup and procedure has been made. The continuing experimental work on caprock integrity at NGI can hopefully benefit from the lessons learned in this report. In addition, as already mentioned, a substantial amount of data exists from the experiment. Even though not enough time was available to fully examine the data in this report, efforts will be made after the submission of this report to fully understand what happened to the caprock after CO_2 injection.

11 References

Aagaard, P. and H. C. Helgeson, Thermodynamic and Kinetic Constraints on Reaction-Rates Among Minerals and Aqueous-Solutions .1. Theoretical Considerations, *Am J Sci, 282*(3), 237-285, 1982.

Abdulagatov, A. I., G. V. Stepanov and I. M. Abdulagatov, The critical properties of binary mixtures containing carbon dioxide: Krichevskii parameter and related thermodynamic properties, *High Temperature, 45*(3), 408-424, 2007.

Adams, J. J. and S. Bachu, Equations of state for basin geofluids: algorithm review and intercomparison for brines (vol 2, pg 257, 2002), *Geofluids, 4*(3), 250, 2004.

Angeli, M., Multiscale study of stone decay by salt crystallization in porous networks, Ph.d. 2007.

Bachu, S., Screening and ranking of sedimentary basins for sequestration of CO_2 in geological media in response to climate change, *Environmental Geology, 44*(3), 277-289, 2003.

Bateman, K., G. Turner, J. M. Pearce, D. J. Noy, D. Birchall and C. A. Rochelle, Large-scale column experiment: Study of CO_2, porewater, rock reactions and model test case, *Oil & Gas Science and Technology-Revue de l Institut Francais du Petrole, 60*(1), 161-175, 2005.

Bentham, M. and G. Kirby, CO2 storage in saline aquifers, *Oil & Gas Science and Technology-Revue de l Institut Francais du Petrole, 60*(3), 559-567, 2005.

Berre, T. Rock Mechanical Testing. Troll East. Well 31/6-A-8. Laboratory Tests on Claystone. NGI. 1998.

Black, R. Humans blamed for climate change. 2007.

Blum, A. and A. Lasaga, Role of Surface Speciation in the Low-Temperature Dissolution of Minerals, *Nature, 331*(6155), 431-433, 1988.

Bøe, R., C. Magnus, P. T. Osmundsen and B. I. Rindstad. CO_2 point sources and subsurface storage capacities for CO_2 in aquifers in Norway. 2002.

Carroll, S. A. and K. G. Knauss, Dependence of labradorite dissolution kinetics on CO_2(aq), Al^{-}(aq), and temperature, *Chemical Geology, 217*(3-4), 213-225, 2005.

Chalbaud, C., M. Robin, S. Bekri and P. Egermann, Wettability impact on CO_2 storage in aquifers: Visualisation and quantification using micromodel tests, pore network model and reservoir simulations., Calgary, 2007.

Chiquet, P., D. Broseta and S. Thibeau, Wettability alteration of caprock minerals by carbon dioxide, *Geofluids, 7*(2), 112-122, 2007a.

Chiquet, P., J. L. Daridon, D. Broseta and S. Thibeau, CO_2/water interfacial tensions under pressure and temperature conditions of CO_2 geological storage, *Energy Conversion and Management, 48*(3), 736-744, 2007b.

Clausen, J. A., R. H. Gabrielsen, P. A. Reksnes and E. Nysaether, Development of intraformational (Oligocene-Miocene) faults in the northern North Sea: influence of remote stresses and doming of Fennoscandia, *Journal of Structural Geology, 21*(10), 1457-1475, 1999.

Czernichowski-Lauriol, I., C. A. Rochelle, I. Gaus, M. Azaroual, J. Pearce and P. Durst, Geochemical Interactions Between CO_2, Pore-Waters and Reservoir Rocks, in Proceedings of the NATO Advanced Research Workshop on Advances in CO_2 Geological Sequestration in Eastern and Western Europe, vol. 65, edited by S. Lombardi, L. K. Altunina and S. E. Beaubien, pp. 157-174, Springer, 2006.

Dahl, B., The use of bisnorhopane as a stratigraphic marker in the Oseberg Back Basin, North Viking Graben, Norwegian North Sea, *Organic Geochemistry, 35*(11-12), 1551-1571, 2004.

Doerr, A. H. and J. F. Coling, Fundamentals of physical geography, Wm. C. Brown Publishers, 1993.

Doughty, C., B. M. Freifeld and R. C. Trautz, Site characterization for CO_2 geologic storage and vice versa: the Frio brine pilot, Texas, USA as a case study., *Environmental Geology,* 2007.

Duan, Z. H. and R. Sun, An improved model calculating CO2 solubility in pure water and aqueous NaCl solutions from 273 to 533 K and from 0 to 2000 bar, *Chemical Geology, 193*(3-4), 257-271, 2003.

Eiken, O., I. Brevik, R. Arts, E. Lindeberg and K. Fagervik, Seismic monitoring of CO_2 injected into a marine aquifer., Calgary, 2000.

Falkowski, P., R. J. Scholes, E. Boyle, J. Canadell, D. Canfield, J. Elser, N. Gruber, K. Hibbard, P. Hogberg, S. Linder, F. T. Mackenzie, B. Moore, T. Pedersen, Y. Rosenthal, S. Seitzinger, V. Smetacek and W. Steffen, The global carbon cycle: A test of our knowledge of earth as a system, *Science, 290*(5490), 291-296, 2000.

Fenghour, A., W. A. Wakeham and V. Vesovic, The viscosity of carbon dioxide, *Journal of Physical and Chemical Reference Data, 27*(1), 31-44, 1998.

Fine, R. A. and F. J. Millero, Compressibility of Water As A Function of Temperature and Pressure, *Journal of Chemical Physics, 59*(10), 5529-5536, 1973.

Gassmann, F., Über die Elastizität poroser Medien, *Vierteljahrsschrift der Naturforschenden Gesellschaft in Zürich, 96*, 1-23, 1951.

Gaus, I., M. Azaroual and I. Czernichowski-Lauriol, Reactive transport modelling of the impact of CO_2 injection on the clayey cap rock at Sleipner (North Sea), *Chemical Geology, 217*(3-4), 319-337, 2005.

Gibbons, K., T. Hellem, A. Kjemerud, S. D. Nio and K. Vebenstad, Sequence architecture, facies development and carbonate-cemented horizons in the Troll Field reservoir,

offshore Norway, in Advances in Reservoir Geology, edited by M. Ashton, pp. 1-31, 1993.

Goodman, R. E., Introduction to Rock Mechanics, John Wiley & Sons, Inc., 1989.

Gundersen, E., F. Renard, D. K. Dysthe, K. Bjorlykke and B. Jamtveit, Coupling between pressure solution creep and diffusive mass transport in porous rocks, *Journal of Geophysical Research-Solid Earth, 107*(B11), 2002.

Gunter, W. D., S. Bachu and S. Benson, The role of hydrogeological and geochemical trapping in sedimentary basins for secure geological storage of carbon dioxide, in Geological Storage of Carbon Dioxide, edited by S. J. Baines and R. H. Worden, pp. 129-145, The Geological Society London, 2004.

Hellevang, H., P. Aagaard, E. H. Oelkers and B. Kvamme, Can dawsonite permanently trap CO_2?, *Environmental Science & Technology, 39*(21), 8281-8287, 2005.

Hellevang, H., S. K. Khattri, G. E. Fladmark and B. Kvamme, Interactions between CO_2, saline water and minerals during geological storage of CO_2 simulations, 2006.

Hildenbrand, A., S. Schlomer, B. M. Krooss and R. Littke, Gas breakthrough experiments on pelitic rocks: comparative study with N^{-2}, CO_2 and CH_4, *Geofluids, 4*(1), 61-80, 2004.

Holloway, S., Storage of fossil fuel-derived carbon dioxide beneath the surface of the earth, *Annual Review of Energy and the Environment, 26*, 145-166, 2001.

IPCC, Underground Geological Storage, in Carbon Dioxide Capure and Storage: Special Report of the Intergovernmental Panel on Climate Change, edited by G. Borm, D. Hawkins and A. Lee, Cambridge University Press, 2005.

Isaksen, G. H. and K. H. I. Ledje, Source rock quality and hydrocarbon migration pathways within the greater Utsira High area, Viking Graben, Norwegian North Sea, *Aapg Bulletin, 85*(5), 861-883, 2001b.

Isaksen, G. H. and K. H. I. Ledje, Source rock quality and hydrocarbon migration pathways within the greater Utsira High area, Viking Graben, Norwegian North Sea, *Aapg Bulletin, 85*(5), 861-883, 2001a.

Isaksen, G. H., R. Patience, G. van Graas and A. I. Jenssen, Hydrocarbon system analysis in a rift basin with mixed marine and nonmarine source rocks: The South Viking Graben, North Sea, *Aapg Bulletin, 86*(4), 557-591, 2002.

Jodecke, M., J. Z. Xia, A. P. S. Kamps and G. Maurer, Solubility of carbon dioxide in aqueous, salt-containing solutions of methanol or acetone, *Chemical Engineering & Technology, 27*(1), 31-+, 2004.

Justwan, H. and B. Dahl. Quantitative hydrocarbon potential mapping and organofacies study in the Greater Balder Area, Norwegain North Sea. 2005.

Justwan, H., B. Dahl, G. H. Isaksen and I. Meisingset, Late to Middle Jurassic source facies and quality variations, South Viking Graben, North Sea, *Journal of Petroleum Geology, 28*(3), 241-268, 2005.

Kaszuba, J. P., D. R. Janecky and M. G. Snow, Carbon dioxide reaction processes in a model brine aquifer at 200 degrees C and 200 bars: implications for geologic sequestration of carbon, *Applied Geochemistry, 18*(7), 1065-1080, 2003.

Kemp, S. J., J. Pearce and E. J. Steadman. Mineralogical, geochemical and petrographical characterisation of Nordland shale cores from well 15/9-A-11, Sleipner field, northern North Sea. British Geological Survey Comissioned Report, CR/02/313. 2002.

Klara, S. M., R. D. Srivastava and H. G. McIlvried, Integrated collaborative technology, development program for CO_2 sequestration in geologic formations - United States Department of Energy R&D, *Energy Conversion and Management, 44*(17), 2699-2712, 2003.

Knudsen, K., D. Leythaeuser, B. Dale, S. R. Larter and B. Dahl, Variation in Organic-Matter Quality and Maturity in Draupne Formation Source Rocks from the Oseberg Field Region, Offshore Norway, *Organic Geochemistry, 13*(4-6), 1051-&, 1988.

Koschel, D., J. Y. Coxam, L. Rodier and V. Majer, Enthalpy and solubility data of CO_2 in water and NaCl(aq) at conditions of interest for geological sequestration, *Fluid Phase Equilibria, 247*(1-2), 107-120, 2006.

Kvamme, B., T. Kuznetsova, A. Hebach, A. Oberhof and E. Lunde, Measurements and modelling of interfacial tension for water plus carbon dioxide systems at elevated pressures, *Computational Materials Science, 38*(3), 506-513, 2007.

Lagneau, V., A. Pipart and H. Catalette, Reactive transport modelling of CO_2 sequestration in deep saline aquifers, *Oil & Gas Science and Technology-Revue de l Institut Francais du Petrole, 60*(2), 231-247, 2005.

Lasaga, A. C., Chemical-Kinetics of Water-Rock Interactions, *Journal of Geophysical Research, 89*(NB6), 4009-4025, 1984.

Le Guen, Y., F. Renard, R. Hellmann, E. Brosse, M. Collombet, D. Tisserand and J. P. Gratier, Enhanced deformation of limestone and sandstone in the presence of high P-CO_2 fluids, *Journal of Geophysical Research-Solid Earth, 112*(B5), 2007.

Li, S., M. Dong, Z. Li, S. Huang, H. Qing and E. Nickel, Gas breakthrough pressure for hydrocarbon reservoir seal rocks: implications for the security of long-term CO_2 storage in the Weyburn field, *Geofluids, 5*(4), 326-334, 2005.

Li, Z. W., M. Z. Dong, S. L. Li and S. Huang, CO_2 sequestration in depleted oil and gas reservoirs - caprock characterization and storage capacity, *Energy Conversion and Management, 47*(11-12), 1372-1382, 2006.

Lindeberg, E., Escape of CO2 from aquifers, *Energy Conversion and Management, 38*, S235-S240, 1997.

MacroSensors, What is an LVDT, and more! Available at *www. macrosensors. com,* Accessed 2008.1.4.

Matter, J. M., T. Takahashi and D. Goldberg, Experimental evaluation of in situ CO_2-water-rock reactions during CO_2 injection in basaltic rocks: Implications for geological CO_2 sequestration, *Geochemistry Geophysics Geosystems, 8*, 2007.

Moore, D. M. and R. C. Reynolds, X-ray Diffraction and the Identification and Analysis of Clay Minerals, OXFORD UNIVERSITY PRESS, 1989.

Nordbotten, J. M., M. A. Celia and S. Bachu, Injection and storage of CO_2 in deep saline aquifers: Analytical solution for CO_2 plume evolution during injection, *Transport in Porous Media, 58*(3), 339-360, 2005.

Okamoto, I., X. C. Li and T. Ohsumi, Effect of supercritical CO_2 as the organic solvent on cap rock sealing performance for underground storage, *Energy, 30*(11-12), 2344-2351, 2005.

Phillips, S. L., R. J. Otto, H. Ozbek and M. Tavana, A Technical Databook for Geothermal-Energy Utilization, *Abstracts of Papers of the American Chemical Society, 181*(MAR), 36-GEOC, 1981.

Portier, S. and C. Rochelle, Modelling CO_2 solubility in pure water and NaCl-type waters from 0 to 300 degrees C and from 1 to 300 bar - Application to the Utsira Formation at Sleipner, *Chemical Geology, 217*(3-4), 187-199, 2005.

Ren, Q. Y., G. J. Chen, W. Yan and T. M. Guo, Interfacial Tension of (CO_2+CH_4) plus water from 298 K to 373 K and pressures up to 30 MPa, *Journal of Chemical and Engineering Data, 45*(4), 610-612, 2000.

Renard, F., E. Gundersen, R. Hellmann, M. Collombet and Y. Le Guen, Numerical modeling of the effect of carbon dioxide sequestration on the rate of pressure solution creep in limestone: Preliminary results, *Oil & Gas Science and Technology-Revue de l Institut Francais du Petrole, 60*(2), 381-399, 2005.

Rochelle, C. A., I. Czernichowski-Lauriol and A. E. Milodowski, The impact of chemical reactions on CO_2 storage in geological formations: a brief review, in Geological

Storage of Carbon Dioxide, vol. 223, edited by S. J. Baines and R. H. Worden, pp. 87-106, The Geological Society London, 2008.

Rosenbauer, R. J., T. Koksalan and J. L. Palandri, Experimental investigation of CO_2-brine-rock interactions at elevated temperature and pressure: Implications for CO_2 sequestration in deep-saline aquifers, *Fuel Processing Technology, 86*(14-15), 1581-1597, 2005.

Sirard, S. M., K. J. Ziegler, I. C. Sanchez, P. F. Green and K. P. Johnston, Anomalous properties of poly(methyl methaerylate) thin films in supercritical carbon dioxide, *Macromolecules, 35*(5), 1928-1935, 2002.

Spiteller, M., Extraction of Soil Organic-Matter by Supercritical Fluids, *Organic Geochemistry, 8*(1), 111-113, 1985.

Springer, N. and H. Lindgren, Caprock properties of the Nordland shale recovered from the 15/9-A-11 well, the Sleipner Area, 2006.

Suekane, T., S. Soukawa, S. Iwatani, S. Tsushima and S. Hirai, Behavior of supercritical CO_2 injected into porous media containing water, *Energy, 30*(11-12), 2370-2382, 2005.

Torp, T. A. and J. Gale, Demonstrating storage of CO_2 in geological reservoirs: The sleipner and SACS projects, *Energy, 29*(9-10), 1361-1369, 2004.

Trietley, H. L., Magnetic Transducers, in Transducers in Mechanical and Electronic Design, pp. 68-96, CRC Press, 1986.

UiO, UiB, NGI and IFE. Subsurface Storage of CO_2 - Risk Assessment, MOnitoring and REmediation. 2008.

Walther, J. V., Relation between rates of aluminosilicate mineral dissolution, pH, temperature, and surface charge, *Am J Sci, 296*(7), 693-728, 1996.

Wang, Z., M. E. Cates and R. T. Langan, Seismic monitoring of a CO_2 flood in a carbonate reservoir: A rock physics study, *Geophysics, 63*(5), 1604-1617, 1998.

Wang, Z. and A. Nur, Effects of CO_2 Flooding on Wave Velocities in Rocks with Hydrocarbons., *SPE Reservoir Engineering, 4*, 429, 1989.

www.chemicalogic.com, Mollier Chart in Metric Units , Available at *www. chemicalogic. com/download/mollier. html,* Accessed 2008.1.2.

www.eia.doe.gov, Greenhouse Gases, Climate Change, and Energy , Available at *http://www. eia. doe. gov/oiaf/1605/ggccebro/chapter1. html,* Accessed 2007.11.11.

Xie, Z. X. and J. V. Walther, Incongruent Dissolution and Surface-Area of Kaolinite, *Geochimica et Cosmochimica Acta, 56*(9), 3357-3363, 1992.

Yuh, S. H., Time-lapse Seismic Monitoring of Subsurface Fluid Flow, 2003.

List of Appendices

Appendix A: Index Testing	***2-3***
Appendix B: False Deformation of Membrane	***4***
Appendix C: Permeability Test	***5***
Appendix D: XRD Results	***6-12***
Appendix E: Scanning Electron Microscope	***13-16***
Appendix F: Results from Solution Analysis	***17***
Appendix G: P-wave Velocity Measurements	***18-19***

APPENDIX A: Index testing

Water content and saturation degree of rest material:

Mass of wet sample m_{ws} (g)	60.19
Mass of dry sample m_{ds} (g)	50.81
Mass of water displaced by sample m_{dw} (g)	29.20
Density of saline water ρ_{diw} (g/cm^3)	1.0269
Density of solid particles (from -98) ρ_{sp} (g/cm^3)	2.75

$$Water\ content = \frac{m_{ws} - m_{ds}}{m_{ds}} = \frac{60.19 - 50.81}{50.81} \times 100\% = \underline{18.46\ \%}$$

$$Volume\ of\ wet\ sample\ V_{ws} = \frac{m_{dw}}{\rho_{diw}} = \left(\frac{29.20}{1.0269}\right) cm^3 = \underline{28.44\ cm^3}$$

$$Volume\ of\ dry\ sample\ V_{ds} = \frac{m_{ds}}{\rho_{sp}} = \left(\frac{50.81}{2.75}\right) cm^3 = \underline{18.48\ cm^3}$$

$$Pore\ volume\ V_p = V_{ws} - V_{ds} = (28.44\text{-}18.48)\ cm^3 = \underline{9.96\ cm^3}$$

$$Volume\ of\ water\ in\ sample\ V_{w,ws} = \frac{m_{ws} - m_{ds}}{\rho_{diw}} = \left(\frac{60.19 - 50.81}{1.0269}\right) cm^3 = \underline{9.13\ cm^3}$$

$$Degree\ of\ saturation = \frac{V_{w,ws}}{V_p} = \left(\frac{9.13}{9.96}\right) \times 100\% = \underline{91.7\ \%}$$

Sample density and porosity

$$Sample\ density\ \rho_s = \frac{m_{ds}}{V_{ws}} = \left(\frac{50.81}{28.44}\right) g/cm^3 = \underline{1.79\ g/cm^3}$$

$$Porosity = \frac{V_p}{V_{ws}} \times 100\% = \frac{9.13}{28.44} \times 100\% \ = \underline{35.0\ \%}$$

$$Porosity = \left(1 - \frac{\rho s}{\rho b}\right) \times 100\% = \left(1 - \frac{1.79}{2.75}\right) \times 100\% = \underline{34.9\ \%}$$

Appendix B: False deformation of membrane

Determination of false deformation:

Cell pressure	Mean axial deformation	Radial deformation	$\varepsilon = (\sigma_{cp} / E) \times (1 - 2\mu)$	False axial deformation	False radial deformation
MPa	*mm*	*mm*		*mm*	*mm*
9,600E-02	0,000E+00	0,000E+00	1,875E-07	-7,501E-06	-7,126E-06
1,910E-01	9,200E-04	9,000E-05	3,731E-07	9,051E-04	7,582E-05
5,120E-01	3,200E-03	2,700E-04	1,000E-06	3,160E-03	2,320E-04
1,008E+00	6,220E-03	4,600E-04	1,969E-06	6,141E-03	3,852E-04
2,000E+00	1,047E-02	9,900E-04	3,907E-06	1,031E-02	8,415E-04
2,989E+00	1,362E-02	1,400E-03	5,839E-06	1,339E-02	1,178E-03
3,990E+00	1,632E-02	1,580E-03	7,794E-06	1,601E-02	1,284E-03
4,990E+00	1,865E-02	1,790E-03	9,748E-06	1,826E-02	1,420E-03
5,989E+00	2,094E-02	1,860E-03	1,170E-05	2,047E-02	1,415E-03
6,991E+00	2,331E-02	2,120E-03	1,366E-05	2,276E-02	1,601E-03
7,992E+00	2,546E-02	2,550E-03	1,561E-05	2,484E-02	1,957E-03
8,992E+00	2,760E-02	2,700E-03	1,757E-05	2,690E-02	2,033E-03
9,992E+00	2,957E-02	2,890E-03	1,952E-05	2,879E-02	2,148E-03
1,099E+01	3,185E-02	3,280E-03	2,148E-05	3,099E-02	2,464E-03
1,199E+01	3,386E-02	3,880E-03	2,343E-05	3,292E-02	2,990E-03
1,299E+01	3,596E-02	4,770E-03	2,538E-05	3,494E-02	3,805E-03
1,399E+01	3,796E-02	5,690E-03	2,733E-05	3,687E-02	4,651E-03
1,499E+01	3,984E-02	6,670E-03	2,928E-05	3,867E-02	5,557E-03
1,599E+01	4,180E-02	7,400E-03	3,124E-05	4,055E-02	6,213E-03

From linear regression:

False radial deformation = 0.00032 x Cell Pressure - 0.00019

False axial deformation = 0.00243 x Cell Pressure + 0.00395

Appendix C: Permeability test

Calculated permeability coefficients:

Date	**Time**	**Δt (min)**	**Cell Pressure (MPa)**	**Δu (kPa)**	**k (10^{-11} cm s^{-1})**
28.12.2007	*12.47*	160	13.03	1400	**7.56**
28.12.2007	*15.27*				
29.12.2007	*20.07*	220	13.03	1400	**8.15**
29.12.2007	*23.47*				
30.12.2007	*13.47*	500	13.02	1400	**7.25**
30.12.2007	*22.07*				
31.12.2007	*18.27*	320	13.03	1400	**6.64**
31.12.2007	*23.47*				
01.01.2008	*10.27*	240	13.03	1400	**6.30**
01.01.2008	*14.27*				
02.01.2008	*04.07*	220	13.04	1400	**6.46**
02.01.2008	*07.47*				
03.01.2008	*11.27*	220	13.05	1400	**6.33**
03.01.2008	*15.07*				
04.01.2008	*00.01*	760	13.05	1400	**6.28**
04.01.2008	*12.41*				
05.01.2008	*09.18*	280	13.04	1400	**6.10**
05.01.2008	*13.58*				
06.01.2008	*00.18*	1420	13.04	1400	**5.93**
06.01.2008	*23.58*				
07.01.2008	*00.18*	480	13.03	1400	**5.78**
07.01.2008	*08.18*				
08.01.2008	*02.48*	380	13.04	1400	**6.22**
08.01.2008	*09.08*				

Appendix D: XRD results

Bulk sample

Bulk XRD:

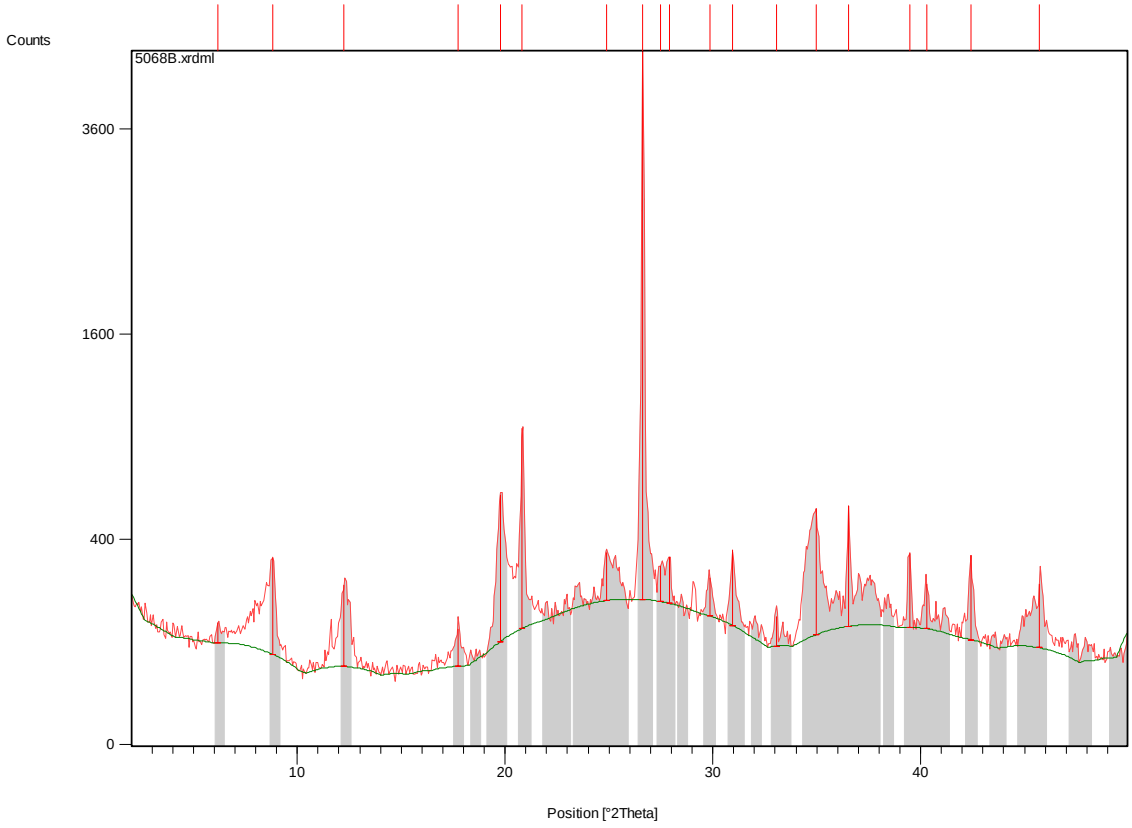

Compound Name	Ref. Code	Empirical Formula	Score
Quartz	46-1045	Si O2	76
Muscovite	01-1098	H2 K Al3 (Si O4)3	54
Kaolinite	06-0221	Al2 Si2 O5 (O H)4	47
Dolomite	36-0426	Ca Mg (C O3)2	37
Chlorite	07-0160	(Mg , Cr)6 (Si , Al)4 O10 (O H)8	37
Potassium feldspar	08-0048	K (Al , Fe) Si2 O8	33
Pyrite	06-0710	Fe S2	25

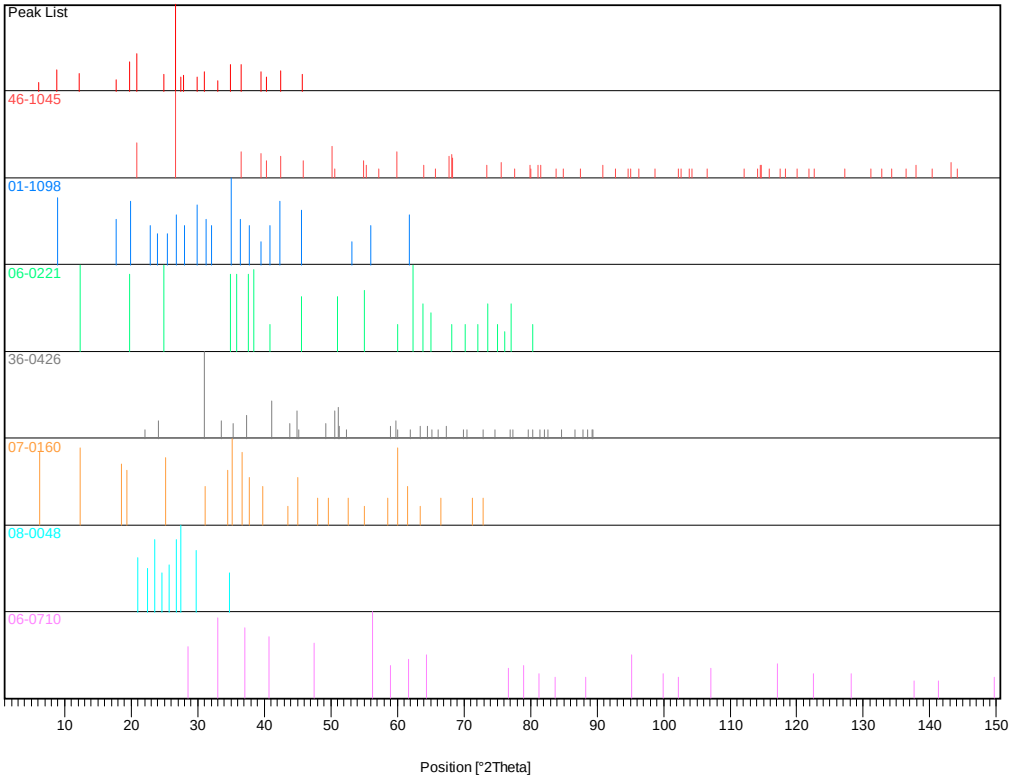

Pos. [°2Th.]	d-spacing [Å]	Matched by	Height [cts]	FWHM [°2Th.]
6.1800	14.30190	07-0160	42.00	0.1500
8.8195	10.02663	01-1098	255.74	0.1771
12.2545	7.22277	06-0221; 07-0160	181.78	0.2362
17.7500	4.99702	01-1098	68.66	0.3542
19.7730	4.49010	01-1098; 06-0221	487.72	0.2952
20.8322	4.26414	46-1045; 08-0048	817.92	0.1771
24.9029	3.57558	06-0221	152.24	0.5904
26.6252	3.34806	46-1045; 01-1098; 08-0048	4375.90	0.2362
27.4800	3.24583	08-0048	106.17	0.1500
27.9000	3.19791	01-1098	143.17	0.1500
29.8459	2.99370	01-1098; 08-0048	106.95	0.3542
30.9583	2.88862	36-0426; 07-0160	225.02	0.2362
33.0661	2.70914	06-0710	63.04	0.3542

34.9604	2.56658	01-1098; 06-0221; 07-0160; 08-0048	414.95	0.2952
36.5374	2.45933	46-1045; 01-1098; 07-0160	408.21	0.1771
39.4625	2.28352	46-1045; 01-1098	219.07	0.1771
40.2977	2.23810	46-1045	115.46	0.2362
42.4203	2.13090	46-1045; 01-1098	234.49	0.1771
45.7299	1.98244	46-1045; 01-1098; 06-0221	154.49	0.4320

Slow scan (26 – 28.5 °2θ):

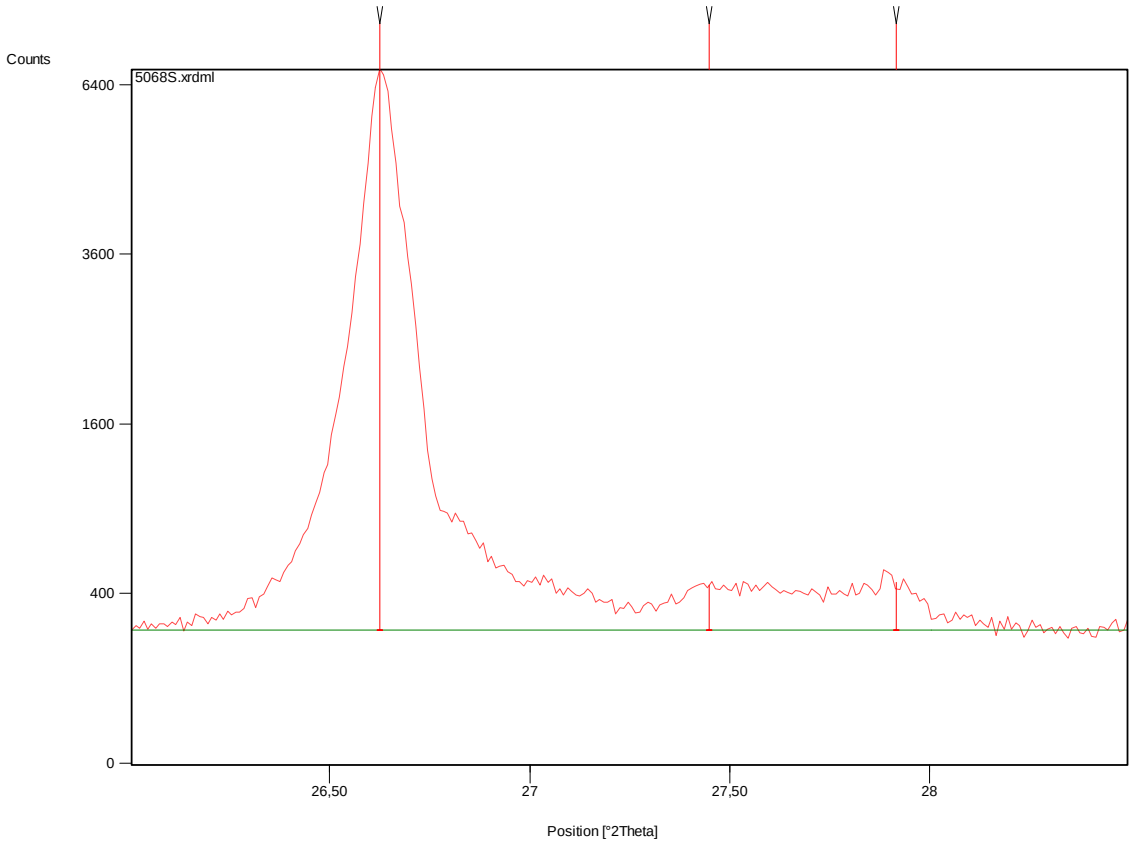

Pos. [°2Th.]	Height [cts]	FWHM [°2Th.]	d-spacing [Å]	Rel. Int. [%]
26,6262	6477,28	0,0689	3,34794	100,00
27,4479	197,16	0,1574	3,24955	3,04
27,9161	207,83	0,0984	3,19611	3,21

Clay fraction XRD:

Treated with ethylene glycol:

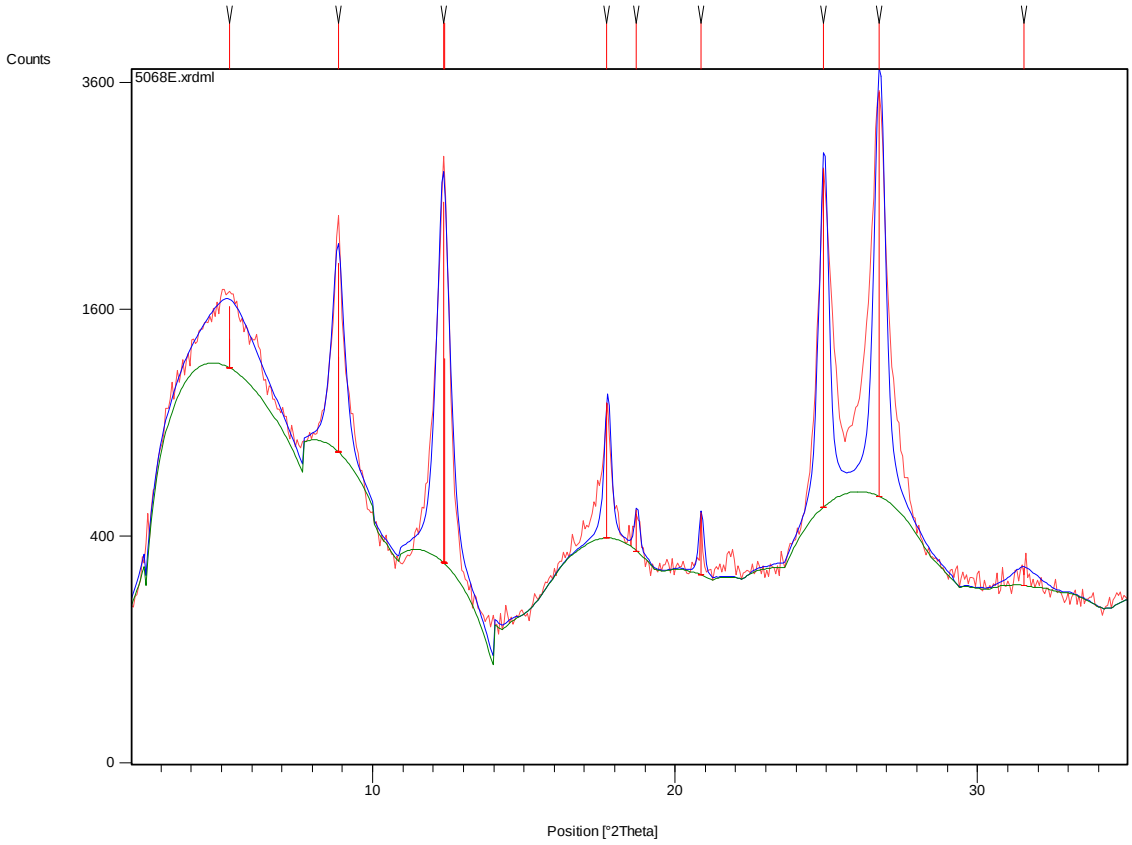

Pos. [°2Th.]	Height [cts]	FWHM [°2Th.]	d-spacing [Å]	Rel. Int. [%]
5,2645	405,25	2,0300	16,77297	13,68
5,2776	182,36	2,0300	16,77297	6,16
8,8600	1182,35	0,4391	9,97262	39,92
8,8821	532,06	0,4391	9,97262	17,96
12,3355	2128,87	0,4147	7,16962	71,88
12,3662	957,99	0,4147	7,16962	32,35
17,7483	617,46	0,2362	4,99749	20,85
18,7255	150,08	0,1771	4,73885	5,07
20,8671	211,37	0,1771	4,25709	7,14
24,8955	2238,92	0,2952	3,57662	75,59
26,7492	2961,79	0,3542	3,33283	100,00
31,5406	48,33	0,9446	2,83661	1,63

Slow scan (24 – 26 °2θ):

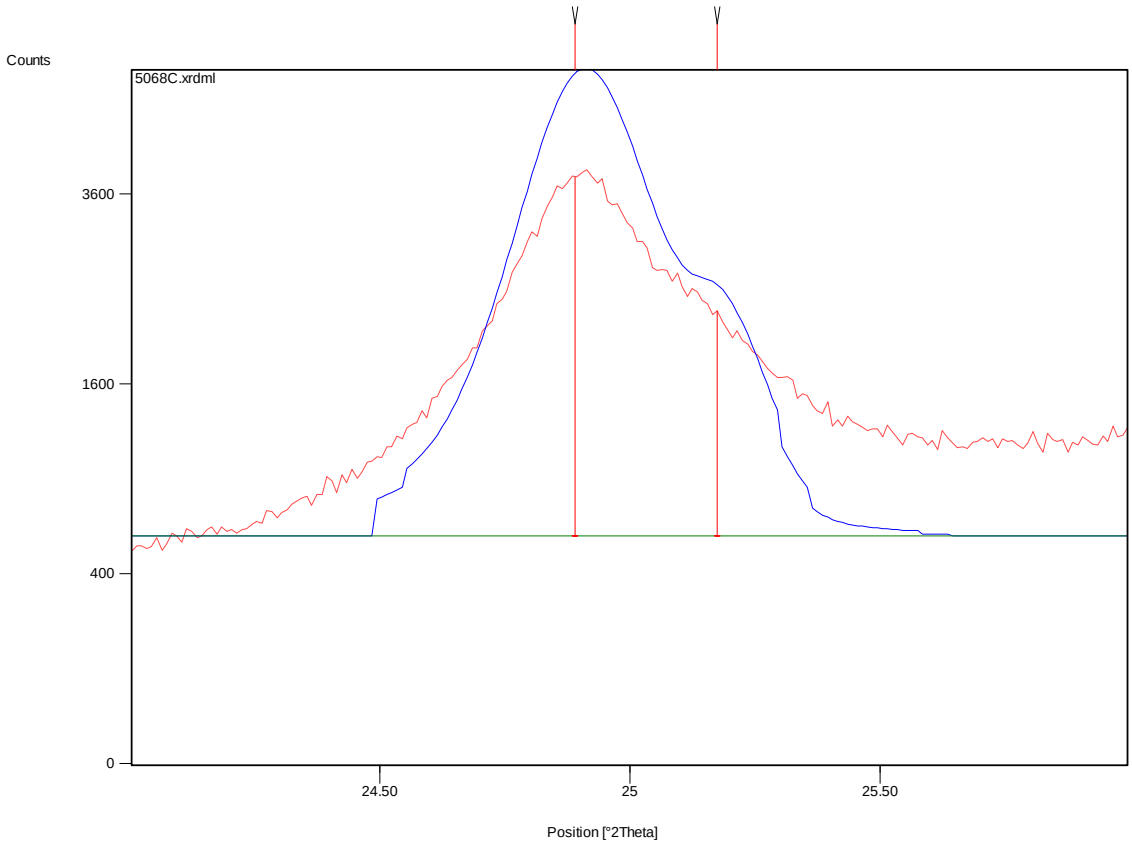

Pos. [°2Th.]	Height [cts]	FWHM [°2Th.]	d-spacing [Å]	Rel. Int. [%]
24.8915	3237.74	0.2880	3.57423	100.00
25.1750	1695.00	0.1500	3.53754	52.35

Weight percents:

Calculations without using weight factors:

XRD

From bulk

	d-spacing [Å]	*Heigth [cts]*	*FWHM [°2Th.]*	*Height x FWHM*	*Relative wt %*	*Absolutt weight percent*
"Quartz"	4.26	817.92	0.1771	144.854	39.76	
"Total Clay"	4.5	487.72	0.2952	143.975	39.52	
Dolomite/Ankerite	2.89	225.02	0.2362	53.150	14.59	14.6
Pyrite	2.71	63.04	0.3542	22.329	6.13	6.1
Total				364.307		

From slow scan

	d-spacing [Å]	*Heigth [cts]*	*FWHM [°2Th.]*	*Height x FWHM*	*Relative wt %*	*Absolutt weight percent*
Quartz	3.33	6477.28	0.0689	446.285	89.66	35.7
K-feldpar	3.24	197.16	0.1574	31.033	6.23	2.5
Plagioclase	3.18	207.83	0.0984	20.450	4.11	1.6
Total				497.768		

From clay minerals

	d-spacing [Å]	*Heigth [cts]*	*FWHM [°2Th.]*	*Height x FWHM*	*Relative wt %*	*Absolutt weight percent*
Smectite	17	405.25	2.0300	822.658	36.98	14.6
Iliite/Muscovite	10	1182.35	0.4391	519.170	23.34	9.2
Kaolinite/Chlorite	7	2128.87	0.4147	882.842	39.68	
Total				2224.670		

Kaolinite/Chlorite

	d-spacing [Å]	*Heigth [cts]*	*FWHM [°2Th.]*	*Height x FWHM*	*Relative wt %*	*Absolutt weight percent*
Kaolinite	3.57	3237.74	0.2880	932.469	78.58	12.3
Chlorite	3.53	1695.00	0.1500	254.250	21.42	3.4
Total				1186.719		

Composition

Mineral	***Weight percent***
Quartz	35.7
K-feldspar	2.5
Plagioclase	1.6
Dolomite/Ankerite	14.6
Pyrite	6.1
Smectite	14.6
Illite/Muscovite	9.2
Kaolinte	12.3
Chlorite	3.4
Total	**100**

Calculations using weight factors:

From bulk

	d-spacing [Å]	*Heigth [cts]*	*FWHM [°2Th.]*	*Weight factor*	*Height x FWHM x weight factor*	*Relative wt %*	*Absolutt weight percent*
"Quartz"	4.26	817.92	0.1771	7.5	1086.402	26.56	
"Total Clay"	4.5	487.72	0.2952	20	2879.499	70.40	
Dolomite/Ankerite	2.89	225.02	0.2362	1.5	79.725	1.95	2.0
Pyrite	2.71	63.04	0.3542	2	44.658	1.09	1.1
Total					4090.283		

From slow scan

	d-spacing [Å]	*Heigth [cts]*	*FWHM [°2Th.]*	*Weight factor*	*Height x FWHM x weight factor*	*Relative wt %*	*Absolutt weight percent*
Quartz	3.33	6477.28	0.0689	1	446.285	68.98	18.3
K-feldpar	3.24	197.16	0.1574	3.7	114.822	17.75	4.8
Plagioclase	3.18	207.83	0.0984	4.2	85.892	13.28	3.5
Total					646.999		

From clay minerals

	d-spacing [Å]	*Heigth [cts]*	*FWHM [°2Th.]*	*Weight factor*	*Height x FWHM x weight factor*	*Relative wt %*	*Absolutt weight percent*
Smectite	17	405.25	2.0300	20	16453.150	36.98	26.0
Illiite/Muscovite	10	1182.35	0.4391	20	10383.398	23.34	16.4
Kaolinite/Chlorite	7	2128.87	0.4147	20	17656.848	39.68	27.9
Total					44493.395		

Kaolinite/Chlorite

	d-spacing [Å]	*Heigth [cts]*	*FWHM [°2Th.]*	*Weight factor*	*Height x FWHM x weight factor*	*Relative wt %*	*Absolutt weight percent*
Kaolinite	3.57	3237.74	0.2880	20	18649.382	0.79	22.0
Chlorite	3.53	1695.00	0.1500	20	5085.000	0.21	5.9
Total					23734.382		

Composition

Mineral	***Weight percent***
Quartz	18.3
K-feldspar	4.8
Plagioclase	3.5
Dolomite/Ankerite	2
Pyrite	1.1
Smectite	26
Illite/Muscovite	16.4
Kaolinte	22
Chlorite	5.9
Total	**100**

Appendix E: Scanning Electron Microscope

Salt crystals:

Numerous salt crystals were seen on horizontal surfaces. Element spectrums indicate dominance of clay minerals.

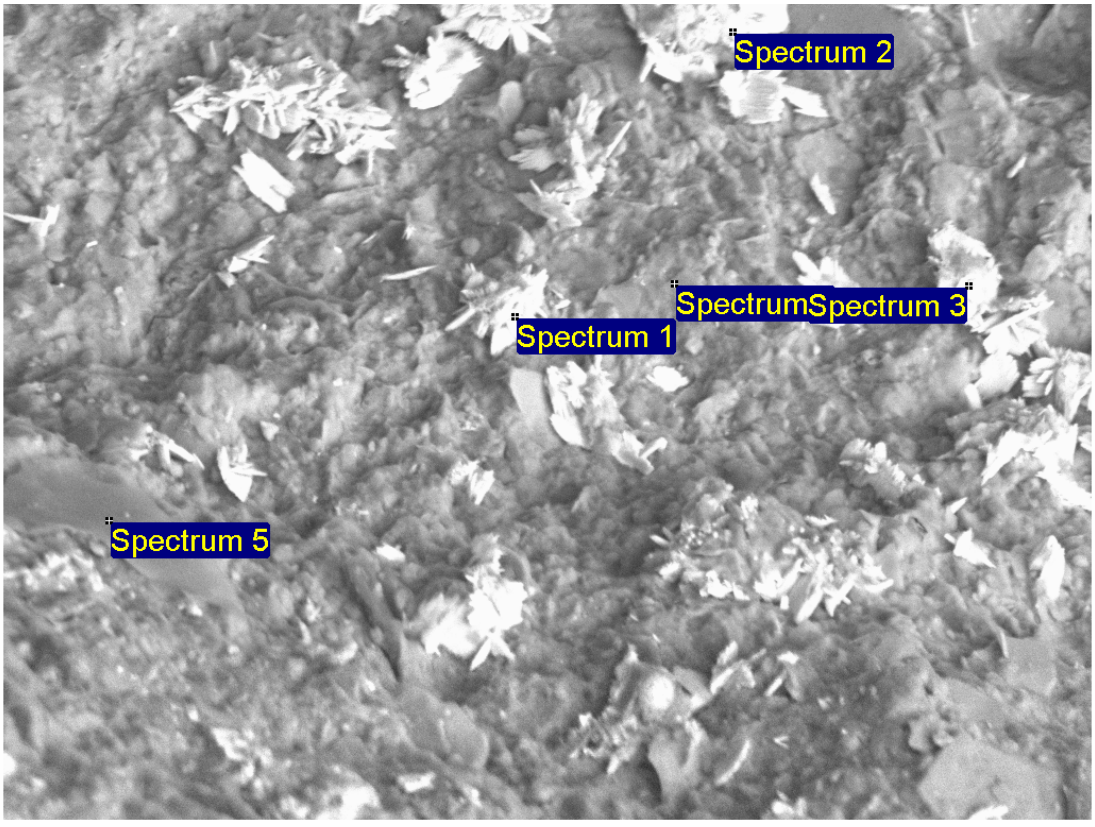

90µm Electron Image 1

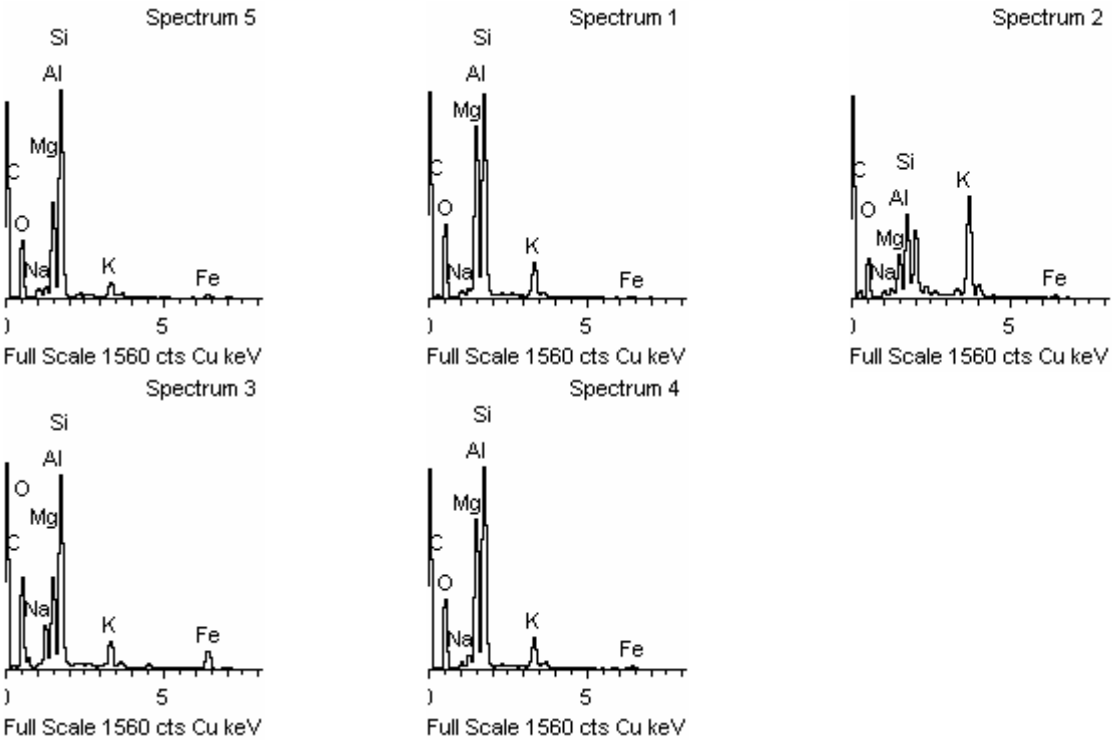

Planar clay minerals:

Planar clay minerals were clearly seen on the horizontal surfaces.

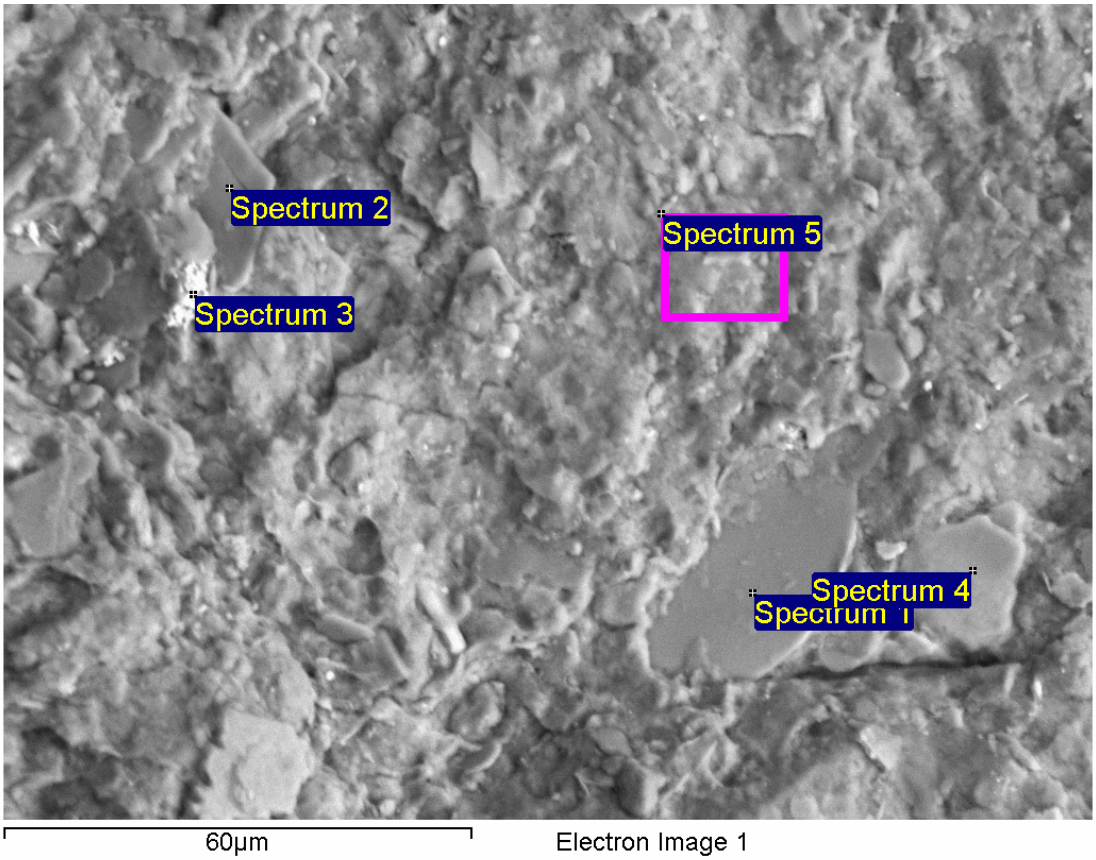

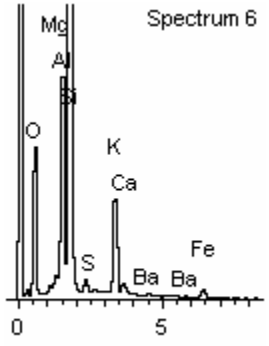

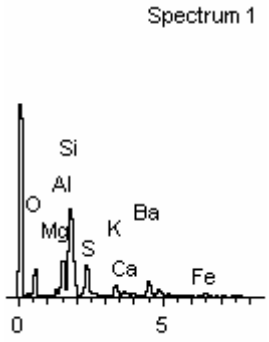

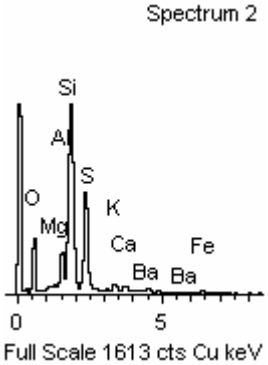

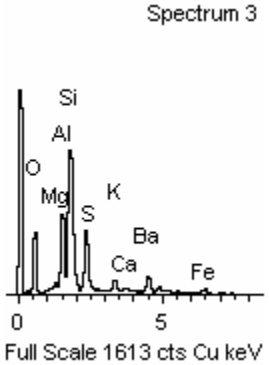

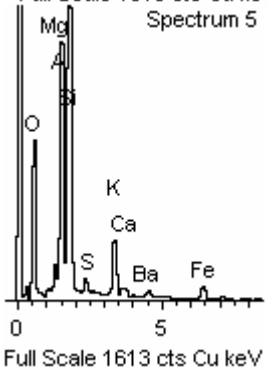

Vertical fracture:

Vertical fractures were seen on the horizontal surfaces. These fractures are perpendicular to the main fracture direction.

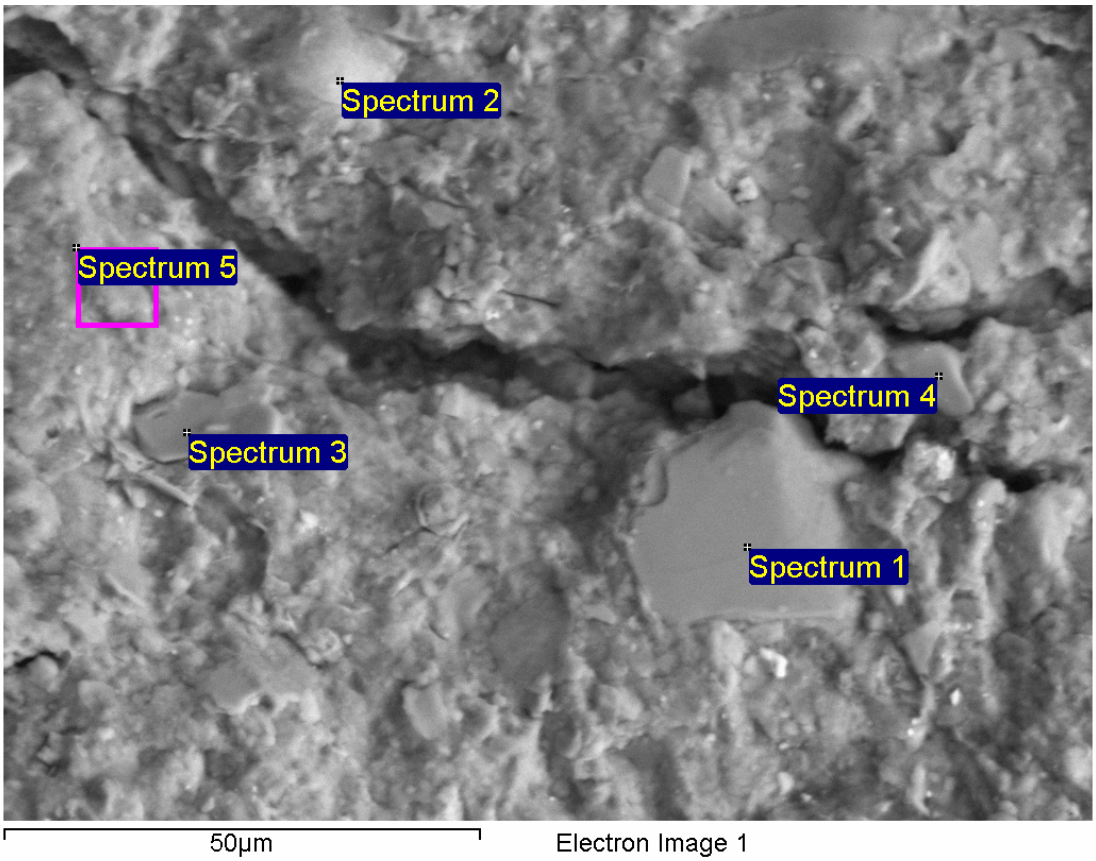

Calcium- and sulphur layer:

A peculiar transition between calcium- and sulphur rich layer (spectrum 1) and clay minerals was seen on the vertical cross-section.

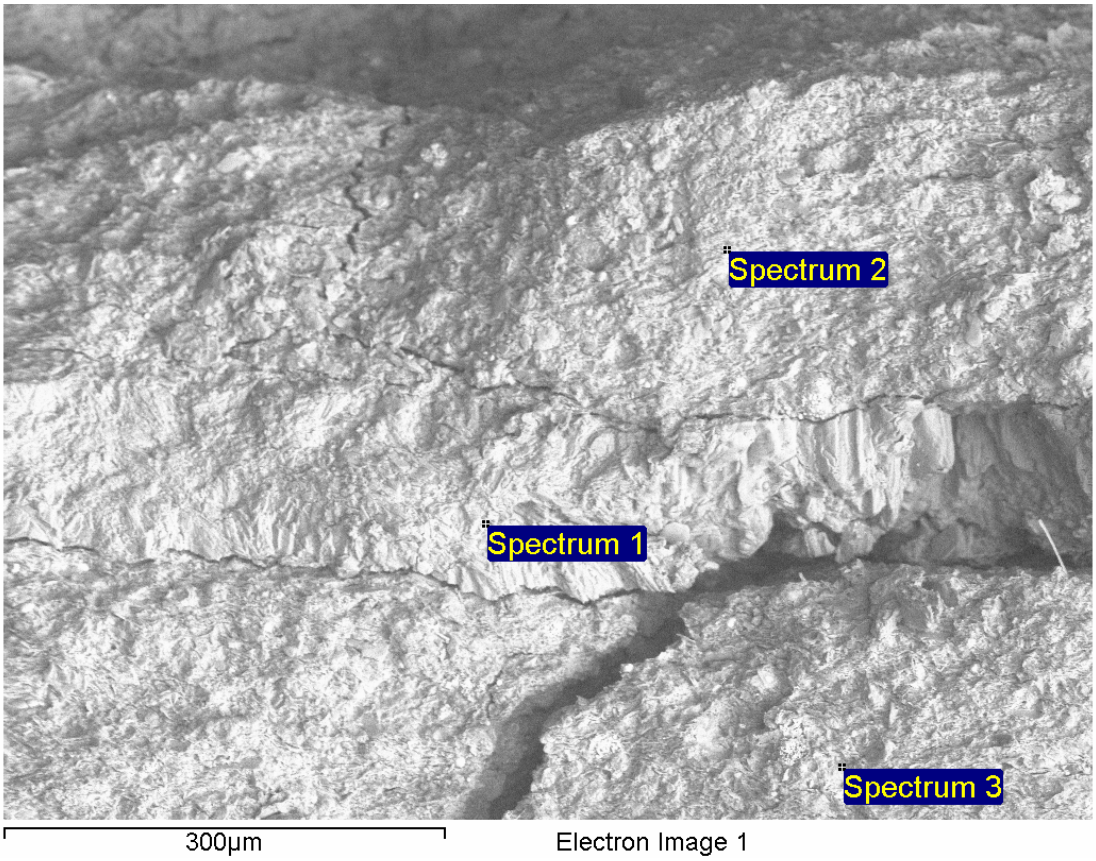

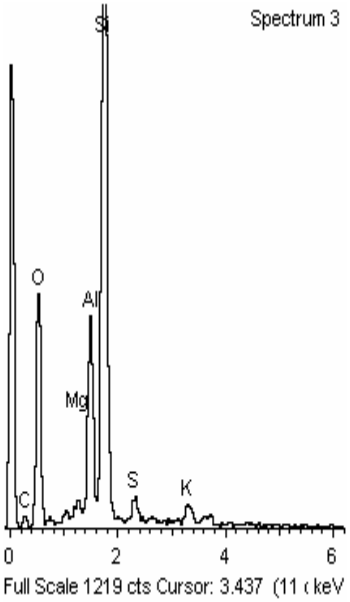

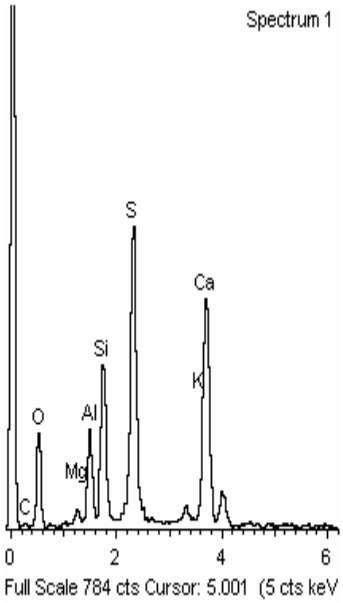

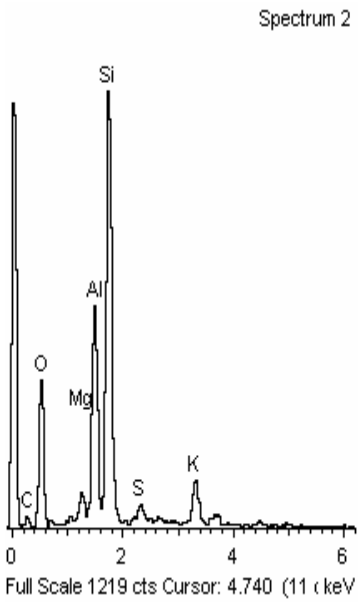

Appendix F: Results from solution analysis

Start pH	Final pH	Alk (meq/l)	Ca (ppm)	Mg (ppm)	Na (ppm)	K (ppm)	Si (ppm)	Al (ppm)	Cl (ppm)	SO_4 (ppm)
2	4.43	0.0333	74	65.6	123	90	44.9	0.08	649	117
3	4.82	0.08	77	66.7	70	51	59.3	0.07	4087	135
4.05	6.69	0.98	78	39.1	87	58	37.1	0.07	484	171
5.14	7.84	1.77	49	43.7	93	66	44.6	0.12	624	120
5.17	7.41	1.62	58	41.0	91	55	43.3	0.08	865	112
6.53	7.61	0.85	49	30.5	76	40	33.2	0.06	973	93
6.63	7.58	0.78	28	10.5	68	35	39.3	0.12	314	90
8.29	6.53	0.26	27	4.0	72	33	40.8	0.25	157	110
8.5	7.63	0.67	33	11.1	77	37	34.2	0.14	274	98
9.75	7.99	1.63	20	2.9	69	34	34.1	0.27	178	169

Appendix G: P-wave velocity measurements

Date	Time	Height (mm)	$t_p - t_{op}$ (s)	V_p (m/s)
13.12.2007	16.21	39.74	17.34	2291.81084
14.12.2007	01.13	39.73	17.35	2289.91354
15.12.2007	21.13	39.67	17.12	2317.1729
16.12.2007	22.13	39.65	17.16	2310.60606
18.12.2007	13.27	39.63	17.16	2309.44056
18.12.2007	15.27	39.61	17.13	2312.31757
18.12.2007	16.27	39.61	17.25	2296.23188
18.12.2007	17.27	39.17	16.17	2422.38714
18.12.2007	18.27	39.61	16.19	2446.57196
18.12.2007	20.27	39.13	16.1	2430.43478
18.12.2007	23.27	39.1	15.98	2446.80851
19.12.2007	11.27	39.07	15.98	2444.93116
19.12.2007	21.27	39.06	16	2441.25
20.12.2007	17.27	39.04	16	2440
21.12.2007	16.07	39.02	15.78	2472.75032
23.12.2007	07.07	39	15.94	2446.67503
23.12.2007	13.27	38.99	15.98	2439.92491
26.12.2007	00.07	38.96	15.89	2451.85651
28.12.2007	05.07	38.95	15.8	2465.18987
30.12.2007	12.47	38.93	15.87	2453.05608
03.01.2008	07.47	38.91	15.92	2444.09548
05.01.2008	05.07	38.9	15.95	2438.87147
07.01.2008	17.07	38.9	15.9	2446.54088
11.01.2008	05.07	38.9	15.92	2443.46734
14.01.2008	09.07	38.89	15.87	2450.5356
15.01.2008	16.24	38.88	15.9	2445.28302
18.01.2008	15.24	38.86	15.8	2459.49367

20.01.2008	17.24	38.85	15.74	2468.2338
22.01.2008	19.24	38.84	15.86	2448.92812
13.02.2008	16.03	38.76	15.69	2470.36329
06.03.2008	18.46	38.73	15.69	2468.45124
12.03.2008	16.44	38.73	15.73	2462.17419
15.03.2008	17.23	38.71	15.77	2454.66075
18.03.2008	16.04	38.71	15.72	2462.46819
21.03.2008	10.13	38.71	15.73	2460.90273
21.03.2008	19.21	38.71	15.83	2445.35692
22.03.2008	09.39	38.71	15.83	2445.35692
22.03.2008	15.36	38.71	15.78	2453.1052
23.03.2008	11.53	38.72	15.89	2436.75267
25.03.2008	08.29	38.73	15.87	2440.45369
27.03.2008	07.55	38.73	15.84	2445.07576
28.03.2008	13.32	38.73	15.76	2457.48731
28.03.2008	16.48	38.73	15.9	2435.84906
29.03.2008	19.17	38.72	15.79	2452.18493